Advanced Fluorescence based Methods for Protein Interaction Studies applied to the RNA binding Protein *At*GRP7

Dissertation

Fabian Humpert

Gedruckt auf alterungsbeständigem Papier nach DIN EN ISO 9706

Inauguraldissertation
zur Erlangung der Doktorwürde
der Fakultät für Physik
der Universität Bielefeld

Advanced Fluorescence based Methods for Protein Interaction Studies applied to the RNA binding Protein *At*GRP7

vorgelegt von
Fabian Humpert
geboren in Wickede

31. Januar 2013

Advanced Fluorescence based Methods for Protein Interaction Studies applied to the RNA binding Protein *At*GRP7 — Fabian Humpert

Gutachter:
Prof. Dr. Markus Sauer
Prof. Dr. Thomas Huser

Zusammenfassung

Im Rahmen dieser Arbeit werden neue Methoden zur Untersuchung verschiedener Interaktionen zwischen Biomolekülen eingeführt und am Beispiel des Glyzin-reichen, RNA-bindenden Proteins *At*GRP7, aus der Pflanze *Arabidopsis thaliana*, angewendet. Dieses Protein ist ein Forschungsschwerpunkt der Arbeitsgruppe *Molekulare Zellphysiologie*, mit der eine Kooperation im Rahmen des Sonderforschungsbereichs SFB 613 besteht. In transgenen *Arabidopsis* Pflanzen wird eine optimierte Variante des reversibel-schaltbaren, fluoreszierenden Proteins Dronpa (genannt Dronpa-s) mit *At*GRP7 fusioniert. So können die intra-zelluläre Verteilung und die Bewegung von *At*GRP7 zwischen Zellkern und Zytoplasma, über Fluoreszenzsignale nachvollzogen werden. Unter anderem wird gezeigt, dass die Fluoreszenz gezielt im Zellkern aus und wieder an geschaltet werden kann, wodurch schließlich ein bidirektionaler Transport von *At*GRP7 nachgewiesen und quantitativ charakterisiert wird.

In einem weiteren Teil der Arbeit, wird *in vitro* die Bindung von *At*GRP7 an kurze RNA Sequenzen untersucht. Diese Eigenschaft ermöglicht es dem Protein, im Zellkern an sein Transkript zu binden, sodass die eigene Proteinbiosynthese, durch selbstregulatorische Mechanismen, unterdrückt wird. Hierzu werden Bindungsstudien mit Hilfe der Fluoreszenz Korrelations Spektroskopie durchgeführt. Es zeigt sich, dass *At*GRP7 eine schwache aber spezifische Bindung mit einer kurzen DNA-Sequenz eingeht, welche eine Bindestelle des Transkriptes repräsentiert.

Die RNA-bindenden Eigenschaften von *At*GRP7 führen auch dazu, dass das Protein in kleinen intra-zellulären Aggregaten zu finden ist, die nur unter Stessbedingungen auftreten. Diese Proteininteraktion

kann durch Kolokalisationsstudien gezeigt werden. Herkömmliche Methoden zur Kolokalisationsanalyse führen hier jedoch zu nicht eindeutig interpretierbaren Ergebnissen. Als Folge daraus wird ein vollkommen neuer Ansatz zur Kolokalisationsanalyse ausgearbeitet. Dieser basiert auf der Korrelations-Matrix-Methode, die für die Detektion von Koinzidenzen auf Einzelmolekülebene entwickelt wurde. Die Methode erweist sich als robust gegen Hintergrundsignale und ist leicht und eindeutig interpretierbar. Zusätzlich kann hiermit eine Kolokalisation von drei oder mehr unterschiedlich gekennzeichneten Objekten quantitativ analysiert werden. Dies ist ein beachtliches Novum auf dem Gebiet der Kolokalisationsanalyse.

Abstract

In the framework of this dissertation, the application of different novel approaches to study protein interactions, is exemplified on the basis of the small glycine-rich RNA binding protein *At*GRP7 from *Arabidopsis thaliana*. This protein is of special interest to the Department of Molecular Cellphysiology, which is a cooperation partner within the collaborative research centre SFB 613. An optimized variant of the reversibly switchable fluorescent protein Dronpa, termed Dronpa-s, was used as a reporter to track the protein's localization in *Arabidopsis* cells, and furthermore, its intra-cellular translocation between the nucleus and the cytoplasm. Therefore, Dronpa-s was fused to *At*GRP7 in transgenic *Arabidopsis* plants. By switching Dronpa-s fluorescence on and off selectively inside the nucleus, a bidirectional nucleocytoplasmic shuttling of *At*GRP7 was visualized and quantified.

Within another branch of this work, the binding affinity of *At*GRP7 to short RNA sequences was quantified *in vitro*, by means of Fluorescence Correlation Spectroscopy. Binding to RNA facilitates the protein, to interact with its transcript inside the nucleus, inducing an autoregulatory inhibition to the own protein bio-synthesis. Results show a weak but specific binding of *At*GRP7 to a short DNA sequence, which resembles a binding site of its own transcript.

The ability of binding to RNA helps *At*GRP7 to participate in stress-related particles, termed processing bodies, upon induction of oxidative stress to *Arabidopsis* cells. This protein interaction was visualized by colocalization studies. Common colocalization parameters failed to reasonably interpret the here provided data. Consequently, a completely novel approach to colocalization detection and quantification was pursued in this work. The here introduced analysis method defines the Γ-norm, which is based on the correlation matrix method, known

from single molecule coincidence studies, brings several benefits to the field of colocalization, like multi-color colocalization, robustness against background noise and improved interpretability.

Contents

1 Introduction

1.1 Fluorescent proteins

In today's fluorescence microscopy the application of fluorescent proteins is widely used. With the discovery of GFP (Green Fluorescent Protein), Chalfie et al. [1994], Shimomura et al. [1962] and Tsien [1998] have rejuvenated research. While most organic fluorescent labels are phototoxic to living cells, fluorescent proteins can be produced intrinsically by cells as part of their protein expression cycle. Even labeling of a fluorescent reporter to a target protein, which usually proves to be difficult and error-prone, is now carried out by the cells themselves.

GFP and other fluorescent proteins (FPs) have been massively used since, to specifically tag proteins in cells. At present, the improved derivative of GFP termed eGFP (enhanced GFP) is by far the most established reporter protein in cell research. The field of application is not just limited to protein localization studies. Moreover, the mobility of proteins fused to FPs can be determined by introducing photobleaching to a defined region of the cell. Subsequently, the transport of other still fluorescing molecules from the surroundings into the bleached region is monitored. This method termed Fluorescence Recovery after Photo-bleaching (FRAP) was first described by Axelrod et al. [1976]. Information on protein mobility can also be gathered by a similar method which monitors the decrease of fluorescence in neighboring regions and is therefore termed fluorescence loss in photobleaching (FLIP) [Lippincott-Schwartz et al., 2001]. Since these methods are limited to the detection of secondary effects after photobleaching, a photoactivatable variant of GFP (paGFP) was engineered allowing to directly monitor the translocation of proteins fused to this reporter

[Patterson and Lippincott-Schwartz, 2002]. However, all these methods induce irreversible photo-manipulation. Recently a new generation of fluorescent proteins, which can be reversibly photoswitched between a fluorescent and a non-fluorescent state, emerged which now pave the way to novel advanced fluorescence imaging techniques. This new class of reversibly switchable fluorescent proteins (RSFPs) combines and further extends the advantages of common and photoactivatable FPs.

In the framework of the collaborative research centre SFB 613 an optimized variant of the reversible photoswitchable fluorescent protein Dronpa [Ando et al., 2004] was engineered and further fused to a specific target-protein in *Arabidopsis thaliana* (*Arabidopsis*) cells. This synthesized derivative of Dronpa was termed Dronpa-s. Within the SFB 613, I therefore closely collaborated with members of the Department of Molecular Cell Physiology during my work. This interdisciplinary collaboration provided access to the interesting field of research on proteomics, i.e. protein structure, function and dynamics. In turn, novel fluorescence based techniques, as presented in this work, were adopted to particular and recent problems which are of special interest to the collaboration partners.

1.2 Target Protein *At*GRP7

Of particular interest is the target-protein *Arabidopsis thaliana* glycine rich RNA-binding protein 7 (*At*GRP7), which is a representative of a class of small glycine-rich RNA-binding proteins with a single RNA recognition motif (RRM). It is part of the endogenous timing system which enables the plant to pre-adopt to periodical environmental changes. Further, it participates in pathogen defense in *Arabidopsis*, presumably via the regulation of mRNA at the post-transcriptional level. The *At*GRP7 transcript (*AtGRP7*) undergoes so-called circadian, i.e. 24-h, oscillations with a peak at the end of the daily light phase. *At*GRP7 regulates these oscillations and thereby its own protein level,

by binding to the transcript and thus causing the production of an alternative splice form with a premature termination codon. The influence of *At*GRP7 on splice-site selection of its pre-mRNA obviously occurs in the nucleus where the transcript is located.

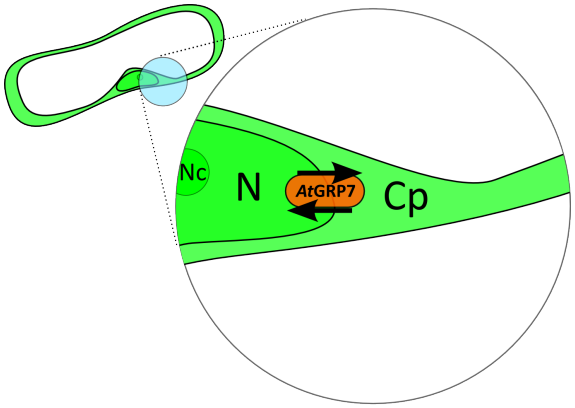

Figure 1.1: Schematic of *At*GRP7 shuttling between cytoplasm and nucleus in a plant cell.
*At*GRP7 is a RNA binding protein which binds to its own pre-mRNA. Since the pre-mRNA is located in the nucleus of the cell (N), *At*GRP7 has to be imported to the nucleus from the cytoplasm (Cp). Therefore, it has to overcome the nuclear barrier.

As proteins are produced in the cytoplasm *At*GRP7 has to somehow overcome the barrier surrounding the cell nucleus, for binding to its own transcript (see figure 1.1). Usually proteins which are imported into the nucleus exhibit a nuclear localization signal (NLS), a special amino acid sequence. The NLS enables strong binding to importin, a protein which helps other proteins to cross the nuclear barrier. Albeit *At*GRP7 lacks a classical NLS, it exhibits a sequence simmilar to a different known nuclear import signal, an M9 domain originally found in mammalian heterogeneous nuclear ribonucleoproteins (hnRNPs). In mammalian cells M9 domains have been reported to facilitate both transport into and out of the nucleus [Bogerd et al., 1999].

The molecular mechanisms of the nuclear import have not been revealed and at present it is not known whether *At*GRP7 is also ex-

ported from the nucleus to the cytoplasm. This bears the obvious question, if *At*GRP7 can get into the nucleus just by diffusion or by active transport processes, involving an M9 domain equivalent in plants.

1.3 Application of photoswitchable proteins in standard imaging techniques

To analyze such protein interactions, in cell biology often fluorescence imaging techniques like the aforementioned FRAP are used. The general problem to this kind of analysis is, that cells are exposed to high laser intensities to efficiently photo-bleach the FPs, often disturbing their physiological function. Photoswitching of RSFPs to the off-state requires much less photons than photobleaching eGFP, allowing FRAP or photoactivation measurements to be performed at much lower excitation intensities, and therefore, inducing less phototoxicity to the cell [Ando et al., 2004]. This work aims to answer the question if RSFPs, like Dronpa-s, can easily be introduced to standard imaging techniques, to replace commonly used FPs efficiently.

1.4 Colocalization analysis visualizing protein interactions

Colocalization studies represent another approach to unravel protein interactions by just providing information on spatial proximity of interaction partners. Therefore, different fluorescent labels are attached to the interaction partners of interest. Thereby, avoiding spectral overlap and any other interactions between the used fluorophores is demanded. Typically, fluorescence images of the such prepared sample are recorded on spectrally separated channels, preferably at the same time. Now, by overlaying the images of the different channels, a merged image denotes sites of colocalization by an additive secondary color. That is, two

merged channels of the primary colors red and green yield the secondary color yellow as a reporter for colocalization.

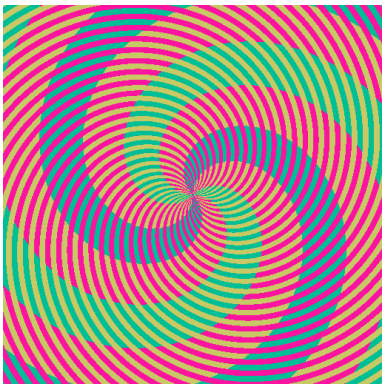

Figure 1.2: Example of the distraction of human vision by colors an shapes.
Most people with healthy vision are consumed by the illusion that the prominent spirals are in shades of green and blue, but they actually have the very same color. [Sample image provided by Fiji]

Due to the shortcomings of human vision, judging by shapes and colors does not suffice to provide reliable information on colocalization. Figure 1.2 demonstrates the problems to be encountered. Approaches to provide an unbiased numerical parameter to indicate and quantify colocalization led to the institution of the at present mainly used Pearson Correlation Coefficient (PCC) and Manders Overlap Coefficient (MOC)[Manders et al., 1993]. Both are not straightforward to apply correctly to image data, and thus, often lead to ambiguous results due to misinterpretation or vague definition of colocalization and noncolocalization. Up to now all implementations of colocalization approaches are limited to determine colocalization between a maximum of two channels. However, in many cases more than two interaction partners are contributing to a specific peculiarity. Thus they have to be examined crosswise. The work at hand presents advances in overcoming these limitations.

2 Theoretical Background

Due to the interdisciplinary nature of this work, the theoretical backgrounds of both, biological and physical subtopics, have to be pointed out. In the following sections a short introduction to fluorescence itself and fluorescence based research methods will be presented. Furthermore the main aspects of the examined biological systems will be mapped in chapter 2.4.

2.1 Principles of Fluorescence

Luminescence being the superordinate effect (besides black body radiation) of light emission by molecules, can be subdivided into several subtypes, i.e. radioluminescence, chemiluminescence and photoluminescence, depending on which effect causes the emission of photons.

Photoluminescence can occur, when a molecule absorbs a photon of the energy

$$E = h \cdot \nu \tag{2.1}$$

with the frequency ν and the Planck constant h. If E is equal or greater than the energy difference ΔE between the ground state S_0 and the first electronically excited state S_1 of the molecule.

The light absorption occurs on a 10^{-15} seconds time scale. Relative to the nuclear movement (10^{-13} seconds) these electronic transitions occur almost instantly which is the keynote to the Born-Oppenheimer

approximation and also accounts for the vertical transitions in the FRANCK-CONDON energy diagramm (figure 2.2).

The excited state endures some 10^{-9} seconds until the molecule relaxes to the ground state by emitting a photon. The fluorescence lifetime is specific for different fluorophores.

The emitted fluorescence photon carries the energy E^*, with

$$E - E_- = E^*. \tag{2.2}$$

Therefore, the maintained energy is composed of

$$E^* = h \cdot \nu^*, \tag{2.3}$$

and

$$\nu^* \leq \nu. \tag{2.4}$$

applies.

Depending on the energy of the incident photon and the energy gaps, the molecule is most often not only lifted to the lowest possible energy state, but to a higher excited vibrational state of the 1^{st} (S_1) or n^{th} (S_n) excited electronic state.

However, according to KASHA's rule fluorescence emission occurs from the lowest electronically excited state, because the energy gaps separating higher excitation levels are close enough for the molecule to decay by *internal conversion*, thus increasing the thermal energy of the surrounding solution. This also explains the common experience of the emission wavelength being independent from the excitation wavelength.

While this rule has some exceptions, it applies for the most molecules. Therefore, the emitted light is commonly red-shifted to the incident light, due to the thermal relaxation prior to the fluorescence process, which is called the STOKES Shift.

Figure 2.1 shows a transition from an excited electronic singlet state to an energetically lower triplet state, termed *intersystem crossing*. This transition implies the need of a change in spin orientation, which is quantum mechanically forbidden.

While the electron is in the triplet state, it can relax to the ground state by undergoing another spin transition and emission of radiation, termed *phosphorescence*. Since this, again, is not allowed, the lifetime of this state is long compared to fluorescence.

Apart from intersystem crossing, there are other concurring processes, which prevent the emission of fluorescence. These processes are termed

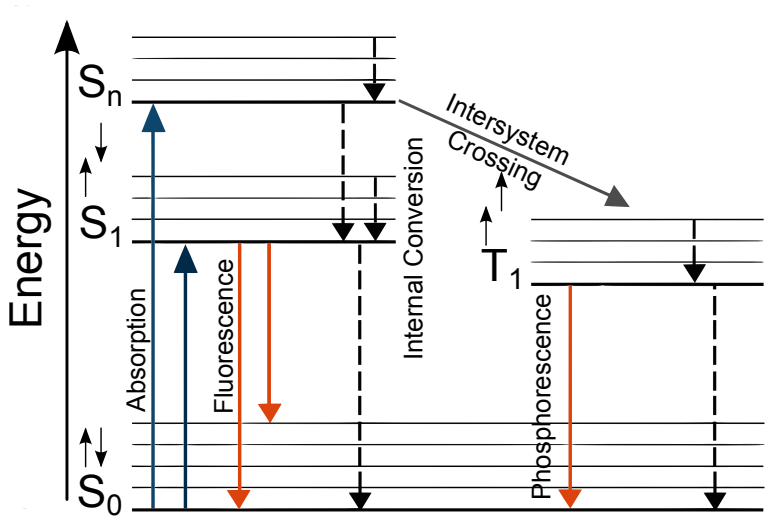

Figure 2.1: Jablonski diagram.
The diagram illustrates the electronic states of a fluorophore and the transitions between them. The vibrational ground states of each electronic state are indicated by thick horizontal lines, the higher vibrational states by thin lines, whereas the electron spin orientation is given by small arrows. Nonradiative relaxations are displayed as black or gray arrows between electronic states. Along with all nonradiative relaxations the phosphorescence, which is the radiative relaxation from the triplet state (T_1) to the singlet ground state (S_0), is competitive to the fluorescence relaxation.

quenching mechanisms, which will be described in chapter 2.2.2 on page 15. All the concurring processes can be described as the rate k_{NR} of nonradiative relaxation processes from S_1 to S_0. In analogy the rate of radiative relaxation processes can be defined as k_R, being the fluorescence rate. The sum of these rates gives the inverse of the average time a molecule spends in the first excited state, also termed fluorescence lifetime τ_{Fl}.

$$\tau_{Fl} = \frac{1}{k_R + k_{NR}} \tag{2.5}$$

For the absorption and emission of photons, the Franck-Condon principle gives information on probabilities for the respective transitions, plotted vertically in the Franck-Condon diagram, depicted in figure 2.2. The transitions will occur most likely, if the two vibrational

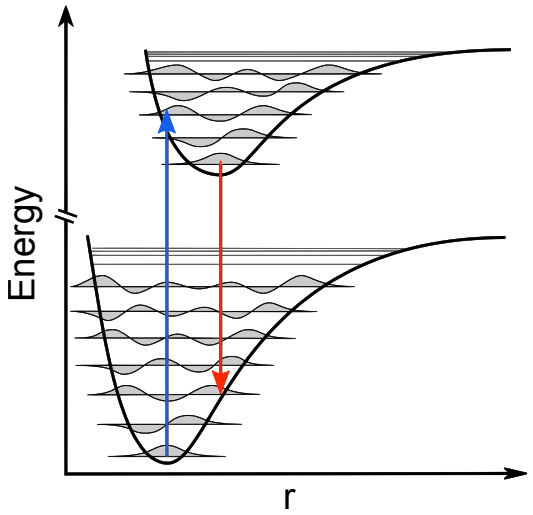

Figure 2.2: Franck-Condon diagram.
Possible transitions between electronic states of a molecule most often occur between overlaps of vibrational wave functions. Transitions happen too fast for the nuclear coordinates r to change.

wave functions significantly overlap. This explains the mirror-symmetry

of absorption- and emission spectra known from most fluorescing compounds. The varying transition probabilities result in an inhomogeneous distribution of photon energies, that are absorbed and emitted, as can be seen in figure 2.3.

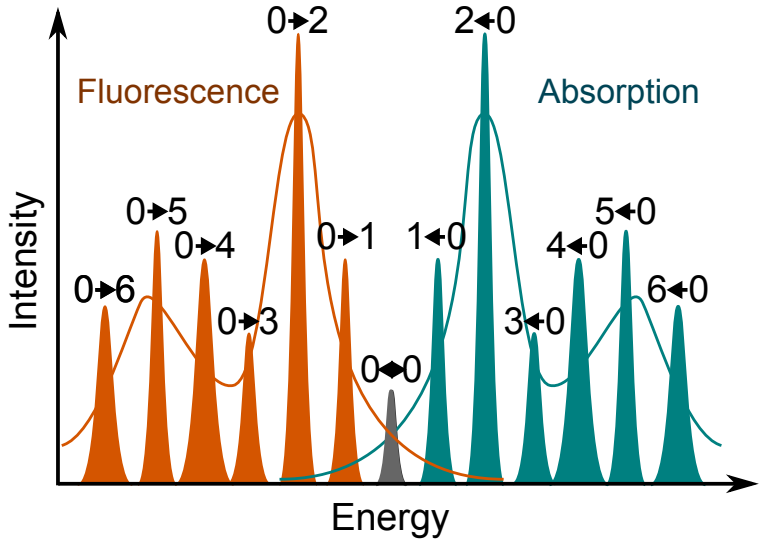

Figure 2.3: Probabilities of electronic transitions in absorption and emission processes (cf. figure 2.2). Excitation and emission probabilities are mirrored, as well as the resulting spectra.

2.2 Fluorescence Spectroscopy

Fluorescence spectroscopy aims to identify and/or quantify molecules by their fluorescence characteristics. This is rendered possible, as each molecule has characteristic absorption and emission spectra due to the specific composition of electronic and vibrational states.

A class of molecules which feature most suitable fluorescence characteristics for spectroscopic purposes is highlighted in the following section.

2.2.1 Fluorophores

Molecules considered as fluorophores meet special needs for efficient fluorescence generation an detection. Therefore they feature a reasonable *quantum yield* Φ, defined as ratio of emitted fluorescence photons to absorbed excitation photons. Φ can also be defined with the relaxation rates given in equation (2.5):

$$\Phi = \frac{k_R}{k_R - k_{NR}} \tag{2.6}$$

Depending on the method of detection, the spectral range of fluorescence can be of importance. Most fluorophores emit visible or near visible light.

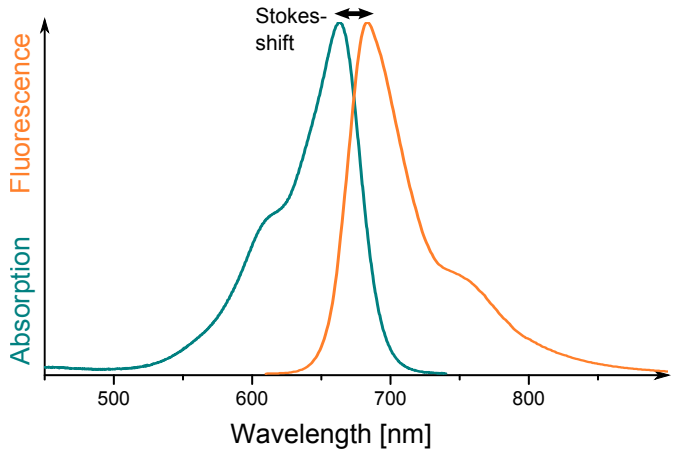

Figure 2.4: Absorption and emission spectra of the artificial fluorophore Atto655 [AttoTec].

Besides the many natural organic dyes, synthetic fluorophores have been designed. Therefore, a wide range of the spectrum is crowded by according fluorescence emitters. Especially the visible spectrum is consistently covered. Figure 2.4 shows absorption and emission spectra of one of these fluorophores, named Atto 655 (AttoTec, Germany). The STOKES shift (see chapter 2.1) of 19 nm between absorption and emission maxima, can clearly be seen.

While the most molecules of interest to natural sciences have inferior fluorescence abilities, fluorophores are attached to those molecules as a fluorescent marker. Thus identification and quantification of even non-fluorescing molecules can be afforded by fluorescence spectroscopy.

2.2.1.1 Fluorescent Proteins

Attaching a fluorescent marker to a target molecule can be a difficult task under certain conditions. Most problems evolve from the urge to mark bio-molecules inside living cells, sustaining cell life at best. Therefore it was a revolution to natural science, when Osamu Shimomura was to discover the Green Fluorescent Protein (GFP) in 1962. Being a protein from the jellyfish *Aequorea victoria*, a gene in the *Aequorea* genome encodes for GFP. It was just a question of time, until the gene's nucleotide sequence was published by Prasher et al. [1992]. Two years later Chalfie et al. [1994] succeeded in expressing recombinant GFP in *E. coli* and *C. elegans*. Eventually the (by then poor) spectroscopic abilities of GFP were enhanced in the lab of Roger Tsien [Heim et al., 1995]. From there GFP raised its importance as a widely-used tool in natural sciences. Several GFP mutants were engineered to feature either further enhancement or even different emission wavelengths. Thus, by the beginning of the 21st century a broad spectrum of fluorescing proteins, emitting various colors of light, were available.

All these fluorescent proteins have the huge advantage of not only being applicable for *in vivo* applications but furthermore, enabling intrinsic tagging bio-molecules with a *fluorescent reporter* by the organism itself. Therefore, the fluorescent reporter is genetically fused to a target protein inside a transgenic organism. This *fusion protein* is translated in one go.

Besides all advantages, fluorescing proteins have general drawbacks compared to synthetic fluorophores, like low quantum yields and poor photostability. Also they are limited in size. While not all

of them are available as monomers, even a monomeric GFP-like protein is of reasonable size. At the margin this can result in fusion proteins, where the reporter is several times bigger than the target. This may alter the target's properties immensely, yielding artifact results.

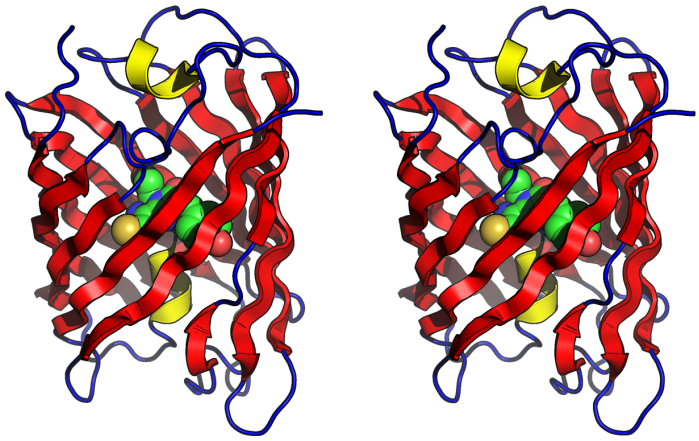

Figure 2.5: Stereoview of a Dronpa molecule.
Dronpa molecule (`PDB-2IOV`) was visualized with `PyMOL` [Andresen et al., 2007, DeLano, 2002]. The common barrel structure is shared by most fluorescing proteins. Here the 'barrel' consists of 11 β-sheets enclosing the chromophore tripeptide which is pictured in detail in figure 2.6. 3D immersion by crosseye stereoview.

In 2004 Ando et. al. could deliver a photoswitchable fluorescent protein, which was named Dronpa after *dron*, a ninja term for vanishing, and pa for photo-activation. This protein can be reversibly switched to a dim state featuring low fluorescence and a bright state with high fluorescence intensities. The switching occurs by irradiation with light of different wavelength as shown in figure 2.6.

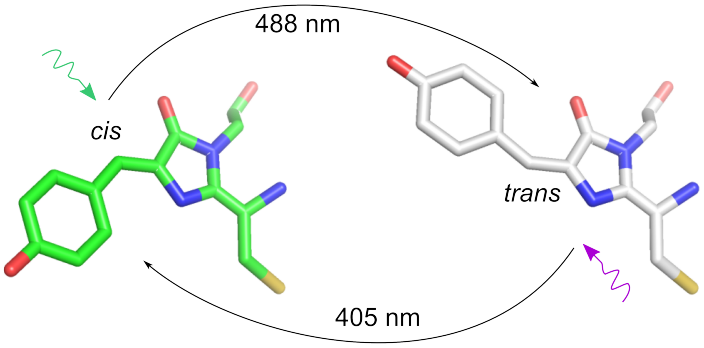

Figure 2.6: Stick model showing light-induced *cis*/*trans* isomerization of the chromophore in Dronpa.
The chromophore of Dronpa is formed by the tripeptide Cys-62–Tyr-63–Gly-64 (CYG). In the fluorescent state the chromophore adopts a *cis*-conformation, while it adopts the *trans*-conformation in the dim state. The isomerization is induced by light of different wavelengths. Thus blue light induces transition to the dim state and UV light again restores the bright state.

2.2.2 Fluorescence Quenching

As described before, processes which diminish fluorescence are called quenching. If another molecule is involved by causing the quenching, this molecule is referred to as *quencher*. *Collisional* or *dynamic quenching*, occurs when an fluorophore, while excited, hits another molecule in the solution. Often molecular oxygen acts as quencher this way [Kautsky, 1939].

The process of dynamic quenching can be described by the Stern-Volmer equation:

$$\frac{F_0}{F} = 1 + K \cdot [Q] = 1 + k_q \cdot \tau_0 \cdot [Q], \tag{2.7}$$

where F_0 and F are the fluorescence intensities with and without quencher respectively. K is the Stern-Volmer quenching constant, $[Q]$

the concentration of the quencher molecules, k_q the quencher rate coefficient and τ_0 the lifetime of the un-quenched fluorophore.

Furthermore, fluorophores and quenchers can build non-fluorescent complexes, which is termed *static quenching*. This can be described by

$$\frac{F_0}{F} = 1 + K_S \cdot [Q], \tag{2.8}$$

with the association constant K_S. Which can be expressed by

$$K_S = \frac{[F_0]}{[F] \cdot [Q]} - \frac{1}{[Q]}. \tag{2.9}$$

Photoinduced electron transfer (PET) is one of various quenching processes.

In PET redox interactions between a fluorophore and its quencher yield a two stepped electron transfer. This demands a very close distance between both molecules [Marcus and Sutin, 1985]. This is emphasized by the Rehm-Weller equation

$$\Delta G_{CS} = E_{ox} - E_{red} - E_{0,0} - \frac{e^2}{\varepsilon \cdot d} \tag{2.10}$$

where ΔG_{CS} is the discharged energy, E_{ox} the oxidation potential, E_{red} the reduction potential and $E_{0,0}$ the energy of the electron transition from S_0 to S_1 state. The term $\frac{e^2}{\varepsilon \cdot d}$ is the solvent effect with ε the dielectric constant and d the charge separation distance.

By excitation the former lowest unoccupied molecular orbital (LUMO) of the fluorophore, it turns into a singly occupied molecular orbital (SOMO). Next the fluorophore is reduced or oxidized by the quencher. In case of oxidation the electron on the SOMO of the fluorophore is transferred to the LUMO of the quencher (1), thus turning it into a SOMO, too. From the SOMO of the quencher the electron can be transferred to the former highest occupied molecular orbital (HOMO)

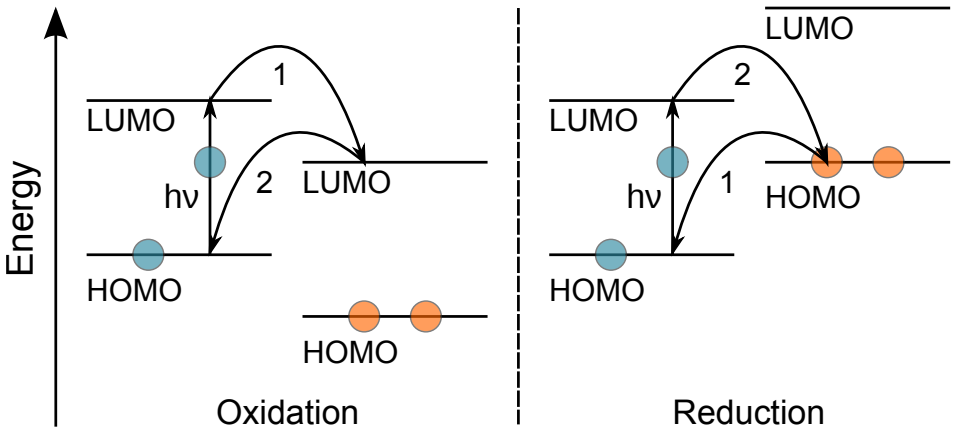

Figure 2.7: Photoinduced electron transfer between fluorophore and quencher. By excitation an electron on the highest occupied molecular orbital (HOMO) of the fluorophore is promoted to the lowest unoccupied molecular orbital (LUMO). After that the fluorophore can be oxidized or reduced by an appropriate quencher in close contact. Two non-radiative electron transitions occur, restoring the initial state of both molecules thereby.

of the fluorophore (2), thereby restoring the initial state. In case of reduction an electron is promoted from the HOMO of the quencher to the former HOMO of the fluorophore (1), as depicted in figure 2.7. Now the electron on the SOMO of the fluorophore restores the initial state by migration to the former HOMO of the quencher (2). All of these electron transitions are radiation-less processes.

2.2.3 Fluorescence Correlation Spectroscopy

The advantage of kinetics on the molecular level, arising on characteristic time scales, is taken by Fluorescence Correlation Spectroscopy (FCS) [Magde et al., 1974]. In figure 2.8 those kinetics are depicted on the respective time scales. Beginning with *antibunching*, the rate at which fluorescence photons can be emitted by the fluorophore, and solvent reactions or conformational changes, on the sub-ns to ns time scale. Furthermore, photophysical processes, like triplet transition,

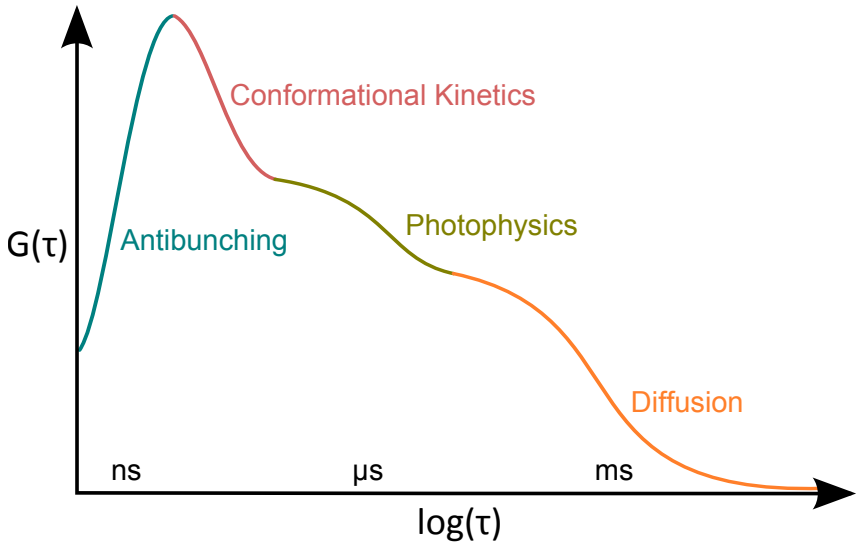

Figure 2.8: Autocorrelation function used for FCS analysis. The sketched function spans multiple time scales from the nano second regime to seconds. Different kinetics can be identified on the respective time scales.

mainly occur in the µs regime, whereas diffusional processes take place in the ms range.

The most common approach to FCS measurements, can be realized on a confocal setup, as described in chapter 2.3 on the next page. Assuming a Gaussian intensity profile, the excitation volume can be approximated by

$$I(\vec{r}) = I_0 \exp\left(-\frac{2(x^2+y^2)}{(\omega_{xy})^2} - \frac{2z^2}{(\omega_z)^2}\right), \tag{2.11}$$

with the axial and lateral diameters of the excitation volume ω_{xy} and ω_z respectively.

Then the auto correlation function is given by

$$G(\tau) = \bar{N}^{-1} \cdot \left(1 + \frac{\tau}{\tau_D}\right)^{-1} \left(1 + \frac{\tau}{\omega^2 \tau_D}\right)^{-\frac{1}{2}} \prod_{i=1}^{n} 1 + K_i \cdot \exp \frac{\tau}{\tau_{Ki}}\,, \quad (2.12)$$

where $\bar{N}$ is the mean number of fluorescing particles in the detection volume, τ_D the characteristic diffusion time and the aspect ratio of the excitation volume $\omega = \frac{\omega_z}{\omega_{xy}}$. $K_i = \frac{k_{A_i B_i}}{k_{B_i A_i}}$ are the equilibrium constants and $\tau_{Ki} = (k_{A_i B_i} + k_{B_i A_i})^{-1}$ the characteristic times for n additional processes of interest (cf. figure 2.8 with $n = 3$).

The *signal to noise ratio* (SNR) of a FCS experiment is determined by

$$SNR = \frac{G(\tau)}{\sqrt{\text{var}\,(G(\tau))}} \approx G(\tau)\nu\bar{N} \propto \nu\sqrt{T}\,, \quad (2.13)$$

with the mean number of photons emitted by each molecule per time interval ν, and T the total number of time intervals during the experiment. As can be seen, the SNR improves with the total duration of the experiment and the number of photons per particle. The latter is highly dependent on the quantum yield of the molecule or its fluorescent marker (see chapter 2.2.1 on page 12).

2.3 Fluorescence Microscopy

The unaided human eye can barely resolve structures of less than half a millimeter. For resolving smaller objects, some kind of microscope has to be applied. But also light microscopy has its limits in resolution. This manifests in the diffraction limit, found by Ernst Abbe in 1873 as

$$d = \frac{\lambda}{2NA} = \frac{\lambda}{sin\alpha \cdot 2n} \quad (2.14)$$

with the radius of a minimal projected spot d, the wavelength λ and the numerical aperture of the objective NA. Where α is the opening angel and n the refractive index of the optical medium separating objective and sample.

This also complies with the RAYLEIGH criterion. The smallest possible point light source displayed by a circular aperture yields a projection in form of an AIRY disc. The lateral intensity profile is then termed *point spread function* (PSF), which is mathematically described by a BESSEL function of first kind and first order. The distance between the main maximum and the first minimum of a PSF is the RAYLEIGH criterion

$$d_{Airy} = \frac{0.61\lambda}{NA} \approx \frac{\lambda}{2NA}, \tag{2.15}$$

which defines the smallest possible, still resolvable distance between two point light sources (see figure 2.9).

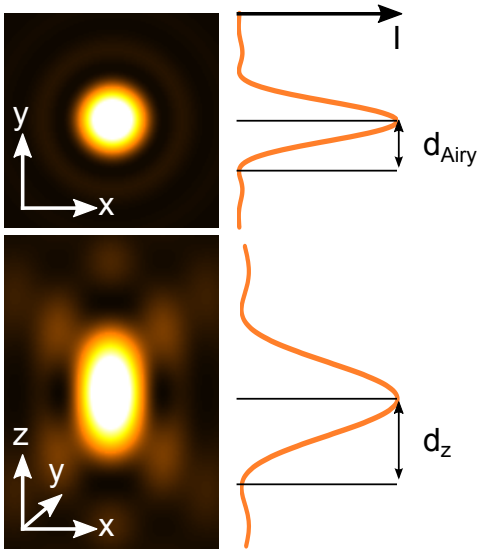

Figure 2.9: Diffraction image of a point light source.
The x-y plane exhibits the characteristic AIRY disc pattern. Intensity profiles are given on the right, with respective distances denoted, which define the lateral and axial resolution.

With the three-dimensional diffraction image of a point light source the axial resolution can be defined analogously, again by the axial distance from the central maximum to the first minimum

$$d_z = \frac{\lambda \cdot 2n}{NA^2} \tag{2.16}$$

Due to that in microscopy two parameters are pushed to the limits for enhancing resolution. First of which, the *NA* of an objective, has reached typical values of 1.4 in research and even 1.7 *NA* objectives are available by now. The second parameter λ was pushed to new limits by changing from light microscopy to electron microscopy, as electrons have a by four magnitudes smaller wavelength than photons.

However, in live cell imaging, fluorescence microscopy still is state of the art and commonly used, as shorter wavelengths are always a trade-off between higher resolution and harming the living system by high energy radiation. Hence, there is a lot of effort to further increase the resolution in fluorescence microscopy.

This can be achieved by the limitation of the *field of view* or *detection volume*. One approach to realize a thus enhanced resolution is the *confocal laser scanning microscopy* (CLSM).

The Confocal Principle

In CLSM a laser beam is focused on the sample by an objective. The emitted fluorescence is collected by the same objective and focused on the aperture of a *pinhole*. Thereafter the fluorescence light is collimated and focused on a single point detector. By the pinhole a small detection volume is defined in overlapping with the focal volume. Thus, only fluorescence and scattered light out from the detection volume can pass the pinhole to reach the detector, as pictured in figure 2.10.

For imaging purposes the sample has to be scanned. That way an image can be constructed out of the intensity values for each scanned coordinate in three dimensions. Therefore, 2D or 3D images of the sample can be generated. The scanning is done either by moving the laser beam over a static sample, or moving the sample over a static beam.

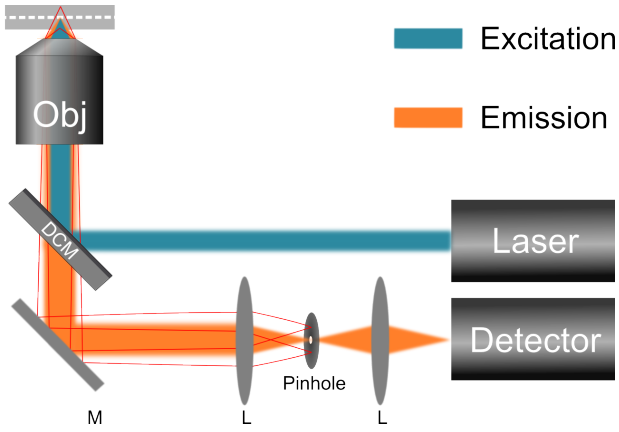

Figure 2.10: Standard confocal microscope.
Laser light is focused by an objective (Obj) on a sample. Fluorescence light is collected by the same objective. A *dichroic mirror* (DCM) separates the laser light from the red-shifted fluorescence light (cf. STOKES shift in chapter 2.1). A lens (L) focuses the fluorescence light on a pinhole, which acts as a spacial filter. Finally, it is focused again on a point-detector.

The resolution in confocal microscopy is enhanced by a factor of 1.41 in relation to standard wide field microscopy.

Another approach to limit the detection volume is total internal reflection (TIRF) microscopy .

Total Internal Reflection Fluorescence Microscopy

If light passes through two different optical media, it changes its direction at the interface, according to the difference in the refractive indices of the two media. This is described by the SNELL'S law:

$$\frac{n_1}{n_2} = \frac{sin(\alpha_2)}{sin(\alpha_1)}, \tag{2.17}$$

with n_i the refractive indices of the media and α_i the beam angles in the different media, as sketched in figure 2.11.

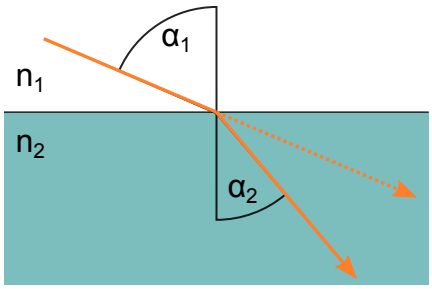

Figure 2.11: Refraction of light upon change of refractive indices.

The largest possible angle of incidence which still yields a refracted ray of light is referred to as the *critical angle*. Under this condition the refracted ray propagates along the interface of the two optical media. The incident light gets totally reflected, as the angle is further increased. In this case an *evanescent wave* in the medium with lower refractive index emerges. The penetration depth of this wave is given by

$$d = \frac{\lambda_0}{4\pi} \cdot \left((n_2)^2 \cdot sin(\alpha_2) - (n_1)^2 \right)^{-\frac{1}{2}}, \tag{2.18}$$

with the vacuum wavelength λ_0 of incident light. The intensity of the evanescent wave is a function of the distance z from the interface

$$I(z) = I_0 \cdot e^{\frac{-z}{d}}, \tag{2.19}$$

where I_0 is the initial intensity at the interface .

In TIRF microscopy this is utilized to limit the excitation volume. Therefore, a laser beam is focused on the back focal plane of an objective with a high *NA*. When the beam is then shifted close to the margin of the objectives aperture, it is deflected and collimated. Eventually the beam is totally reflected at the interface, under an incident angle bigger than the critical angle. This results in an evanescent field, emerging in

the sample, with a penetration depth of only some 100 nm, depending on the parameters mentioned above.

2.4 Biological Background

A quite remarkable part of this work findings in molecular biology are presented. Thus a short summary of the corresponding fundamentals is given in chapter 2.4.1 and chapter 2.4.2. First of which gives an introduction to the structure and function of nucleic acids, whereas the second delivers insight into the synthesis of proteins within a cell.

2.4.1 Structure of Nucleic Acids

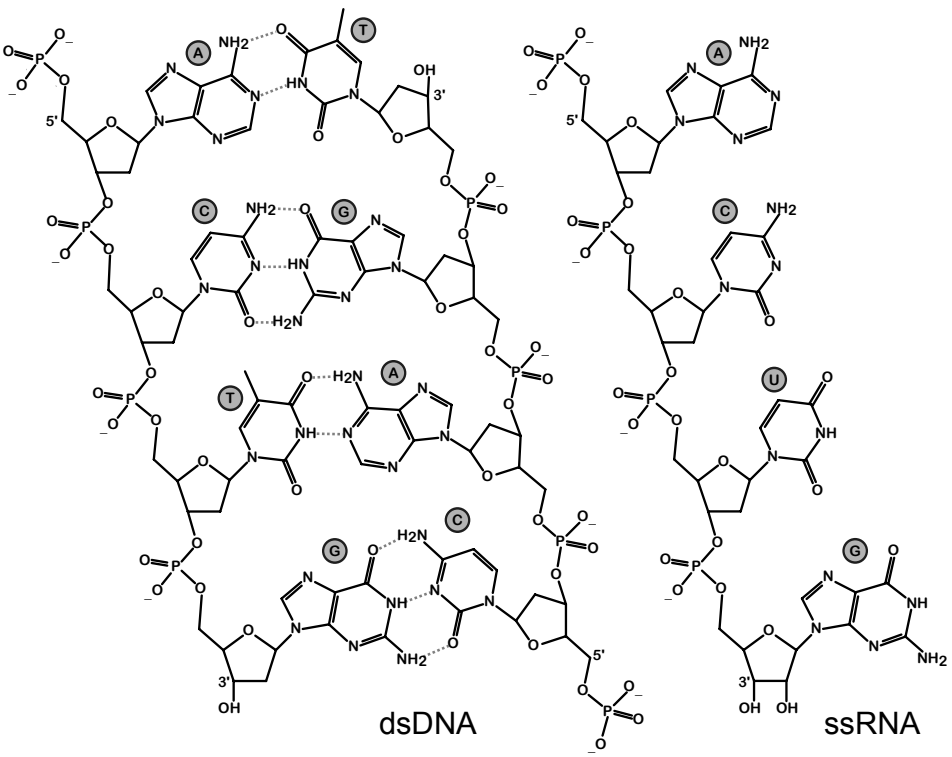

Figure 2.12: Chemical Structure of DNA and RNA.
Bases are identified by the encircled abbreviations. In RNA the thymine (T) is replaced by uracil (U). H-bonds are denoted by dotted lines.

Desoxyribonucleic acid (DNA) and ribonucleic acid (RNA) are to be found in every single organism, providing the storage and delivery of genetic information. Both types of nucleic acids consist of nucleotide sequences and are therefore called *polynucleotides*[1].

Each nucleotide is composed of a backbone, consisting of a sugar[2] and a phosphate group, and a nucleobase attached to the sugar. This structure gives rise to the pairing of two complementary nucleobases, as hydrogen bonds (h-bonds) form amongst them.

In DNA the sequence of the nucleobases adenine (A), cytosine (C), guanine (G) and thymine (T) encodes *genetic information*. In RNA thymine is replaced by uracil (U). The nucleobases are subdivided in pyrimidines (Y) and purines (R), while A and G are purines and C, T and U pyrimidines. Thus the complement to a pyrimidine is a purine, which leads to the pairing of A and T[3] with two h-bonds as well as G and C with three h-bonds in between (cf. figure 2.12). This most common binding pattern is termed Watson-Crick base pairing. However, other binding patterns exist[4], yielding more complex tertiary structures.

In most cases the DNA is available as a double strand (ds) composed of two anti-parallel DNA strands bound to each other due to base pairing of complementary nucleobases. Each DNA strand has two ends which differ in orientation of the terminal sugar molecule. While one end exhibits the 3' carbon the other end exhibits the 5' carbon, as depicted in figure 2.12. Thus each polynucleotide strand features one *3'-end* and one *5'-end*. Hereby the direction of a strand can be defined. In dsDNA the two complementary strands are of opposite direction. This gives rise to the double-helical structure of DNA (see figure 2.13 a) which was first discovered by James Watson and Francis Crick in 1953.

In contrary to DNA RNA is most often available as a single strand (ss).

[1] Short strands of nucleotides are called *oligonucleotides* (*oligos*) accordingly.
[2] 2-desoxyribose in DNA and ribose in RNA
[3] U in RNA respectively
[4] i.e.: Hoogsteen base pairs and wobble base pairs

H-bonds between base pairs in ssRNA account to the building of secondary structures like *hairpin-loops* (see figure 2.13 b).

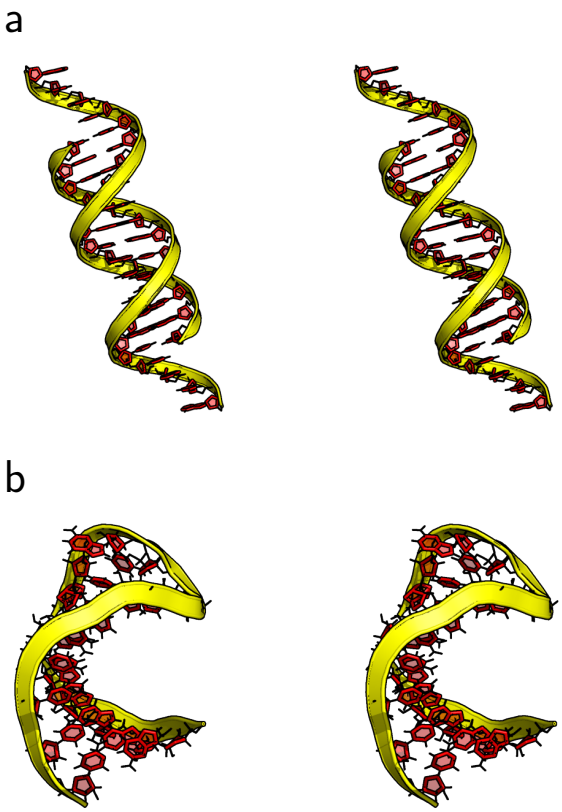

Figure 2.13: Stereoview of DNA double helix and RNA hairpin-loop. DNA and RNA structures were calculated with `make-na server` and `MC-fold` respectively. The generated models were visualized with `PyMOL` [DeLano, 2002, Parisien and Major, 2008]. 3D immersion by crosseye stereoview.

2.4.2 Protein Biosynthesis

Protein biosynthesis is a multi-step process. First the genetic information is transcribed from DNA to RNA which, in a second step, is translated into aminoacid sequences. These are the building blocks of proteins. The whole process is also termed *gene expression*.

2.4.2.1 Transcription

The transcription is performed by the RNA polymerase (RNAP)[5], which binds to one of both strands in dsDNA, the so called *template strand*[6]. This binding region is called *promoter*. Transcription starts from the 3'-end of the promoter, thus the opposite *coding strand*[7] of the DNA is copied. As a result the *pre-mRNA* is assembled from 5'-end to 3'-end.

If a gene codes for a protein the pre-mRNA is termed *transcript* of the protein. Genes can be enhanced or silenced, meaning the expression of the gene is promoted or suppressed respectively. Therefore, regulatory sequences termed *untranslated regions* (UTR) upstream (5'UTR) and downstream (3'UTR) of the coding region in a DNA strand can direct the gene expression accordingly. These regions are also transcribed to the pre-mRNA and, as they lack gene coding information.

Splicing

In eukaryotic cells a further step in RNA processing can occur. If the pre-mRNA sequence between 5'UTR and 3'UTR contains *introns* a process termed *splicing* takes place. In the process of splicing the intron regions are removed, leaving the remaining *exon* regions to build up the thereby matured mRNA, which is illustrated in figure 2.14. The mature mRNA can be translated to a protein in a following process. In eukaryotic cells the complete transcription takes place inside the nucleus, the organelle which holds the DNA.

For the final protein synthesis the mature mRNA has to leave the nucleus and enter the cytoplasm of the cell, where the translation takes place.

[5] In eukaryotic cells there is more than just a single type of RNAP.
[6] Also termed anti-sense strand.
[7] Also termed sense strand.

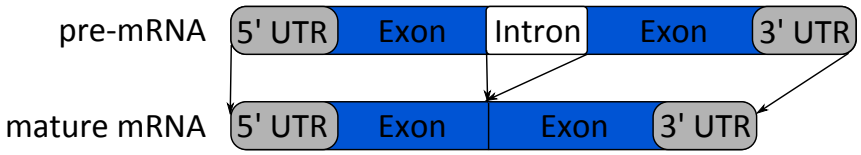

Figure 2.14: Maturation of pre-mRNA by splicing.
Depicted is a pre-mRNA strand with a 5' exon, an intermediate intron and a 3' exon. The non-coding intron is cut out, while the remaining exons build up the mature mRNA.

2.4.2.2 Translation

As polypeptides or proteins consist of amino acids, the nucleic alphabet of four characters has to be translated into the amino acid alphabet. While there are 22 proteinogenic amino acids which can build proteins, only 20 of them are directly encoded. Thus, the amino acid alphabet consists of 20 characters. A translation from genetic code into amino acid code is warranted, hence a specific sequence of three nucleotides ,termed codon, each encodes for a specific amino acid yielding $4^3 = 64$ different possible codons. Only three of all possible codons do not encode for amino acids. Therefore, most amino acids are encoded by more than one codon. Thus, the genetic code is referred to as degenerated. However, most organisms feature a characteristic preference of one or two codons over the other codons to encode for a specific amino acid, which is reflected in the organism's DNA sequence.

The three codons not encoding for an amino acid, are termed *stop-codons*[8], as they induce the termination of the polypeptide chain elongation in the *C-terminal end* featuring a free carboxyl group. In analogy the other end of the polypeptide is termed *N-terminal end*, as it exhibits a free amine group.

[8]The stopcodons are: UAA, UAG and UGA

2.4.3 Circadian Rhythms in Plants

Virtually all organisms have to adapt to the 24 hour light-dark cycle in consequence to the rotation of the earth. Consequently many higher organisms evolved internal clocks with circadian rhythms which enable them to pre-adapt to periodic environmental changes. On exemplary benefit plants are enabled to synthesize all proteins needed for photosynthesis right before dawning, thus prolonging the period of effective photosynthesis during daylight.

The complex structure of the internal clock can be abstracted by defining three greater sections. These sections termed *input pathway*, *main oscillator* and *output-pathway* are sketched in figure 2.15.

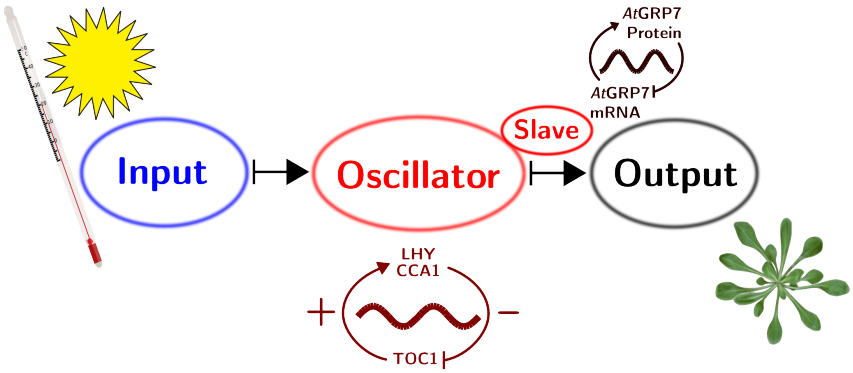

Figure 2.15: Scheme of the internal clock of *Arabidopsis*. The internal clock is subdivided into an *input pathway*, where external stimuli start resp. reset the clock, an *oscillator*, setting the pace, and the *output pathway*, where the phenotypic response is generated.

Here the input pathway describes the reception of endogenous signals mainly in form of light and temperature. These signals are carried further downstream to the main oscillator, where the signal may induce the expression of so called *clock proteins*. These proteins interact with each other, generating a circadian rhythm of about 24 hours. This oscillation is directed downstream, promoting expression of *clock related proteins* like *At*GRP7, which possibly generate oscillation

themselves, thus being termed *slave-oscillators*. All these oscillating signals eventually trigger phenotypic response, preparing the plant for changes in the environmental conditions.

On the molecular level the oscillations of the main oscillator are generally generated by *feedback-loops*. These are afforded by enabling or disabling gene expression on the transcriptional level, regulation on the posttranscriptional level by i.e. alternative splicing, or direct protein modification on the posttranslational level.

In *Arabidopsis*, a largely used model organism for higher plants in general, the master-oscillator consists of the main clock proteins LHY (Late Elongated Hypocotyl), CCA1 (Circadian Clock Associated 1) and TOC1 (Time of CAB Expression 1). These proteins interact in interlaced positive and negative feedback loops. TOC1 exhibits a maximum expression level in the evening hours, due to the so called *evening event* (EE) embedded inside its promoter (cf. chapter 2.4.2.1 on page 28). The EE is built by the sequence `AAATAACT` which can be found in the majority of genes with their expression peak in the evening [Harmer et al., 2001]. The expression of both LHY and CCA1 is induced by TOC1, resulting in a maximum expression during the morning hours, and therefore, phase shifted to that of TOC1. Furthermore, CCA1 and LHY both bind to the TOC1 promoter, causing a repression of TOC1 protein expression [Alabadí et al., 2002]. However, LHY and CCA1 additionally repress their own as well as the other's gene expression, again by binding to the respective promoter. Besides this feedback-loop there are further affiliated regulation loops called *morning loop* and *evening loop* [see Farré et al., 2005, Fujiwara et al., 2008, Kim et al., 2007, Locke et al., 2005, Para et al., 2007, for futher reading]. These multiple regulation pathways yield the stable contrariwise oscillation of the three proteins throughout the day.

The next section introduces *At*GRP7, a small protein whose transcription is subject to this circadian rhythmicity.

2.4.4 Glycine-rich RNA-binding Proteins in *Arabidopsis*

*At*GRP7 is a small glycine-rich RNA binding protein in *Arabidopsis*. RNA binding proteins are highly conserved in plants, animals and also in the human genome. They regulate gene expression on the post transcriptional level and influence maturing, modification and degradation of mRNA. Schmidt et al. [2010] described this regulation processes to aid the plant in resisting abiotic and biotic stress.

Under cold conditions *At*GRP7's gene expression is induced. The protein increases stress tolerance by causing the closing of stomata.

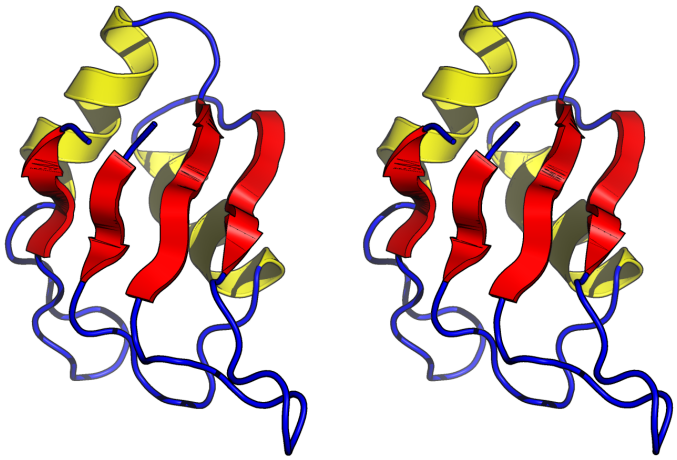

Figure 2.16: Predicted structure of *At*GRP7 without its glycine stretch.
The protein's binding pocket is built up of four β-sheets (red) which are lined up by two α-helices (yellow). Connecting random coil amino sequences are also shown (blue). The two centric β-sheets hold a RRM sequence each (cf. Sequence 2). The structure was predicted by homology modeling with `CPHmodels` [Nielsen et al., 2010]. 3D immersion by crosseye stereoview.

However, under dehydration and salt stress conditions *At*GRP7 promotes the opening of stomata.

Furthermore, a role in immune response mediation is assumed, because *loss of function* mutants show an increased susceptibility to pathogens. Along with that, a reduction of mRNA export from the nucleus was observed, as well as late flowering of the mutants, suggesting an interaction with the autonomous flowering pathway.

*At*GRP7's function in the immune response pathway is presumably aided by the influence of the circadian rhythmicity, as it was found to be a clock related protein itself and part of a so called *slave oscillator* downstream the master oscillator [see Heintzen et al., 1997].

Staiger and Apel [1999] found the promoter of *At*GRP7 to feature two domains giving rise to the rhythmic expression of its protein. Later on one of these domains was identified as EE by Harmer et al. [2001].

*At*GRP7 regulates the circadian oscillations of its own transcript *AtGRP7*. The transcript concentration in *Arabidopsis* peaks 8-12 hours after illumination (input pathway), while *At*GRP7 protein achieves peak levels 4 hours later. This shifted oscillation indicates a negative auto-regulation that is considered to be initiated by *At*GRP7 binding to its own pre-mRNA (cf. chapter 2.4.2.1 on page 28). This binding induces an alternative splicing, which results in an alternate transcript featuring a premature stopcodon (cf. chapter 2.4.2.2 on page 29). Thus the translation is aborted too early, yielding a non-functional protein, which is sketched in figure 2.17.

Furthermore, the transcript is subject to the *nonsense mediated decay* showing a shorter half life than the correctly spliced transcript, as described by Schöning et al. [2008]. Staiger et al. [2003] identified this negative auto-regulation as the propulsive force according for the persisting oscillation of *At*GRP7 and its transcript.

The correctly spliced and translated *At*GRP7 features a N-terminal RRM and a glycine stretch at the C-terminus. The RRM is built up by the two Ribonucleoprotein (RNP) domains RNP1 and RNP2, and accounts for binding to the pre-mRNA. Furthermore, the glycine stretch

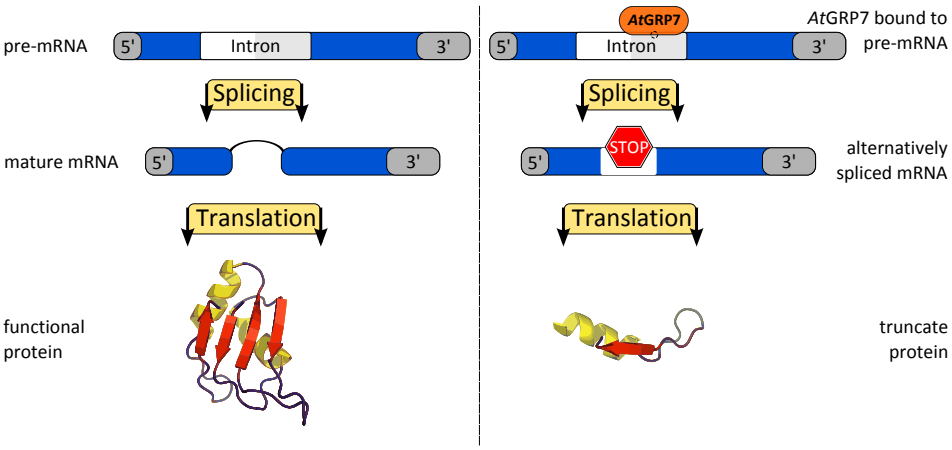

Figure 2.17: Alternative Splicing of *AtGRP7* in comparison to correct splicing.
*At*GRP7 induces alternative splicing by binding to its own transcript (top right), resulting in a mRNA with a premature stopcodon, which is translated to a non-functional truncated protein. Thus *At*GRP7 negatively regulates its own expression.

holds a M9 domain, which accounts for intra-cellular transport of *At*GRP7, as described by Ziemienowicz et al. [2003].

Figure 2.16 shows the predicted structure of *At*GRP7 omitting the glycine stretch, as no sufficient data exists for structural elucidation. RNP1 and RNP2 each locate to one of the two central β-sheets, forming the binding motif.

The amino acid sequence of *At*GRP7 is shown in Sequence 2, with highlighted RNPs and the predicted domain. Sequence 1 shows the nucleotide sequence of *AtGRP7* with highlighted binding sites accordingly. Prior to this work, two binding sites have been roughly identified via depletion analysis and Electrophoretic mobility shift assay (EMSA) [Schöning et al., 2007, Staiger et al., 2003]. They locate to the 3'UTR and the second half of the intron. The 3'UTR binding site was further investigated by Schüttpelz et al. [2008].

Sequence 1: *AtGRP7* nucleotide sequence.
UTR is displayed in gray, binding regions in orange and exons in blue.

```
   1 CUUCGUCUAC AUCGUUCUAC ACAUCUCACU GCUCACUACU CUCACUGUAA
  51 UCCCUUAGAU CUUCUUUUCA AAUUUCAAUG GCGUCCGGUG AUGUUGAGUA
 101 UCGGUGCUUC GUUGGAGGUC UAGCAUGGGC CACUGAUGAC AGAGCUCUUG
 151 AGACUGCCUU CGCUCAAUAC GGCGACGUUA UUGAUUCCAA GGUCUGUUAC
 201 ACGCCGAGAU CGGACUCCGA GUGAUAUCGA UGAUCUCAUC CUCGACGGAU
 251 CUGUUCCGAU CUUGUGUUUC UCUGUUACUU GAUUCGAUUA CUCUGUUACU
 301 AUUCUCGUUC UUUGUUACUA CUACUACUAC UACUGUUACU UGUAUUUUCC
 351 CAAAUCGGUA CGUUCAUCUU CCUGCUUCUG UGAGCCCGGA GAUCGAUCGG
 401 AUUUUUUUGU AUUUUGUAUA UUUGUUGUAG AUCUAAAUGC UUUUGUUCAG
 451 UUUUGUUGGA UUGUUUUGCU GAUCUGGUUU UUGUAUUAUU UGGAUAACAG
 501 AUCAUUAACG AUCGUGAGAC UGGAAGAUCA AGGGGAUUCG GAUUCGUCAC
 551 CUUCAAGGAU GAGAAAGCCA UGAAGGAUGC GAUUGAGGGA AUGAACGGAC
 601 AAGAUCUCGA UGGCCGUAGC AUCACUGUUA ACGAGGCUCA GUCACGAGGA
 651 AGCGGUGGCG GCGGAGGCCA CCGUGGAGGU GGUGGCGGUG GAUACCGCAG
 701 CGGCGGUGGU GGAGGUUACU CCGGUGGAGG UGGUAGCUAC GGAGGUGGCG
 751 GCGGUAGACG CGAGGGUGGA GGAGGAUACA GCGGCGGCGG CGGCGGUUAC
 801 UCCUCAAGAG GUGGUGGUGG CGGAAGCUAC GGUGGUGGAA GACGUGAGGG
 851 AGGAGGAGGA UACGGUGGUG GUGAAGGAGG AGGUUACGGA GGAAGCGGUG
 901 GUGGUGGAGG AUGGUAAUUC CUUUAAUUAG GUUUGGGAUU ACCAAUGAAU
 951 GUUCUCUCUC UCGCUUGUUA UGCUUCUACU UGGUUUUGUG UGUUCUCUAU
1001 UUUGUUCUGG UUCUGCUUUA GAUUUGAUGU AACAGUUCGU GAUUAGGUAU
1051 UUUGGUAUCU GGAAACGUAA UGUUAAGUCA CUUGUCAUUC UCUAAAUAAC
1101 AAAUUUCUUC GGAGAUAUUA UCUCUGUUGA UUGAUUCUAU CAUCU
```

Sequence 2: *At*GRP7 amino acid sequence.
Glycine stretch in gray, region used for structure prediction (cf. figure 2.16) in yellow with RNPs in red.

```
   1 MASGDVEYRC FVGGLAWATD DRALETAFAQ YGDVIDSKII NDRETGRSRG
  51 FGFVTFKDEK AMKDAIEGMN GQDLDGRSIT VNEAQSRGSG GGGGHRGGGG
 101 GGYRSGGGGG YSGGGGSYGG GGGRREGGGG YSGGGGGYSS RGGGGGSYGG
 151 GRREGGGGYG GGEGGGYGGS GGGGGW
```

3 Materials and Methods

3.1 Instrumentation

All instrumentation used in this work will be described in this chapter. This includes the different custom built spectroscopic setups used for confocal and widefield microscopy, as wells as standard commercial systems utilized.

3.1.1 Ensemble Spectroscopy Devices

3.1.1.1 Fluorescence Spectroscopy

A Cary Eclipse (Varian, Darmstadt, Germany) spectrometer was used for recording fluorescence spectra. The spectrometer is equipped with a thermoelectric peltier temperature control, allowing for thermal kinetic measurements.

Fluorescence spectra of recombinant Dronpa-s in solution

Purified Dronpa-s protein was diluted with PBS to 10^{-5} M in a standard quartz cuvette. The emission spectra of Dronpa were measured with the described fluorescence spectrometer at 488 nm excitation wavelength.

3.1.1.2 Absorption Spectroscopy

If light of the intensity I_0 and the wavelength λ passes through a substance, it will be attenuated to the intensity I due to absorption. The attenuation depends on the concentration C of the substance, the *specific absorption coefficient* ε at the wavelength λ and d the length of the trajectory through the substance. If the concentration is below 10^{-6} M, effects like fluorescence emission reabsorption and intermolecular interactions can be neglected. Thus the absorption A linearly relates to the concentration In this case, the absorption of light is given by the Lambert-Beer law.

$$A = \log\frac{I_0}{I} = \varepsilon \cdot C \cdot d \; . \tag{3.1}$$

Absorption spectra were obtained with a Lambda 25 absorption spectrometer (PerkinElmer). The samples were diluted to a concentration of 10^{-7} M in quartz glass cuvettes (Hellma), prior to examination.

3.1.2 Confocal Laser Scanning Microscopes

In this work varying confocal systems were used for live cell imaging. Each has its own set of advantages and disadvantages. While the commercial setups provide out of the box functionality for standard experiments, it can be hard to get quantitative results or perform rather uncommon methods on them. This is where a custom-built setup comes into play, as it is highly scalable.

Confocal systems can be of two types in general. The most common used technique in commercial systems is the *beam scanning* approach, where the laser beam is deflected by galvanometer driven mirrors, thus scanning the static sample. Both commercial systems used in this work are of beam scanning type.

Another approach is realized via *stage scanning*. Here the whole stage harboring the sample is moved in relation to a static laser beam, also

resulting in the scanning of the sample. Therefore, the stage has to be moved with high accuracy, which is often realized by a piezo driven stage. This technique was used for the custom-built setup, described in chapter 3.1.2.3.

3.1.2.1 Zeiss LSM 710

The LSM 710 (Carl Zeiss AG, Germany) is an inverse confocal microscope (see chapter 2.3), equipped with a Helium Neon (HeNe) Laser and an Argon Ionen (Ar^+) Laser. Thus, it provides several excitation laser lines: Ar^+ 458 nm , 488 nm, and 514 nm. *HeNe* 543 nm and 633 nm. Input laser powers of the Ar^+ lines could only be adjusted arbitrarily by setting a remote control knob. Input laser power of the HeNe could not be adjusted. Furthermore, the software provides a final laser power adjustment in relative units (0 – 100 %). Whereas 100 % corresponds to the input laser power. Due to the security mechanisms it is not possible to directly measure applied laser powers with an external device, as all laser emission was shut off when the optical path was interrupted by any means.

Input laser powers for each line were measured during the initial installation of the setup to be 1.42 mW for 458 nm, 7.18 mW for 488 nm, 5.76 mW for 514 nm, 0.56 mW for 543 nm and 1.71 mW for 633 nm. The Ar^+ remote control knob was adjusted to the same maximum level at its best. Therefore, laser power was assumed to be nearly the given values at initial setup attenuated by the respective percentage set in the software.

The LSM 710 facilitates two independent galvanometric scanning mirrors by which the laser beam is guided through a PlanAPO 63x/1.40 *NA* oil immersion objective (Zeiss), focusing on the sample. The fluorescence is collected by the same objective, transmits the dichroic filter and is further directed to a pinhole with adjustable aperture size. A subsequent grid spectrally separated the light nanometer-wise and directed it to three different photomultiplier tubes (PMT) . Prior to that, the spectral range could be narrowed to appropriate detection windows by multiple filter sets. The built-in z-drive (Axio Observer)

supplied 3D-scans of the samples with a minimum step size of below 25 nm.

The bundled evaluation software `Zen` (Zeiss) that came with the LSM 710 supplied a rich interface individual settings and a broad range of tools and algorithms for automated procedures, such as time-lapse imaging and also a FRAP analysis. For various reasons a manual postponed FRAP analysis was favored over the in-built tool (see chapter 3.2.2.2 on page 47).

Resulting images were saved as `.lsm`-files with a set of all applied measurement parameters for further processing. This file format can be imported by `ImageJ` (via plugin) and `Fiji` (see chapter 3.2.2 on page 46).

3.1.2.2 Leica TCM SP2

In general the TCM SP2 (Leica) features the same backbone components as the LSM 710 except for the upright orientation of the microscope. In addition to the laser lines mentioned in chapter 3.1.2.1 for the LSM, the SP2 features a 405 nm laser line. For imaging a PlanApo ×63; 1.1 *NA* oil immersion objective (Leica) was deployed. The according laser powers could be obtained by placing the sensor of an external power-meter (Field Master, Coherent) in the focal plane of the objective.

3.1.2.3 Custom Build CLSM

A custom-built confocal laser scanning microscope was used for fluorescence imaging. The main components are schemed in figure 3.1 on the facing page. The setup consists of an inverted microscope (Axiovert 200M; Zeiss) equipped with a piezo stage (PI-509; Physik Instrumente). The piezo stage moves the sample through the focus and is controlled by an analog output card (PCI-6713; National Instruments). An argon-ion laser (Ion Laser Technology) emitting at 488 nm and a laser diode (Vioflame, Coherent) emitting at 405 nm are used for excitation. Both

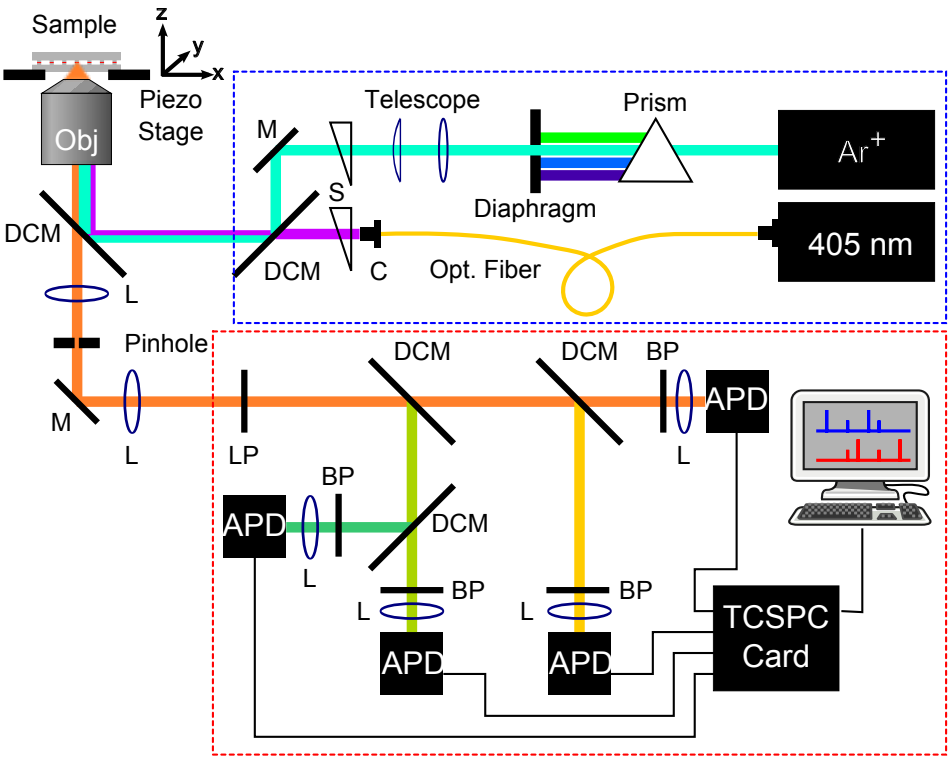

Figure 3.1: Scheme of the custom-built confocal laser scanning setup.
Optical elements used in the excitation path, indicated by the blue dashed box: Argon-Ion laser (Ar^+) and a diode laser emitting at 405 nm as laser sources. Collimator (C), mirror (M), lens (L), KEPLER-type telescope and an optical fiber, were used for beam guiding and shaping. Both excitation lasers could be attenuated and shut independently (S) and were overlaid by a dichroic mirror (DCM). Prism and a diaphragm were used to separate the 488 nm line from the residual Ar^+ laser lines.
Optical elemets within the detection path, indicated by the red dashed box: Long-pass (LP) and band-pass (BP) filters depleted raman and rayleigh scattered laser light. DCMs were used for spectral separation of the fluorescence signal. Avalanche photo diodes (APD) were used as detectors for the spectrally filtered light. For signal processing a time correlated single photon counting (TCSPC) PCI card was deployed.

laser sources are controlled by a shutter and a variable attenuator. The 488 nm laser light beam was extended using a telescope, overlaid with the 405 nm laser beam by the use of a dichroic mirror and coupled into the microscope where it was directed into the objective (Plan Apo, ×60, *NA* 1.4 oil; Olympus). The light beam was focused onto the sample and fluorescence light was collected by the same objective and spectrally separated using a dichroic beamsplitter (z 405/488; Chroma Technology). The parallel light beam was first focused onto a 100 µm pinhole and then focused onto the active area of an avalanche photodiode (AQR-16; Perkin Elmer) passing an emission filter (HQ 500 LP; Chroma Technology). The electric signal was then processed by a time-correlated single-photon counting device (SPC-630; Becker & Hickl). The whole set-up is controlled by a software based on LabView that controls the movement of the piezo scan stage and attributes photon information obtained by the photon-counting device to the appropriate x- and y -positions on the sample. If not stated otherwise, the piezo movement was adjusted to a dwell time of 1 ms/px and a step size of 500 nm/px for laser scanning experiments.

3.1.3 Fluorescence Correlation Spectroscopy Setup

FCS experiments were performed on a custom-made confocal fluorescence microscope (see figure 3.2) that essentially consists of a standard inverse fluorescence microscope equipped with a HeNe laser, emitting at 632.8 nm, as excitation source and a pinhole of 100 µm size. The collimated laser beam was coupled into an oil-immersion objective (×60; NA 1.35, Zeiss) by a dichroic beam splitter (645DLRP, Omega Optical, Brattleboro, VT). The average laser power was adjusted to be 0.5 mW before entering the aperture of the microscope, so as not to populate the triplet state of the fluorophores. The fluorescence signal was collected by the same objective, filtered by a band-pass filter (700RDF75, Omega Optical), and imaged onto the active area of two single-photon avalanche photodiodes (APDs) (SPCM-AQR-14, PerkinElmer Optoelectronics, Vaudreuil, QC, Canada), sharing the fluorescence signal by a cubic non-polarizing beamsplitter (Linos, Göttingen, Germany). The signals of the APDs were recorded at cross-correlation setting

(9 cycles a 100 s for each measurement) by using a real-time photon correlator PCI card (DPC-230, Becker & Hickl, Berlin, Germany). The application of two APDs at cross-correlation setting circumvents dead-time and after-pulsing effects.

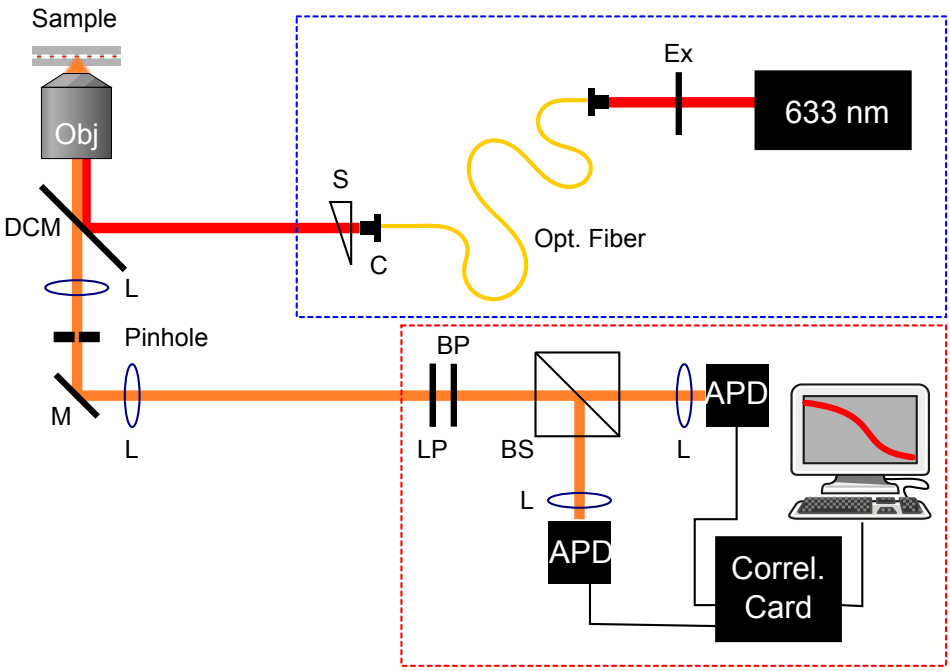

Figure 3.2: Scheme of the custom-built FCS setup.
Optical elements used in the excitation path, indicated by the blue dashed box: Diode laser equipped with excitation filter (Ex) emitting at 633 nm as laser source. Collimator (C), mirrors (M), lenses (L), and an optical fiber, were used for beam guiding and shaping. An attenuator/shutter (S) was used for adjusting the laser intensity.
Optical elemets within the detection path, indicated by the red dashed box: Long-pass (LP) and band-pass (BP) filters depleted raman and rayleigh scattered laser light. A 50/50 beam splitter cube (BS) was used for equal distribution of the fluorescence signal on to APDs. For signal processing a correlator PCI card was deployed.

3.2 Data Processing and Analysis

3.2.1 Correlation Matrix Method

This method is based on evaluating the Euclidian length Γ of a vector derived from a 4×4 Hermitian correlation-matrix that contains correlation coefficients calculated from image data. Therefore, an image is first transcribed into a linear trace of the pixel-to-pixel intensity variation. This linear plot can consist of an arbitrarily chosen path within the image, or it could just be a linear display of the confocal image scan. The intensity profile is then subdivided into N sections s (not necessarily of equal length). For each section the absolute number of signals $I_i(s)$ with $i = 1, 2 =$ `red,green` is counted where i represents the individual channels (e.g. red/green emitting fluorophores). $I_{sum}(s)$ and $I_{col}(s)$ denote the total number of signals across all channels and the number of colocalized intensities. The 4×4 correlation-matrix for colocalized data is defined as

$$\chi = \begin{pmatrix} 1 & r_{2,1} & r_{sum,1} & r_{col,1} \\ r_{1,2} & 1 & r_{sum,2} & r_{col,2} \\ r_{1,sum} & r_{2,sum} & 1 & r_{col,sum} \\ r_{1,col} & r_{2,col} & r_{sum,col} & 1 \end{pmatrix} \tag{3.2}$$

and the corresponding Euclidian length Γ of the vector can be calculated in the case of two colors with

$$\Gamma_2 = \sqrt{r_{1,2}^2 + r_{1,col}^2 + r_{2,col}^2 + r_{sum,col}^2} \tag{3.3}$$

, where every $r_{i,j}$ represents a correlation coefficient of two channels with $i, j = 1, 2, sum, col$ calculated by

$$r_{i,j} = \frac{\frac{1}{N}\sum_{s=1}^{N}(I_i(s) - \overline{I_i}) \cdot (I_j(s) - \overline{I_j})}{\sqrt{\sum_{s=1}^{N}(I_i(s) - \overline{I_i})^2} \cdot \sqrt{\sum_{s=1}^{N}(I_j(s) - \overline{I_j})^2}} \tag{3.4}$$

, taking into account the alternating contributions, respectively. The correlation matrix can readily be extended to more than two data channels by including the corresponding additional coefficients. For

practical reasons a number of $N = 20$ segments is reasonable to reduce computation time. The relative deviation of the norm is calculated to 10%. As the number of sections goes to 100 the norm reaches a limiting value and the relative error becomes insignificant. The Γ-norm decreases to a limiting value as a number of sections following a power law. For a two-channel sample that exhibits perfect colocalization the norm Γ_2 has a maximum value of 2. If the majority of signals are randomly colocalized, Γ_2 adopts values below 1, and a mixture of both delivers a value between 1 and 2. To also provide a measure for the number of non-colocalized events an additional relative norm is defined as

$$\Gamma_{rel} = \frac{\Gamma_{max} - \Gamma_N}{\Gamma_{max}} \tag{3.5}$$

, called the anti-fraction. Γ_{rel} denotes the relative number of signals which do not colocalize or in other words it represents the deviation from a perfectly colocalized sample. The introduction of this parameter is necessary, because for samples with more than two data channels Γ_2 is a mixture of all (two or more) colocalized events, whereas Γ_{rel} is always (in good approximation) the percentage of non-colocalized events. For image processing the algorithm can be further simplified by neglecting the signal identification step using arbitrary thresholds. The threshold value can be set using $T = \mu + 3\sigma$, where μ denotes the mean intensity value of the region of interest (ROI) or the entire image, and the linear term $\delta \cdot \sigma$ represents multiples of the corresponding standard deviation σ. The extension of this method to the evaluation of three-color colocalization data is straightforward. In this case Γ has to be modified to

$$\Gamma_3 = \sqrt{r_{1,2}^2 + r_{1,col}^2 + r_{2,col}^2 + r_{sum,col}^2 + r_{3,col}^2 + r_{3,1}^2 + r_{3,2}^2} \tag{3.6}$$

,which can have a maximum value of $\sqrt{7} \approx 2.65$. In this case, norms with values below

$$\left.\frac{\Gamma_{n-max}}{n}\right|_{n=3} \approx 0.88 \tag{3.7}$$

,(where n is the total number of channels analyzed) indicate a sample with a major anti-fraction, i.e. few to no colocalized events. Fur-

ther extension to more than 3 color channels is also straight forward.

3.2.2 Image Processing with ImageJ (Fiji)

Post-processing of image data of all kinds was done with `Fiji`, which is a platform independent, scientific grade java application. `Fiji` is an image processor based on the freely available and widely used `ImageJ` which is known to be especially expandable by a multitude of plugins. Therefore, the approach of `Fiji` is, to deliver a fully usable image processor out of the box, by including the most important plugins in a single software package. Also frequent updates to the `ImageJ`-core as well as to the plugins are supplied. All this made Fiji the first choice for image post-processing in this work.

Furthermore, a novel plugin to work with both, `ImageJ` and `Fiji`, emanated from this work and was made accessible to further scientific usage.

3.2.2.1 GICA-Plugin

The developed plugin was written in the scripting language `Jython`, which is an implementation of the `Python` programming language written in Java. Thus it could be directly packaged as an `ImageJ/Fiji` plugin.

Therefore, `Fiji` provides an own *integrated development environment* (IDE) for plugin and macro programming.

However, the core algorithms were written in `C++`, partly originating from the routines developed by Yahiatène et al. [2012]. These routines were adapted and complemented by newly developed algorithms, to match the needs emerging due to the novel implementation in image data analysis (see chapter 3.2.1).

3.2.2.2 FRAP-Analysis of Time Lapse Image Series

Time lapse image series acquired with one of the deployed confocal setups, were saved as a `tif`-stack whenever possible, or converted thus. In this form they could be easily imported in `ImageJ/Fiji`. Files saved in `.lsm` format are nothing but `tif`-stacks including all parameters set during measurement in a specific file header. Therefore `Fiji` can import those right out of the box, whereas a plugin is necessary for `ImageJ`.

However, once imported, the image data was processed as follows: Three *regions of interest* (ROI) were defined by using the selection tool and the `Roi Manager` of `Fiji/ImageJ`. One ROI including plain background signal, a second ROI encircling a fluorescent reference cell and the last ROI defining the target cell, compartment or area in general. Thus this had to be satisfied by establishing an appropriate composition of the image prior to acquisition.

Occasionally an additional registration of the image stack was necessary, when the specimen moved a reasonable distance during image acquisition. This was realized by application of the `StackReg` plugin.

Furthermore, the `Multi Measure` function of the `ROI Manager` was used, while the measurement options were set to calculate the mean gray value of each ROI and its standard deviation. This results in a list of comma separated values and therefore was saved as a `csv`-file. Thus obtained data was further analyzed and plotted with the statistic software suite `Origin8 Pro` (OriginLab, USA).

3.2.3 Fluorescence recovery after selective photoswitching

For fluorescence recovery after selective photoswitching experiments, the selected area of the sample was moved to the laser focus by means of the piezo stage. A preswitch image was acquired with the setup described above. Then the laser power was increased to

10 µW for 10 seconds through a variable attenuator in order to switch Dronpa-s to the off-state. The switched region corresponds to the dimensions of the laser focus. The cell was scanned directly after the end of the switching process. Subsequently, images were acquired at 2 min intervals. The mean gray values in the nucleus were calculated for each image and plotted versus the time. A mono-exponential function

$$f(t) = A \cdot (1 - exp{-k \cdot t}) \,, \tag{3.8}$$

where t is the time, A the apparent saturation and k the recovery constant, was fitted to the data points to extract the Characteristic recovery time ($\tau_{\frac{1}{2}}$) value. The images were stored at 16 bit resolution and analyzed using ImageJ (U.S. National Institutes of Health; `http://www.rsbweb.nih.gov/ij/`). A Student's t-test was used to evaluate the differences in recovery half-times at zt4 and zt11, respectively. A p value < 0.05 was considered significant.

3.2.4 Hairpin Computation

DNA hairpin structures were calculated and visualized by `UNAFold` (version 3.8) Peyret [2000], SantaLucia [1998], Zuker [2003]. The settings were adjusted to linear DNA sequences in a mM concentration. Folding temperatures were set to room temperature and ionic conditions were adapted to the used PBS buffer and set to 140 mM.

3.3 Sample Preparation

3.3.1 Recombinant Dronpa-s fusion protein

Dronpa-s was created by adaptation of the codon usage to the bias of *Arabidopsis* using codon adaptation index (CAI) performed by GeneArt

using their in-house proprietary software Geneoptimizer®. Furthermore, cryptic splice signals, TATA boxes, ribosomal entry sites, repeat sequences and extensive RNA secondary structure were avoided and a Kozak sequence surrounds the start codon.

Dronpa-s was fused in frame to glutathione S-transferase in the vector pGEX-6P1 (GE Healthcare). Recombinant GST-Dronpa-s was expressed in E. coli BL21 (DE5) cells and purified from crude lysate by batch absorption on GST agarose. The Dronpa-s moiety was recovered by cleavage of the fusion protein with PreScission protease (GE Healthcare) on the column according to the manufacturer's recommendation.

3.3.2 Immobilization of recombinant Dronpa

Mowiol polyvinyl alcohol (PVA) (Calbiochem) was heated to 37° C and mixed with a solution (0.5 mg/ml in PBS) of recombinantly expressed Dronpa-s. Microscopy coverslips were immediately coated using a self-assembled spin coater resulting in a film only a few micrometers thick. Measurements were performed on the setup described previously.

3.3.3 Construction of the *At*GRP7-Dronpa-s fusion

To allow in-frame fusion of Dronpa-s to the C-terminus of the *At*GRP7 coding sequence (including the intron), the *At*GRP7 stop codon was replaced by a *Bam*HI site. The *At*GRP7-Dronpa-s fusion protein was expressed under control of 1.4 kb of the *AtGRP7* promoter, the *AtGRP7* 5' UTR and 3' UTR (construct *AtGRP7*:*At*GRP7-Dronpa-s). As a control, Dronpa-s was placed under control of the same regulatory elements [Staiger and Apel, 1999]. The cassettes were inserted into *Hind* III-*Xba*I-cut pUC19 polylinker of the binary vector pHPT1 [Schöning et al., 2008].

3.3.4 Plant transformation and growth

Agrobacterium-mediated stable transformation of *Arabidopsis* Col was performed using vacuum infiltration [Bechtold and Pelletier, 1998]. Seeds were germinated on onehalf strength MS plates containing 0.5 % sucrose supplemented with the appropriate antibiotic and grown in 16 h light / 8 h dark cycles at 20° C in a Percival growth chamber.

3.3.5 Transient expression in *Nicotiana benthamiana*

Both, Dronpa-s and Dronpa from the commercial vector (Dronpa-GREEN pDG-S1; MLB Group Company), were placed under control of the CaMV promoter in the vector pRT104 [Töpfer et al., 1987]. The cassettes were inserted into the binary vector pCAMBIA 3000 and the constructs were introduced into *Agrobacterium tumefaciens* GV3101 (pMP90) . *Agrobacterium* cultures were independently centrifuged at 8000 g for 15 min, washed once with and resuspended in infiltration media (10 mM MES–KOH pH 5.7, 10 mM MgCl2, 100 µM acetosyringone) and adjusted to an optical density (OD)600 of 0.8. Cultures expressing Dronpa-s or Dronpa-GREEN were mixed with an equal volume of agrobacteria expressing the viral silencing suppressor p19. Multiple individual leaves (4–5 leaf stage, ca. 10 cm high) were mechanically infused by pressing the tip of the syringe against the lower surface of the leaf and applying gentle pressure to the plunger. Four days after infiltration, leaves were harvested and quick-frozen in liquid N_2. For determination of the Dronpa fluorescence, native protein extracts were prepared and diluted to a concentration of 5 µg/mL with PBS. After excitation at 480 nm, the fluorescence emission spectrum was recorded (500–600 nm). Peak fluorescence intensity at 516 nm was expressed as means ± SD (n = 10). Student's t -test was used to determine whether the differences were statistically significant.

3.3.6 Transfection of HeLa and COS-7 cells

Both, Dronpa-s and Dronpa-GREEN (pDGS1; MLB Group Company), respectively, were inserted into the vector pcDNA3.1+ under control of the CMV promoter. Transfection of confluent HeLa or COS-7 cells was performed with TurboFect (Fermentas) according to the manufacturer's instructions. Twenty-four hours after transfection, proteins were extracted using the mammalian protein extraction reagent (M-PER)mammalian protein extraction reagent (Thermo Scientific) according to the manufacturer's instructions. Dronpa fluorescence was determined as described for tobacco leaves.

3.3.7 Titration assays for FCS measurements

Synthetic DNA and RNA oligonucleotides functionalized with Atto655 at the 3´ end (absorption maximum 663 nm, fluorescence emission maximum 684 nm) were obtained from IBA (Göttingen, Germany). Fluorescently labeled oligonucleotides were diluted to a final concentration of 0.1 nM in phosphate-buffered saline (PBS, pH 7.4) containing 0.05% Tween 20 to suppress glass surface interactions.

For measurements with RNA oligonucleotides, ribonuclease inhibitor RiboLock (400 units/ml) (Fermentas; St. Leon-Rot, Germany) and tRNA (10 µg/ml) were added to the buffer. FCS measurements were carried out in 70 µl solution enclosed by a recessed slide and a cover slip, using 63 µl of oligonucleotide solution 10^{-10} M and 7 µl of recombinant protein, as indicated. All measurements were performed at room temperature.

4 Results and Discussion

In order to give a comprehensive view on the findings made during this work, I will start with the fluorescent reporter Dronpa-s, a variant of the reversibly photoswitchable Dronpa, which was found by Ando et al. [2004] previously.

Dronpa-s (synthetic Dronpa) was engineered to optimize the codon usage for expression in *Arabidopsis* by Lummer et al. [2011]. To characterize the photochemical properties of the synthetic protein in detail, recombinantly expressed Dronpa-s from *Escherichia coli* was purified and further examined for its fluorescence spectroscopic abilities. The corresponding results are shown in chapter 4.1.

In a further step transgenic *Arabidopsis* plants were cultivated. Those plants are genetically altered. Therefore, they intrinsically produce Dronpa-s which is fused to a specific protein of interest: *At*GRP7. The purpose of the fusion protein is to permanently combine the fluorescent properties of Dronpa-s with the physiological functionality of the target protein *At*GRP7.

To test whether *At*GRP7 remains functional in the fusion protein, a knockout mutant was engineered, in which endogenous *At*GRP7 is not expressed. In this mutant, an elevated level of *At*GRP8 was detected, which is a closely related protein that is under negative control by *At*GRP7. Thus, the loss of *At*GRP7 expression leads to a relief in repression for *At*GRP8 [Streitner et al., 2008]. Furthermore, the mutant develops more leaves than wild-type (wt) plants prior flowering. An insertion of *At*GRP7-Dronpa-s into this mutant, leads to a compensation for the lack of endogenous *At*GRP7, thus, *At*GRP8 protein returns to wt levels.

After proving the functionality of *At*GRP7 within the fusion protein is preserved, the target protein can be examined by means of fluorescence spectroscopic methods. Endorsing this, sub-cellular localization studies and findings on the complex transport mechanisms of *At*GRP7 are featured in chapter 4.2 and chapter 4.3 respectively.

As suggested previously [Heintzen et al., 1997, Schöning and Staiger, 2005, 2009, Schöning et al., 2007, 2008, Schüttpelz et al., 2008, Staiger, 2001, 2002, Staiger and Apel, 1999, Staiger and Heintzen, 1999, Staiger et al., 1999, 2003, Streitner et al., 2008] *At*GRP7's ability to bind nucleic acids, is assumed a key role in its molecular function. This binding is examined further via binding studies based on FCS measurements. The according results are discussed in chapter 4.4.

Recent findings also indicate *At*GRP7 to play a role in the stress response pathway of *Arabidopsis*. Therefore, colocalization studies were performed on a confocal setup, in order to visualize molecular participation of *At*GRP7 in the building of processing bodies (see chapter 4.5). Emerging from this approach, a completely novel and enhanced colocalization algorithm was developed, which is reviewed in depth in chapter 4.6.

4.1 Spectroscopic Properties of Dronpa-s

The synthetic protein exhibits an absorption spectrum with the maximum at 503 nm (see figure 4.1). The emission spectrum, recorded during excitation at the wavelength of 488 nm, peaks at 518 nm. Thus, the codon-optimized variant resembles the original Dronpa protein cloned from *Pectiniidae* as reported by Ando et al. [2004].

Subsequently, the minimum region of a sample that could be photoswitched with the confocal setup (see chapter 3.1.2.3) was determined, using immobilized Dronpa-s protein. Therefore, an approximately 10 µm thin layer of Dronpa-s, embedded in PVA, was spin-coated on a glass cover slide. For three seconds 488 nm laser light was

focused onto a single spot in the sample with a focal laser power of 10 µW to transfer Dronpa-s to the off-state. Then, an area of 8 µm × 8 µm was scanned with attenuated focused laser light (0.3 µW) of the same wavelength (figure 4.2 a). Thus, an intensity profile of the bleached region could be acquired by laser scanning fluorescence microscopy.

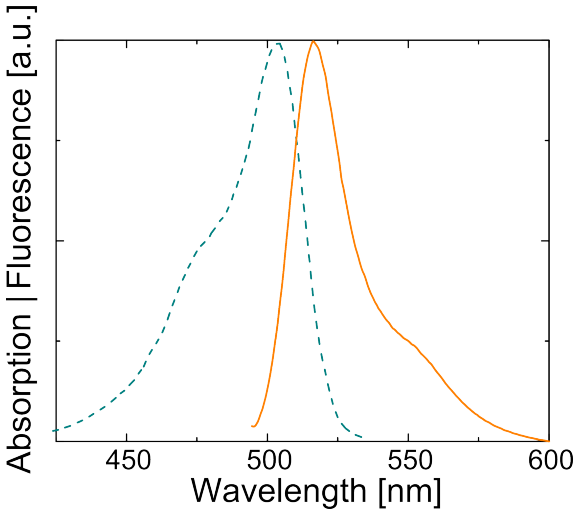

Figure 4.1: Absorption and emission spectra of Dronpa-s.
The dashed line represents the absorption and the solid line the emission of Dronpa-s. Both, absorption and emission of Dronpa-s, peaking at 503 nm and 518 nm respectively, comply with the characteristics of original Dronpa [Ando et al., 2004].

A line plot through the center of the bleached spot yields a Gaussian intensity distribution, where $2{\cdot}\sqrt{2 \cdot \ln 2}{\cdot}\sigma = \mathrm{FWHM}$, with σ resembling the standard deviation and the Full width at half maximum (FWHM) being the extent of the normal distribution function. Here the FWHM parameter is used to characterize the size of the bleached spot. An effective diameter of 1.15 µm in lateral direction for a minimum bleached region could be achieved using a confocal setup (figure 4.2 b), at a given exposure time of 3 s and focal laser power of 10 µW. This implies that in biological samples also a minimum region of approximately

1 µm diameter can be selectively transferred to the off-state upon laser irradiation.

The limitation of the affected area is mandatory to not only switch off fluorescence in specific cells inside a compound, but even more, selectively switching specific sub-compartments of a cell. Such can be done with nuclei in mammalian or plant cells, that are surrounded by cytoplasm and other cell compartments.

Analogue to the previous, another experiment was performed after switching the majority of Dronpa-s molecules to the off-state, by repeatedly scanning an area of 20 µm × 20 µm with a significantly higher laser power (20 µW focal power). Consecutive to that, laser light of 405 nm and a focal laser power of 0.1 µW, was focused into the sample for 3 seconds causing the Dronpa-s molecules in a small spot regaining their fluorescence. The result of the subsequent scanning is shown in figure 4.2 c and d. Compared to the previously described off-switching, a wider area is affected by the on-switching, with a FWHM of 2.7 µm. This complies with the observation in figure 4.3 indicating the on-switching process to be more efficient, as already described for original Dronpa by Ando et al. [2004].

A further interesting finding was achieved, when samples expressing *At*GRP7-Dronpa-s were examined using the commercially available LSM 710 (Zeiss) (cf. chapter 3.1.2.1). This setup lacked an UV-laser as excitation source and the operator had to adjust to laser lines from an Ar^+ (458 nm , 488 nm, 514 nm) and a *HeNe* laser (543 nm, 633 nm). Thus, switching Dronpa-s to the on-state, with the shortest available wavelength available, was tested. On-switching by 458 nm turned out to be rather efficient, which is showcased in figure 4.3. Here, Cos-7 cells, transiently expressing Dronpa-s, were imaged via excitation with the 488 nm laser line (figure 4.3 a). The applied focal excitation power sufficed to switch a noticeable amount of Dronpa-s molecules to the off-state during acquisition of the image sequence. This yields the decay in fluorescence intensity shown in figure 4.3 c.

Consecutive imaging using the 458 nm laser line not only shows the gradual increase of fluorescence in each image, but furthermore exhibits the ability of 458 nm light to excite both, on- and off-state of Dronpa,

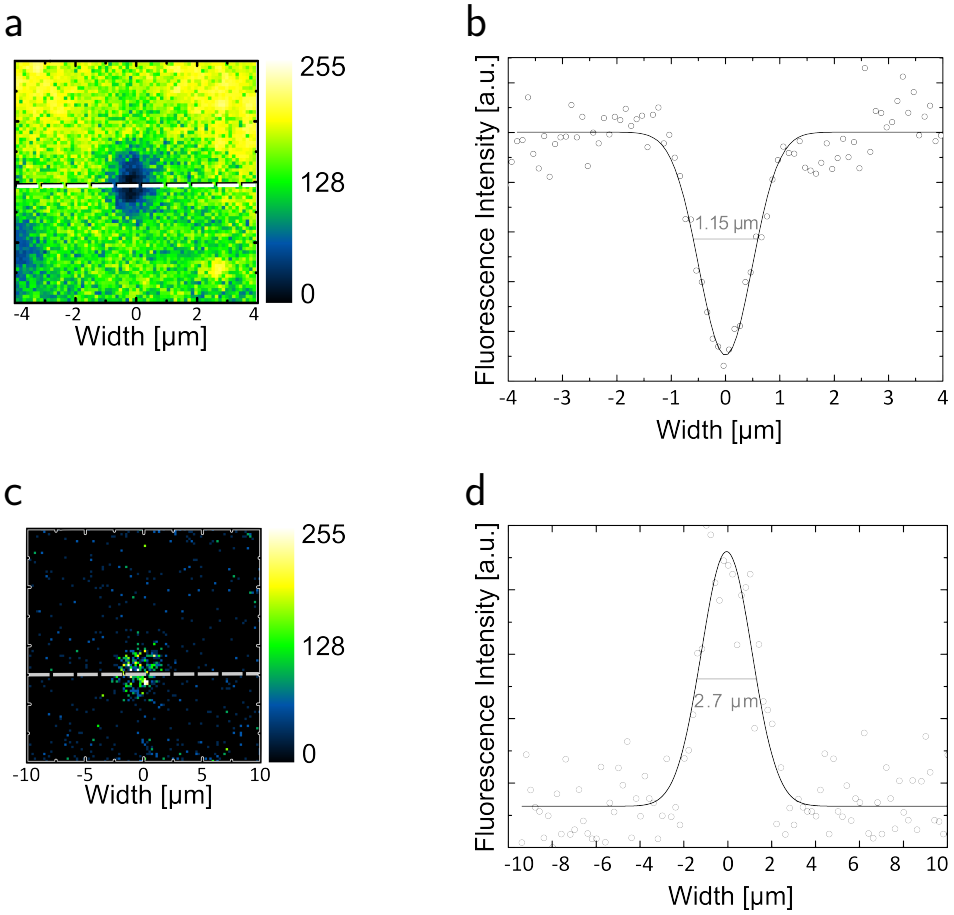

Figure 4.2: Photoswitching of immobilized Dronpa-s.
Recombinant Dronpa-s was immobilized in Mowiol (see. chapter 3.3.2) and spin-coated on a glass surface. With the confocal setup described in chapter 3.1.2.3, a small spot was switched off (a) and on (c) by focused 488 nm and 405 nm laser light respectively. The exposure time and laser power were adjusted to the same levels as used for FRAP experiments, thus the lateral dimension of the minimum affected region could be determined according to the FWHM convention.

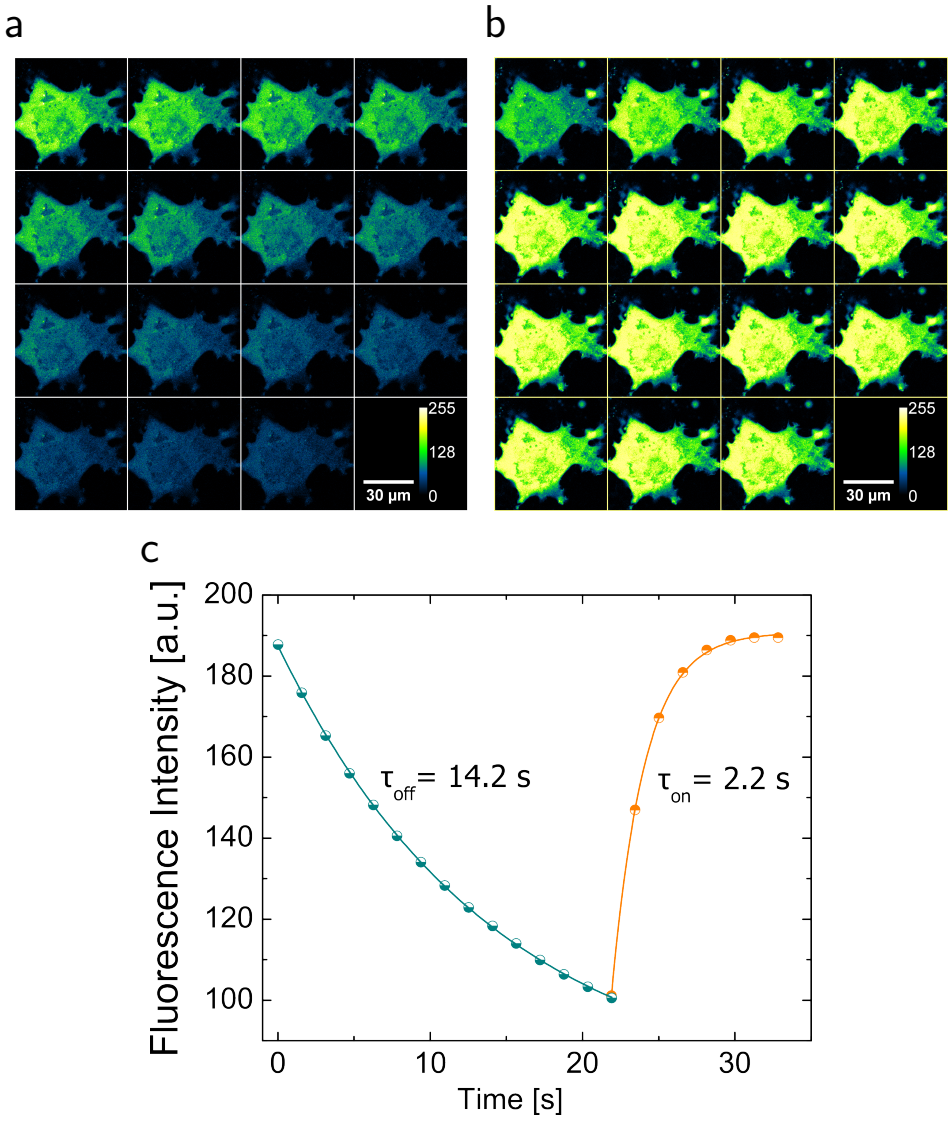

Figure 4.3: Photoswitching Dronpa-s in Cos-7 cells. Transiently transfected Cos-7 cells, expressing Dronpa-s, were imaged on a standard confocal setup (see chapter 3.1.2.1). Imaging with 488 nm light (~1.9 µW; 1 %) switches Dronpa-s off. Subsequent irradiation with 458 nm light (~0.6 µW; 30 %) switches Dronpa-s back to the on state efficiently.

efficiently (figure 4.3 b). Even with 458 nm light, on-switching is more efficient than the off-switching by 488 nm light. This effect can be explained by analyzing the absorption spectra of Dronpa-s in the on- and the off-state respectively. The wavelength of 458 nm is close to the isosbestic point of the two absorption spectra, thus both states are excited with comparable efficiency. Both processes follow a mono-exponential trend (figure 4.3 c), where $\tau_{on/off}$ denotes the characteristic time of the respective progression.

4.2 Subcellular Localization of *At*GRP7

Having access to the functional fusion protein *in vivo*, the localization of *At*GRP7-Dronpa-s within *Arabidopsis* cells was of high interest. Therefore, the custom confocal setup was used to record fluorescence images of *Arabidopsis* roots and/or leafs, which were cut off of the plant and immediately conditioned with approximately 100 µl H_2O between two glass coverslips. Under these circumstances the cells are considered alive for at least half an hour. These samples were further examined at the confocal setup.

The obtained fluorescence images resemble optical cross-section of the sample. Due to the confocal principle, fluorescence from higher and lower planes of the sample is filtered by the pinhole efficiently.

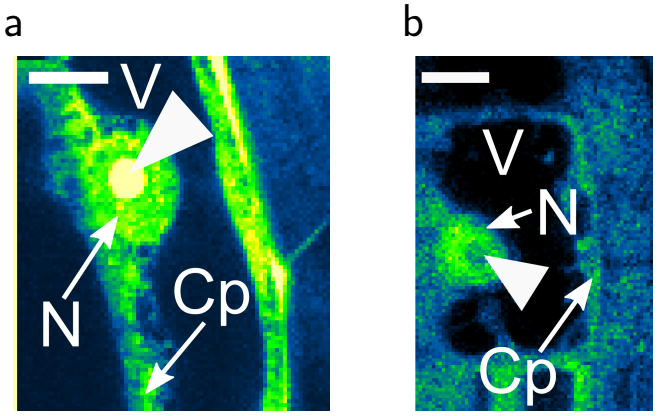

Figure 4.4: Localization of *At*GRP7-Dronpa-s and Dronpa-s in transgenic *Arabidopsis* plants.
Root cells of transgenic *At*GRP7-Dronpa-s plants imaged with the custom confocal setup (see chapter 3.1.2.3). The scale bar corresponds to 10 µm. The arrowheads denote the nucleolus. Arrows point at nucleus (N) and cytoplasm (Cp), V is the vacuole. (a) Intracellular distribution of *At*GRP7-Dronpa-s with a high abundance in the nucleolus. (b) Intracellular distribution of *At*GRP7-Dronpa-s showing low abundance in the nucleolus.

Plant cells are subject to their intrinsic cell pressure termed turgor pressure, which pushes the tonoplast against the cell wall. The tonoplast separates the vacuole from the cytoplasm and all other cell compartments. Thus a healthy *Arabidopsis* cell will look like pictured in figure 4.4, exhibiting the cytoplasm pressed against the cell wall by the vacuole, forming a thin rim. Bigger cell compartments situated within the cytoplasm are visible as buckles against the vacuole. The most prominent compartment is the cell nucleus, which remains its spherical shape despite the turgor, thus standing out of the cytoplasm (figure 4.5). For even better discrimination of the nucleus against the rest of the cell, the Endoplasmic reticulum (ER) was additionally marked by a fluorescent reporter. Here the red fluorescent protein mCherry was used. The rough ER accumulates around the nucleus highlighting it efficiently (figure 4.5).

Due to the fusion of *At*GRP7 to Dronpa-s the localization within a cell could be easily displayed. It is dispensed in the cytoplasm homogeneously and in high abundance. *At*GRP7 also locates to the nucleus in an even higher concentration compared to the cytoplasm. The cross-section in which the nucleus has its maximum expanse, reveals another feature of the cell. A spot within the nucleus exhibits a particularly high *At*GRP7 abundance. This suggests that *At*GRP7 strongly concentrates at nucleolus site (figure 4.5), which is a small cell structure inside the nucleoplasm.

The turgidity avoids a clear distinction of cell wall and cytoplasm. Thus it was uncertain if *At*GRP7 is also situated at or in the cell wall. Therefore, the osmotic flow, which keeps up the turgidity of the cells, was interrupted by applying hypotonic medium to the sample. As a consequence the protoplast, including cytoplasmic membrane, cytoplasm, vacuole and other cell compartments, peeled away from the cell wall, leaving a gap in between. This process is termed plasmolysis. Fluorescence images from both conditions, before and after plasmolysis, are displayed in figure 4.6. The fluorescence image gives clear evidence that *At*GRP7 is not located in the cell walls of *Arabidopsis*, since only the protoplasts feature fluorescence.

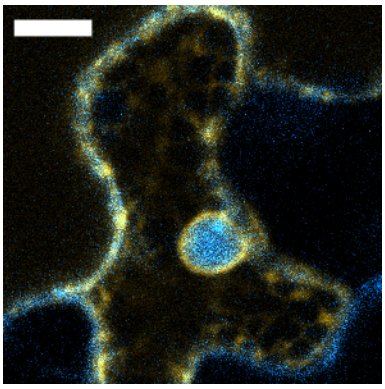

Figure 4.5: Localization of *At*GRP7-Dronpa-s in *Arabidopsis* epidermal leaf cell.
Epidermal leaf cell of *Arabidopsis* expressing both, *At*GRP7-Dronpa-s (blue) and an ER marker attached to mCherry (yellow). *At*GRP7-Dronpa-s is to be found in the cytoplasm and prominently locates to the nucleoplasm, which is pronounced by the rough ER enclosing the nucleus. Scale bar corresponds to 20 µm. Image was acquired with the custom confocal setup (see chapter 3.1.2.3)

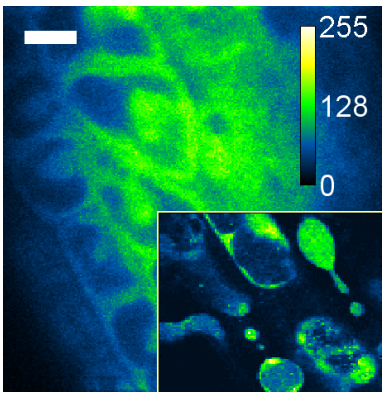

Figure 4.6: Plasmolysis of *Arabidopsis* root cells expressing *At*GRP7-Dronpa-s.
The image shows a fluorescence image of a compound of *Arabidopsis* root cells before and after (inset) exposure to hypertonic medium. The scale bar corresponds to 10 µm. The images were acquired by using the custom confocal setup (see chapter 3.1.2.3).

4.3 Nucleo-Cytoplasmic Shuttling of *At*GRP7

With the perspective on how *At*GRP7 is distributed throughout the cells in *Arabidopsis*, the question how the *At*GRP7 molecules reach the inside of the nucleus, arose. The nucleus is separated from the cytoplasm by the nuclear envelope.

Proteins and other molecules can pass this barrier by shuttling through the so called nuclear pore complexes (NPC). NPCs contain a central aqueous channel with an estimated radius of about 2.6 nm [Mohr et al., 2009]. Proteins with a molecular mass above approximately 40 kDa require a nuclear localization signal (NLS) to pass the NPCs, while smaller proteins can passively diffuse through the channel [Freitas and Cunha, 2009, Görlich and Kutay, 1999].

Regular nuclear localization signals consist of one or two stretches of basic amino acid residues, in particular lysines. *At*GRP7 does not feature a classical NLS, but it has an M9 domain originally found in some mammalian heterogeneous nuclear ribonucleoproteins (hnRNPs) implicated in many aspects of RNA processing [Siomi and Dreyfuss, 1995]. M9 domains have been suggested to mediate transport both into and out of the nucleus by Bogerd et al. [1999]. *At*GRP7, with a size of 17 kDa, is below the size-exclusion limit of the NPC, anyway. Therefore, it can reach the nucleoplasm by diffusion. However, the strong abundance of *At*GRP7-Dronpa-s (which –with 45 kDa– is obviously bigger than Dronpa-s) in the nucleus, can hardly be explained solely by diffusion.

4.3.1 Imaging Techniques adopted to reversibly switchable Dronpa-s

Diffusion and transport mechanisms can be visualized by special imaging techniques, involving photobleaching and photoactivation of fluorophores. The first method to quantify molecular movement through photobleaching recovery kinetics was described by Axelrod

et al. in 1976. This method became a widely used imaging technique and was termed FRAP[1]. Even measurements of protein dynamics between compartments within the cell became possible by selectively bleaching the fluorescence of specific cell compartments [Goodwin and Kenworthy, 2005, Köster et al., 2005, Lippincott-Schwartz et al., 2001].

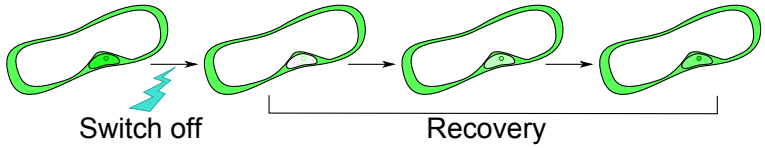

Figure 4.7: FRAP scheme revealing *At*GRP7 to be imported from cytoplasm to nucleus in a plant cell. First fluorescence within the nucleus is selectively switched off, leaving the rest of the cell unaffected. In the following the fluorescence recovery is monitored, possibly providing information on the underlying transport mechanism.

This method looked promising in the quest for the mechanism behind the nuclear transport of *At*GRP7. An aim was to realize an experiment as schemed in figure 4.7 where the fluorescence of Dronpa-s is selectively switched off within the nucleus, and the recovery is monitored subsequently. The determination of the kinetics of fluorescence recovery, should yield information about the process which gives rise to nuclear import of *At*GRP7.

Due to the ability to reversibly switch Dronpa-s, a further experiment is imaginable. As displayed in figure 4.8, even a possible export of *At*GRP7 can be visualized and characterized by an inverse experiment design, where the fluorescence, specifically within the nucleus, is switched back on, consecutive to switching off all fluorescence throughout the entire cell.

[1] [Ali and Reddy, 2006, Braeckmans et al., 2003, 2007, Braga et al., 2004, Bulinski et al., 2001, Carrero et al., 2003, Ellenberg et al., 1997, Glazachev and Khramtsov, 2006, Hagen et al., 2009, Hallen and Layton, 2010, Herrmann et al., 2005, Kruhlak et al., 2000, Lippincott-Schwartz et al., 2003, Lubelski and Klafter, 2008, Mazza et al., 2007, 2008, Mueller et al., 2008, Reits and Neefjes, 2001, Sprague and McNally, 2005]

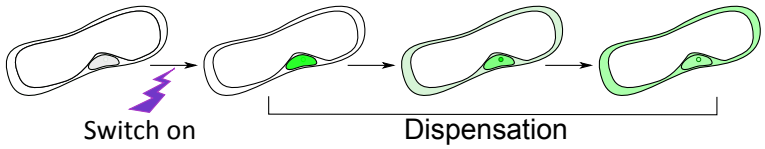

Figure 4.8: Photoactivation scheme revealing *At*GRP7 to be exported from nucleus to cytoplasm in a plant cell.
First all fluorescent molecules in the cell are switched off. Next, the fluorescence within the nucleus is selectively switched on, leaving the rest of the cell unaffected. In the following the decay of fluorescence is monitored, possibly providing information on the underlying transport mechanism.

The general aptitude of Dronpa-s for such imaging techniques was tested with Cos-7 cells, which were transiently expressing *At*GRP7-Dronpa-s. These mammalian cells were preferred over the stable transfected plant cells, at test stage, because of their size and shape, both of which afford a more convenient experiment design. Another aspect was time, since Cos-7 cells grow a lot faster than *Arabidopsis* seedlings.

Similar to its distribution in *Arabidopsis* cells, *At*GRP7 locates to both nucleus and cytoplasm of Cos-7 cells, where it holds no native functionality. As shown in figure 4.9, Dronpa-s fluorescence can be selectively switched off in the nucleus of the cell, while the rest of the cell remains fluorescent. The following images of the sequence display the gradual recovery of fluorescence within the nucleus on a time scale of several minutes. Thus, fluorescent molecules from outside the nucleus have moved to the inside by passing the nuclear envelope. The $\tau_{\frac{1}{2}}$ parameter can be extracted from the respective fluorescence intensity plot, by a logistic fit (figure 4.10). $\tau_{\frac{1}{2}}$ resembles the time of half recovery which is characteristic to the mechanism accounting for the recovery.

A following second experiment could be performed on the very same cell which was probed before. This time the fluorescence in the whole cell

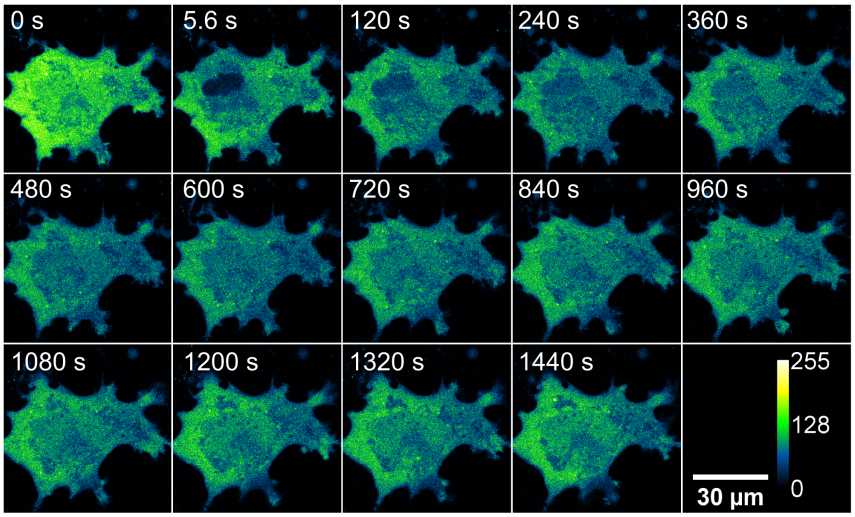

Figure 4.9: Dronpa-s within the nucleus of Cos-7 cells selectively switched to off-state.
Transiently transfected Cos-7 cells expressing Dronpa-s were imaged on a standard confocal setup (see chapter 3.1.2.1). The 'FRAP' program of the LSM software (Zen, Zeiss) was used to specify a small region of interest within the nucleus. Next the ROI was irradiated by intense 488 nm light and a subsequent time lapse image sequence was recorded (1%, 488 nm).

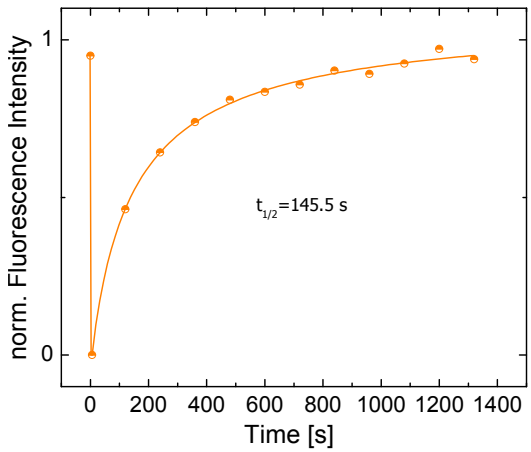

Figure 4.10: Intensity recovery plot of fluorescence within Cos-7 nucleus.
The fluorescence intensity recovery was fitted by a logistic model.

is switched off. In a next step, the molecules within the nucleoplasm were selectively switched to the on-state, as shown in figure 4.11. As a result the nucleus fluoresces bright, while the rest of the cell remains dark. Over time (again several minutes) the fluorescence got dispersed to the whole cell, emanating from the nucleus. Due to this dispersion the fluorescence intensity decreased within the nucleus, which is displayed by the intensity plot in figure 4.12. A respective $\tau_{\frac{1}{2}}$ value can be extracted, by fitting a logistic model to the data (figure 4.10).

In summary the applied testing stage, featuring Cos-7 cells and the standard confocal LSM 710 microscope, demonstrated the aptitude of Dronpa-s to serve as a fluorescent reporter for experiments comprising selective photoswitching. Another interesting finding arose from these experiments. Unexpectedly Dronpa-s also turned out to be better adapted to expression in Cos-7 cells compared to original Dronpa [Lummer et al., 2011].

4.3.2 Selective photoswitching in plant cells

Exchanging the test system against the functional system in plants bore some difficulties which had to be overcome. As mentioned before, the *Arabidopsis* seedlings need some time to grow to reasonable size. Plants had to grow for a time period of at least two weeks prior to examination. Furthermore, the size and shape of the plant cells compared to the previously used Cos-7 cells was very different.

It was a challenge to take aim at the nucleus with the laser, while it was pushed against the cell wall, being a significantly smaller target. Therefore, it was convenient to switch to the custom confocal setup (described in chapter 3.1.2.3) for most of the experiments which were carried out in plant cells. The custom setup allowed for the laser beam to be pointed at a single spot in the nucleus for an arbitrary amount of time in order to perform selective photoswitching. In contrary to that the 'FRAP' program of the LSM 710 had some limitations, like solely being able to scan a small given ROI repeatedly, and thus, switching a

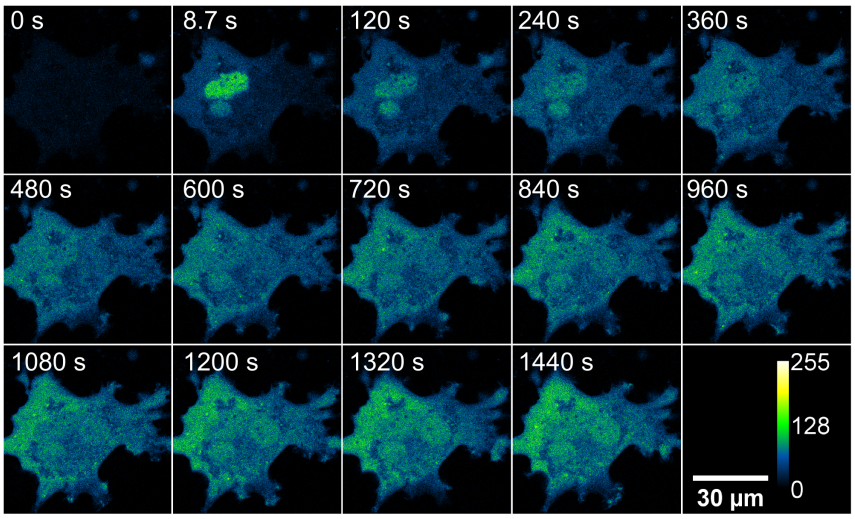

Figure 4.11: Dronpa-s within the nucleus of Cos-7 cells selectively switched to on-state.
Transiently transfected Cos-7 cells expressing Dronpa-s, were imaged on a standard confocal setup (see chapter 3.1.2.1). The 'FRAP' program of the LSM software (Zen, Zeiss) was used to specify a small region of interest within the nucleus. Next the ROI was irradiated by 458 nm light and a subsequent time lapse image sequence was recorded (488 nm).

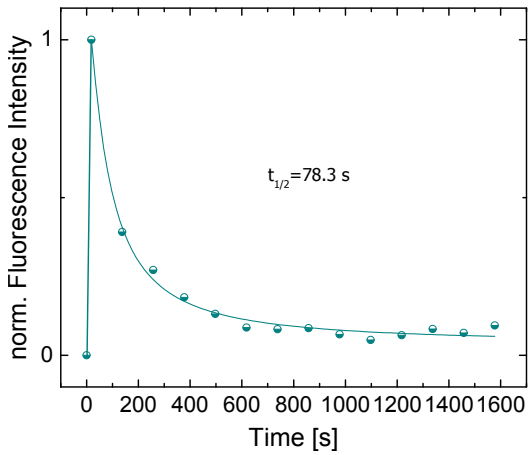

Figure 4.12: Intensity decay plot of fluorescence within Cos-7 nucleus.
The decay in fluorescence intensity was fitted by a logistic model.

bigger area. While not being a problem with the big nuclei in Cos-7 cells, because of their big nuclei, this sometimes led to unintended switching of parts of the cytoplasm in *Arabidopsis* cells.

Considering that and the results of the proof-of-principle-experiments described in chapter 4.1, which identified the minimum switchable spot size, it was possible to selectively switch nuclei in *Arabidopsis* cells. A first success is shown in figure 4.13. Here, a direct comparison of fluorescence images before (figure 4.13 a) and after (figure 4.13 b) selectively switching off the fluorescence within the nucleus, is given. As can clearly be seen, there is a sharp edge separating the dim nucleus from the still fluorescent rest of the cell. This demonstrates, that just *At*GRP7-Dronpa-s molecules within the nucleus were affected by the laser beam and thus switched to the off-state (figure 4.13 b). In case of non-selective switching, a gradual transition from a dim switched region to the brighter environment has to be expected.

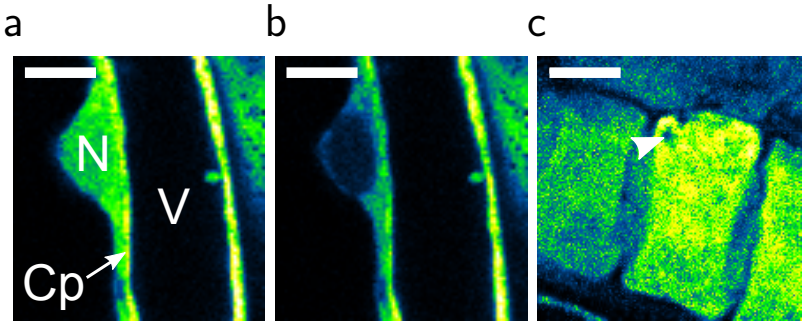

Figure 4.13: Selectively photoswitching Dronpa-s within a cell nucleus of *Arabidopsis*.
All images were acquired using the custom confocal setup, as described in chapter 3.1.2.3. (a) Image taken before switching. Nucleus (N), Cytoplasm (Cp) and Vacuole (V) are marked. (b) Image obtained instantly after photoswitching. Fluorescence within the nucleus was selectively switched off. (c) The depicted cell was fixed with paraformaldehyde prior to image acquisition. The photo-switched region is comparably small and thus denoted by an arrowhead. The scale bars correspond to 10 µm.

The assumption that the technically switched region exhibits a compa-

rable size as shown in figure 4.2 for recombinant Dronpa-s embedded in PVA, is verified by figure 4.13 c. Here *Arabidopsis* root cells were fixed with paraformaldehyde, rendering diffusion impossible. The same treatment as applied in figure 4.13 c yielded a dark spot of comparable size to the aforementioned PVA-experiment. Although, the concentration of recombinant Dronpa-s embedded in PVA, probably differs by far from the *At*GRP7-Dronpa-s concentration within *Arabidopsis* cells, the spot size of off-switched molecules is not altered significantly, if laser power and dwell time are reasonably set. The difference in size of the off-switched areas in figure 4.13 b and c, should thus be attributed to diffusion of the Dronpa-s protein inside the nucleus, which is fast in comparison to the import of fluorescent proteins from the cytoplasm via the NPCs. This also explains the sharp edge between dim nucleus and bright cytoplasm in figure 4.13 b.

Finally, selective photoswitching experiments were carried out in *Arabidopsis* cells expressing *At*GRP7-Dronpa-s. These experiments were designed to reveal the mechanisms which underlie the transport of *At*GRP7-Dronpa-s through the NPCs. Analogue to the experiments in Cos-7 cells, the selective photoswitching of fluorescence within the nucleus was followed by a successive fluorescence recovery (figure 4.14). A reference sample consisting of root cells expressing only Dronpa-s (not the fusion protein), was probed in the same manner. In this case, monitoring the fluorescence recovery within the nucleus yields a completely different intensity plot (figure 4.15).

Within the first two minutes, a notable amount of Dronpa-s is transported into the nucleus. From then on, the fluorescence starts to decrease successively. This decrease happens due to unintended off-switching during image acquisition. After excitation with 488 nm light Dronpa-s molecules emit an amount of fluorescence photons, according to the quantum yield. However, there is also the chance that they are switched to the off-state, with a respective lower probability, though. Thus, intense 488 nm light, increasing this probability, effectively switches Dronpa-s to the off-state. Therefore, each time obtaining a fluorescence image, a small amount of Dronpa-s is switched to the off-state simultaneously.

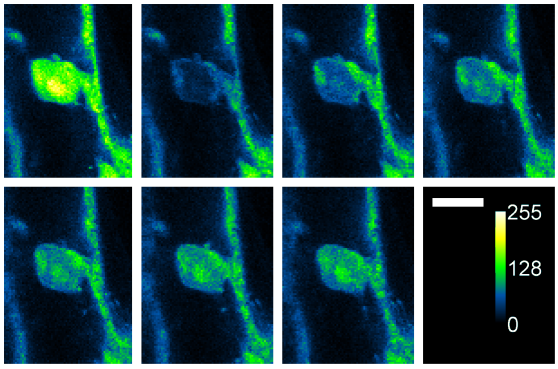

Figure 4.14: Nuclear import of *At*GRP7-Dronpa-s visualized by selective photoswitching.
Root cells of transgenic *Arabidopsis* plants, stably expressing *At*GRP7-Dronpa-s, were imaged on the custom confocal setup (see chapter 3.1.2.3). Fluorescence within the nucleus of a cell was switched off and the recovery was monitored to visualize the nuclear import of *At*GRP7-Dronpa-s. Scale bar: 10 µm.

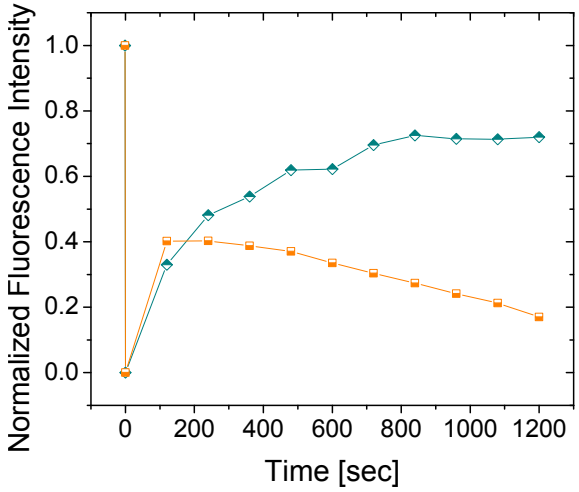

Figure 4.15: Nuclear import kinetics of *At*GRP7-Dronpa-s (blue) and Dronpa-s (orange) by selective photoswitching.
Comparison of the nuclear import kinetics in *Arabidopsis* cells expressing *At*GRP7-Dronpa-s and Dronpa-s respectively. The depicted graphs represent typical kinetics for both plant types.

Due to the rather high concentration of Dronpa-s within the cell, this effect is negligible under usual conditions. In this case, the concentration of fluorescing Dronpa-s molecules within the nucleus, two minutes after off-switching, is comparably low, and therefore, the effect of unintended off-switching is noticeable.

The second conclusion emerging from this experiment is, that Dronpa-s can not be actively imported into the nucleus against a concentration gradient, while this is the case with *At*GRP7-Dronpa-s, in comparison. With analogue experiment design, fluorescence of *At*GRP7-Dronpa-s is still rising within the nucleus after more than two minutes, until the intensity saturates after about 20 minutes. This is evidence for an active transport of *At*GRP7 into the nucleus and against a concentration gradient. It also explains the immense abundance of *At*GRP7 within the nucleus, which was described previously, since it is actively accumulated in the nucleus.

4.3.3 Daytime Dependency in Import Speed

Another interesting finding revealed a dependency between the speed of import and the time of day. Therefore, *Arabidopsis* plants were probed at different relative time points. The relevant point of reference is termed Zeitgeber time (zt) and is set by light stimuli, which are applied on the plants. A time point after the stimulus is denoted by ztH, where H gives the number of hours passed since the stimulus. Thus, zt4 for instance, marks the time point 4 hours after the stimulus.

Selective photoswitching was performed at zt4 and zt11, which corresponds to the time of maximum and minimum *At*GRP7 abundance in *Arabidopsis* (cf. chapter 2.4.4). Figure 4.16 shows the *At*GRP7-Dronpa-s import kinetics of *Arabidopsis* plants at zt4 and zt11 respectively. The shown kinetics differ in import speed, which is denoted by the characteristic $\tau_{\frac{1}{2}}$ times. At zt4 the import is significantly slower than import at zt11. The mean value for ten cells probed at zt11 $\tau_{\frac{1}{2}}$ amounts to 88 s with a standard error $s_x = 8\,\mathrm{s}$, while the import for six cells probed at zt4, averages out at $(150 \pm 17)\,\mathrm{s}$. The molecular basis which

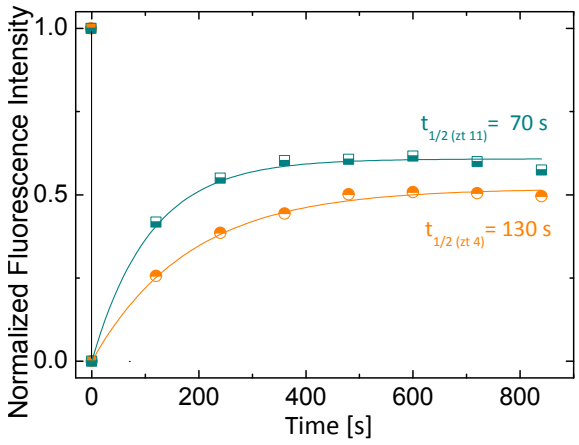

Figure 4.16: Nuclear import kinetics of *At*GRP7-Dronpa-s at two different times of the day.
Shown are representative measurements of *At*GRP7-Dronpa-s import speed at zt4 (orange) and zt11 (blue), respectively. Thereby, the determined $\tau_{\frac{1}{2}}$ times are characteristic parameters, to describe the speed of import.

gives rise to this effect remains unknown. Furthermore, a possible impact on the function of *At*GRP7 can not be determined. A method for regulation the *At*GRP7 concentration within the cells could bear further examination to clarify if this effect is based on the changing *At*GRP7 concentration throughout the day, or if it still exists at equal concentrations of *At*GRP7 in the cell.

4.3.4 Nuclear Export of *At*GRP7-Dronpa-s in *Arabidopsis*

After characterizing the import of *At*GRP7 into the nucleus of *Arabidopsis* cells, the fate of the proteins in the nucleus remained unknown. Therefore, a possible export of *At*GRP7-Dronpa-s was examined by selectively switching fusion proteins inside the nucleus to the on-state. Previously to that, all fusion proteins in the whole cell were switched to the off-state. As a result the export of *At*GRP7-Dronpa-s could be visualized as displayed in figure 4.17. One minute after switching

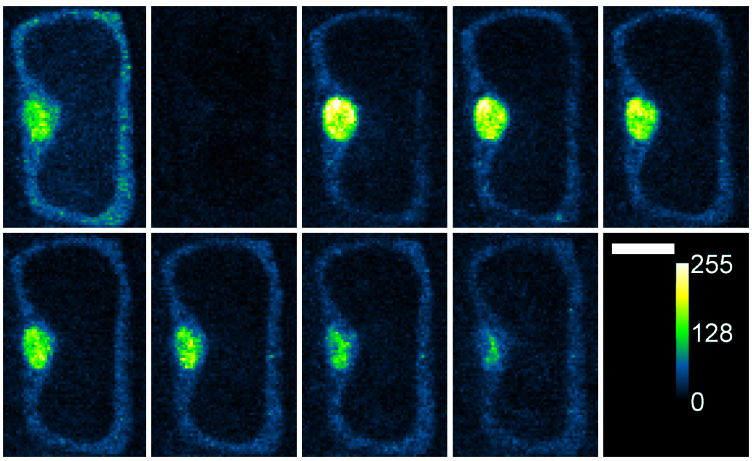

Figure 4.17: Nuclear export of *At*GRP7-Dronpa-s visualized by selective photoswitching.
Root cells of transgenic *Arabidopsis* plants, stably expressing *At*GRP7-Dronpa-s, were imaged on the custom confocal setup (see chapter 3.1.2.3). First all *At*GRP7-Dronpa-s molecules in the cell were switched to the off-state. Subsequently the fluorescence within the nucleus of a cell was switched on and the following decay was monitored to visualize the nuclear export of *At*GRP7-Dronpa-s. Therefore, a fluorescence image was recorded every minute.

*At*GRP7-Dronpa-s to the on-state selectively, the nucleus exhibited a high fluorescence intensity, as expected. The cytoplasm regions in direct vicinity to the nucleus also bore a faint fluorescence. While time progresses the fluorescence within the nucleus decays successively, as fluorescent *At*GRP7-Dronpa-s is dispensed to the whole cytoplasm. Analyzing the fluorescence decay specifically in the nuclei of six different cells, yielded an average $\tau_{\frac{1}{2}}$ of (127±27) s. Therefore, the export occurs with similar speed as the import. No significant difference of $\tau_{\frac{1}{2}}$ values at different relative time points was detected. This suggests that *At*GRP7 undergoes a bi-directional nucleocytoplasmic shuttling, while only the import speed is significantly impacted by the time of day. In mammalian cells, proteins with a high homology to *At*GRP7 are known to undergo a comparable shuttling due to their M9 domain

[Bogerd et al., 1999]. This gives rise to the assumption that the M9 domain of *At*GRP7 mediates its nucleocytoplasmic shuttling. However, export kinetics in plants, expressing solely Dronpa-s, could not be quantified due to the comparably low concentration within the nucleus. This results in a weak fluorescence signal after photoactivation within the nucleus, which is subject to unintended off-switching during image acquisition. Thus, a subsequent monitoring of (export induced) fluorescence decay is not possible, since all signal is lost after recording 2 – 3 images. Therefore, an active export cannot be discriminated against diffusion and can only be speculated.

4.4 RNA-binding of *At*GRP7

As previously described in chapter 2.4.4, *At*GRP7 is known to bind to its own pre-mRNA, inducing an alternate splicing. This mechanism builds the motor for the circadian oscillation of *At*GRP7 and its transcript throughout the day. Thanks to the findings learned in the previous chapter of this work, it is evident, that the *At*GRP7 protein is actively pumped into the nucleus where its pre-mRNA is located. This suggests, that a high concentration of *At*GRP7 is necessary for effective binding to is pre-mRNA.

The binding of *At*GRP7 was studied before by Schöning et al. [2007], Staiger et al. [2003]. Therefore, it is known, that the pre-mRNA *AtGRP7* features two binding sites, one in its 3'UTR region and another in its intron region. Binding of *At*GRP7 to the 3'UTR site was examined in detail, delivering a dissociation constant (K_D value) of 10^{-7} M [Schüttpelz et al., 2008].

4.4.1 FCS binding study

To complete the picture and learn more about the binding process, the intron site of *AtGRP7* was probed in FCS binding studies in this work. First, the binding of *At*GRP7 to the putative binding site in the second half of the intron was characterized by determining a K_D value as a measure for the affinity of the binding partners, while the K_D is defined as the inverse of the association constant K_A:

$$K_D = \frac{[A][B]}{[AB]} = \frac{1}{K_A} \tag{4.1}$$

A DNA oligo (Int), resembling the sequence of intron binding site (compare table 4.1 and Sequence 1 on page 35), was labeled with the fluorophore Atto655 (AttoTec, Germany). In this work, DNA was preferred over RNA due to the ease in handling the samples, considering that *At*GRP7 is known to bind to DNA and RNA with comparable efficiencies [Schüttpelz et al., 2008].

A 10^{-10} M concentrated solution was probed in an FCS diffusion study. Subsequently, purified *At*GRP7 protein was added to successively increase the protein concentration. This titration is shown in figure 4.18. The K_D value for the binding could be determined to $(3.9{\cdot}10^{-7} \pm 5{\cdot}10^{-8})$ M. However, binding to the intron is slightly weaker than reported for the 3'UTR site [Schüttpelz et al., 2008]. Generally, a K_D value in the regime of 10^{-7} M marks a rather weak binding. Highly efficient binding processes known from molecular biology yield K_D values in the nM range. This may be one explanation for *At*GRP7 being actively pumped into the nucleus. Thus, the rather weak binding could be compensated by increasing the concentration of the binding partner.

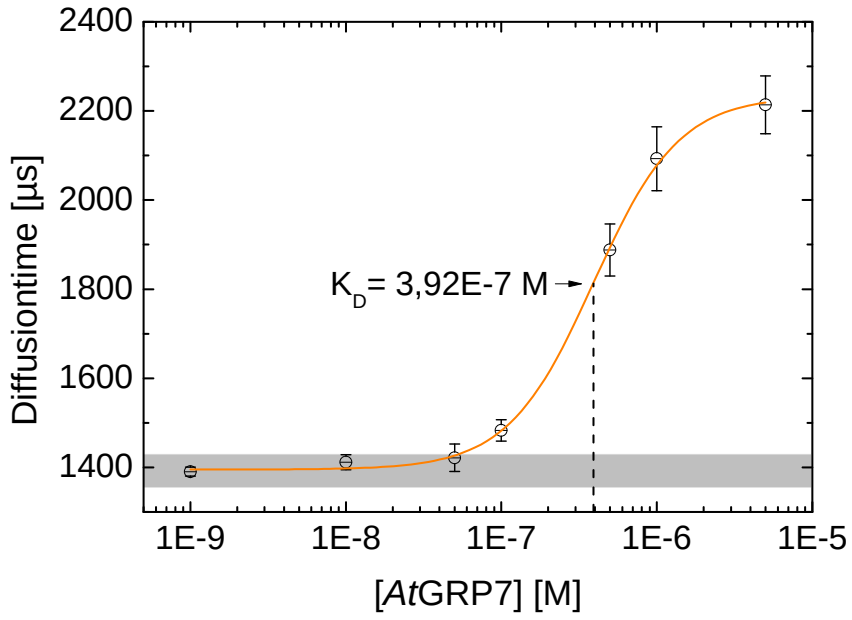

Figure 4.18: Binding of *At*GRP7 to the intron site of its transcript probed by FCS.
Characteristic diffusion time τ_D plotted against *At*GRP7 protein concentration. The point of inflection, obtained by fitting the data with a sigmoidal model, denotes the dissociation constant (K_D) of the binding. The gray area at the bottom denotes the characteristic diffusion time of oligo without *At*GRP7 protein.

4.4.2 Mutational binding site analysis

In a further step, a core binding sequence within the intron site was identified. Therefore, different oligonucleotides labeled with the fluorophore Atto655 were examined. The respective sequences are listed in table 4.1.

Table 4.1: Sequences of oligonucleotides: *AtGRP7* intron (second half) and candidates for the core binding sequence

	Sequence 5' - 3'	$\Delta\tau_D$ [µs]
Int	TTC AGT TTT GTT GGA TTG TTT TGC TGA TCT G-Atto655	729±34
Seq1	TTC AGT TTT GTT-Atto655	132±11
Seq2	TT GGA TTG TTT T-Atto655	456±16
Seq3	TT TGC TGA TCT G-Atto655	304±30

Via FCS the characteristic diffusion time τ_D was measured in a 10^{-10} M concentrated solution of each oligo. In a second step the oligo samples of each sequence were incubated with 10^{-6} M purified *At*GRP7 for 15 minutes. After that, the mixed samples were probed for the characteristic diffusion time τ_D by means of FCS. Upon binding of *At*GRP7 to the respective oligos, an increase of τ_D was detected. The higher the increase ($\Delta\tau_D$) in diffusion time, the more stable was the binding process. As can be seen in table 4.1, the oligo sequence Seq2 exhibits the highest $\Delta\tau_D$ value at binding, and thus was identified as the core binding sequence. Note, that a comparison of $\Delta\tau_D$ values is only reasonable, if the oligos are of the same length, since bigger oligos are supposed to exhibit a bigger hydrodynamic radius, and therefore, intrinsically yield higher diffusion times. This is demonstrated in table 4.1, where the full length oligo Int yields a by far higher $\Delta\tau_D$ value than the fragment sequences. K_D values for Seq2 and Seq1 were determined to $(4{,}47\pm0.53)\cdot10^{-7}$ M and $(1.75\pm0.09)\cdot10^{-6}$ M, respectively, supporting the given interpretation of $\Delta\tau_D$ values.

However, also Seq3 shows a notable binding, compared to Seq1, which yields a 2-3 fold lower $\Delta\tau_D$. In consequence to that, Seq2 and Seq3 were combined to another oligo for the following experiments. This

extended oligo was termed Seq4 and its sequence was mutated at several sites as listed in table 4.2. By inserting mutations, the sequence specificity of *At*GRP7 in binding to its transcript was examined. Since Seq1 exhibits no reasonable binding with *At*GRP7, it was excluded for this experiment.

Table 4.2: Sequences of Seq4 oligonucleotide and the mutated forms Mutation sites are highlighted in red. Pyrimidines were exchanged by pyrimidines and purines by purines.

	Sequence 5' - 3'	$\Delta\tau_D$ [µs]
Seq4	Atto655-TTG GAT TGT TTT GCT GAT CTG	599 ±45
Seq4-mut1	Atto655-TTG GAT TGT CCT GCT GAT CTG	502 ±31
Seq4-mut2	Atto655-TTG AAT TGT TTT GCT GAT CTG	575 ±28
Seq4-mut3	Atto655-TTG GAT CGT TTT GCT GAT CTG	281 ±21
Seq4-mut4	Atto655-TTG GAT TAT TTT GCT GAT CTG	553 ±25
Seq4-mut5	Atto655-TTG GAT TGT TTT ACT GAT CTG	457 ±36
Seq4-mut6	Atto655-TTG GAT TGT TTT GCC GAT CTG	436 ±49
Seq4-mut7	Atto655-TTG GAT TGT TTT GCT AAT CTG	225 ±44

As can be seen in table 4.2, two of the point mutated sequences induced a significant loss in binding efficiency. Seq4-mut3 and Seq4-mut7 both hardly show any binding by *At*GRP7, which is indicated by the comparably low $\Delta\tau_D$ (cf. table 4.2). These findings suggest that Seq4 harbors one or more important binding motifs. Notably, mut7 was embedded into the second half of Seq4 formerly represented by Seq3. Thus, Seq3 contributes significantly to the binding site, though it exhibits a slightly weaker binding than Seq2. Moreover, the mutational analysis shows the specificity of the binding motifs within Seq4, and thus, their contribution to stabilizing the binding of *At*GRP7 to the intron region of the transcript.

4.4.3 Conformational changes upon binding

It has to be assumed that the binding sites within the complete transcript sequence are not directly available to *At*GRP7 for binding,

but rather are masked by secondary structures like hairpin loops. In a further experiment the binding of *At*GRP7 to the binding motif hidden in a secondary structure was examined. Therefore, a fragment of Seq4 was forced into a hairpin structure upon mutation. Sequence 3 displays the hairpin design. The stem consists of three base pairs and the loop region holds a sequence of 7 bases. Two point mutations had to be inserted to assure base pairing within the stem. Thus designed, the oligo fragment can form a secondary structure hairpin loop at room temperature, as displayed in figure 4.19.

Sequence 3: Hairpin designed from oligo Seq4
Hairpin fragment is highlighted: Stem in yellow, loop in orange, point mutations in blue. First row shows the native sequence.

```
1 TTGGATTGTT TTGCTGATCT G
1 TTGGATTGTT TTTCCGATCT G
```

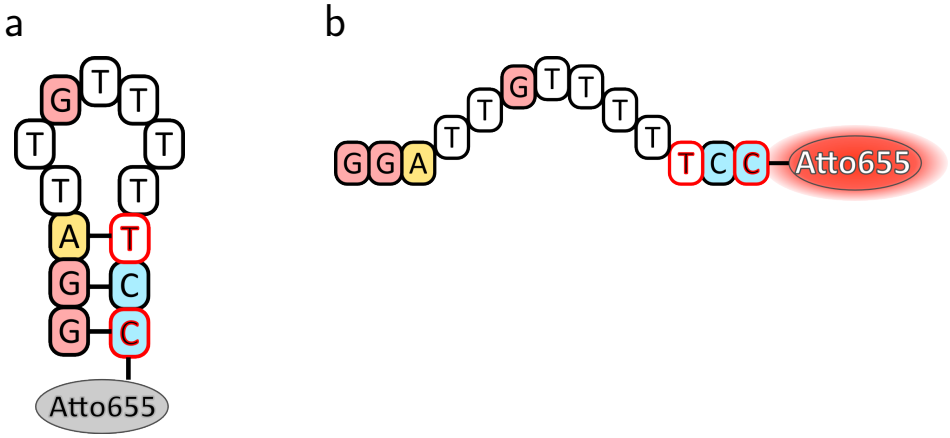

Figure 4.19: Schematic representation of the designed hairpin.
a) In the closed form the Atto655 at 3'-end is quenched due to Van-der-Waals-contact with the guanosine residues at 5'-end. b) The open form gives rise to the separation of both ends and thus inhibits the quenching of Atto655, which again can emit fluorescence upon excitation.

Of further importance is the 5'-end, which exhibits a terminal guanosine residue. The 3'-end was coupled to an Atto655 fluorophore. If the hairpin exists in its closed form, guanosine (5'-end) and Atto655 (3'-end) are in direct vicinity. Due to this, a quenching of Atto655 is accomplished by photoinduced electron transfer (cf. chapter 2.2.2; further reading: Doose et al. [2009]). The open form separates guanosine and Atto655, thus a fluorescence signal can be obtained.

At room temperature the hairpin is not permanently closed. Open and

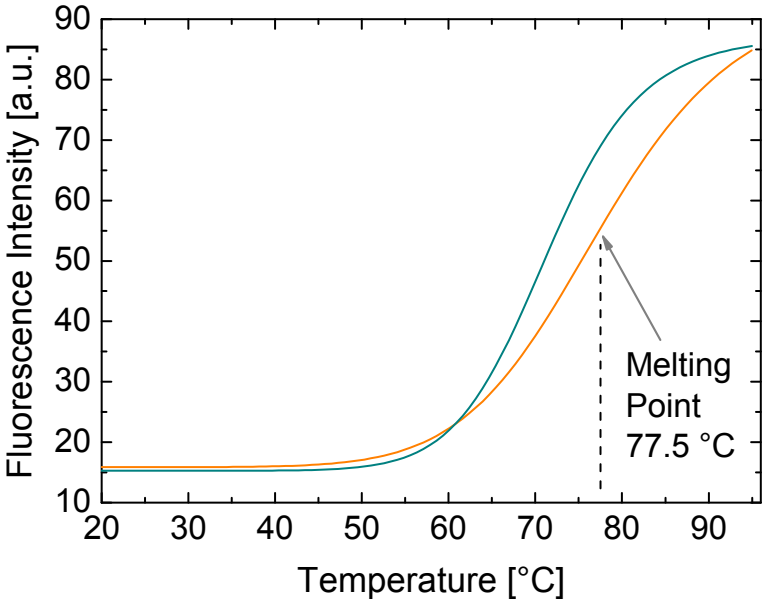

Figure 4.20: Melting of the hairpin structure visualized by plotting the fluorescence intensity against the temperature.
With increasing temperature the hairpins melts to the open form (orange). The temperature at which 50% of the hairpins exist in the open form is considered the melting point. The fluorescence intensity correlates linearly to the concentration of melted hairpins, as the fluorescence is quenched efficiently in the closed form. By cooling the sample to room temperature again, the hairpins re-engage their closed form (blue).

closed forms are in a steady state equilibrium with an emphasis on the closed form. With higher temperatures the equilibrium is pushed towards the open form, as can be seen in figure 4.20.

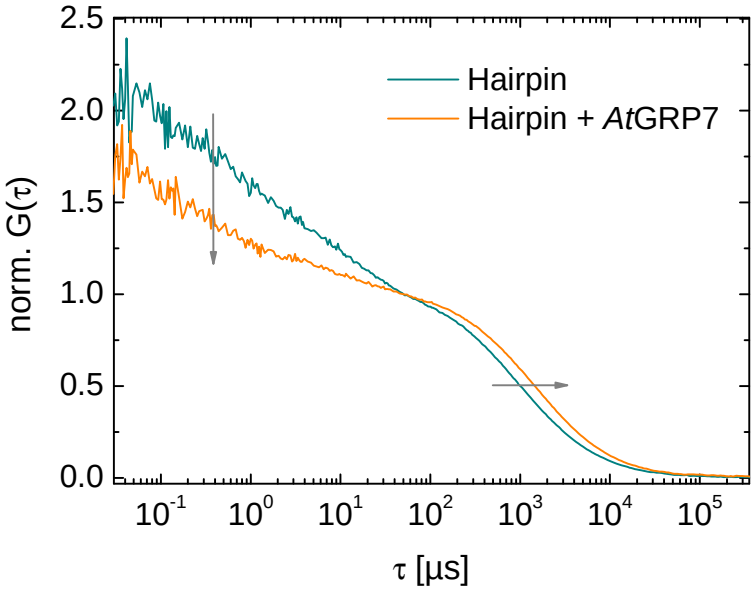

Figure 4.21: Conformational changes induced to hairpin at binding of *At*GRP7.
FCS correlation curves for hairpin only (blue) and hairpin incubated with *At*GRP7 (orange). The curves were normalized to the number of particles. The shift in diffusion time denotes binding (horizontal arrow) and the shift in the µs regime reveals a change in the conformational activity of the hairpin.

An FCS analysis can reveal the kinetics of periodical opening and closing of the hairpin, accompanied by fluorescence quenching and emission respectively, as described in chapter 2.2.3. In contrary to measuring conventional fluorophores, the number of particles, obtained by FCS studies, can only resemble apparent values. An efficiently quenched hairpin will always exhibit a lower number of particles compared to an un-quenched fluorophore of same concentration, because the majority of hairpin particles are quenched and thus not considered in FCS studies.

Such an analysis was performed to probe for conformational changes within the transcript *AtGRP7* upon binding to *At*GRP7 (figure 4.21). The FCS correlation function for the hairpin indicates a τ_D of (992 ± 95) µs, and an average of $N = 1.0 \pm 0.1$ apparent particles within the detection volume. The steep slope in the µs and sub-µs range indicates high conformational activity, thus, periodical opening and closing of the hairpin. In contrary to that, the correlation function of the hairpin incubated with purified *At*GRP7 yields a higher τ_D of 1394 ±99 µs, which indicates the binding. Furthermore, an increase of apparent particles within the detection volume to $N = 1.65 \pm 0.1$, denotes a clear emphasis to the open hairpin form. This is also supported by the comparably shallow slope in the (sub-)µs range, suggesting low conformational activity.

Drawn together, these findings reveal the preference of *At*GRP7 to bind to its transcript in an open single stranded form. Thus, binding sites previously masked by secondary structures are stretched upon binding of *At*GRP7. This result complies with the studies of *At*GRP7 binding to the 3'UTR of its transcript [Schüttpelz et al., 2008].

4.5 *At*GRP7 relates to Stress-Response

The capabilities of *At*GRP7 to bind RNA may also relate to its assumed role in the stress response pathway of *Arabidopsis* (see chapter 2.4.4). An interesting remark regarding the role of *At*GRP7 in stress response is the observation, that upon cold stress and oxidative stress *At*GRP7-Dronpa-s agglomerates and beads out within the cytoplasm. This behavior was revealed while taking fluorescence images of *Arabidopsis* root cells expressing *At*GRP7-Dronpa-s with the intention to examine the nucleocytoplasmic shuttling, as described in chapter 4.3. Which type of stress induced the aggregation during this particular imaging session remains unknown.

However, at 10 °C as well as 1h after treatment with arsenide *At*GRP7-Dronpa-s reproducibly builds small aggregates of about 100 – 500 nm size in the cytoplasm as displayed in figure 4.22 a. This kind of distribution throughout the cell is also known from processing bodies and stress granules, both particles related to stress response in *Arabidopsis*. Physiologically both types of particles give rise to an alteration of the protein expression at the posttranscriptional level. This enables the plant to immediately adopt to the environmental changes inducing stress. That might hint at a contribution of *At*GRP7 in those particles. Even more, as an accumulation of RNA and other RNPs to p-bodies and stress granules has been reported [see Buchan and Parker, 2009, Buchan et al., 2008, Kedersha et al., 2005].

In fluorescence microscopy, such molecular interactions, are typically visualized and quantified by colocalization studies. Most commonly used parameters that can measure the degree of colocalization in multi-channel fluorescence images, are the Pearson Correlation Coefficient (PCC) and the Manders Overlap Coefficient [Manders et al., 1992], which are implemented in most commercial software packages for image processing [Adler and Parmryd, 2010]. A closer look at the PCC reveals that it has some major drawbacks, rendering it hardly usable for colocalization analysis in this particular scenario.

The PCC, which takes on values between +1 and -1 as a measure of the similarity of channels (+1: perfect colocalization; -1: anti-

colocalization), is very sensitive to intensity fluctuations and threshold variations. Additionally the PCC appears to be very sensitive to high background signals and therefore a high signal-to-noise ratio (SNR) is required to perform the analysis. Analogously the PCC delivers unreasonable results if the noise levels of the channels differ significantly. In some cases the PCC analysis returns negative values which are hard to interpret reasonably.

The major problem here was that the PCC often fails, if regions of interest contain a certain amount of colocalized pixels, mixed with a fraction of signals that do not colocalize, as seen in figure 4.22 c. Therefore, a PCC based colocalization study of *At*GRP7-Dronpa-s and stress granules or p-bodies demands setting ROIs to each solitary particle. Doing so results nonetheless in a highly biased PCC value, due to the small amount of pixels analyzed. Moreover, the examiner has to provide additional, most certainly biased, spatial information to the PCC analysis, by determining the ROIs manually.

Emerging from this challenge, a completely novel approach to colocalization studies was afforded. Inspired by a recent advance to determining coincident events in single molecule studies reported by Yahiatène et al. [2012], the correlation matrix method was introduced to colocalization analysis. Before this novel and enhanced method is elaborated in detail in chapter 4.6, it is applied in a colocalization study of *At*GRP7 and processing bodies.

As seen in figure 4.22, leaf cells of *Nicotiana benthamiana* were treated to transiently express the fusion proteins *At*GRP7-eGFP and DCP1-mCherry. The sample was exposed to arsenide for 1 h previous to imaging to induce oxidative stress. DCP1 is used as a reporter protein for processing bodies. The marginal spectral overlap between the two fluorophores enables imaging without notable cross-talk signal in the respective channel. Aggregation under stress condition of *At*GRP7-eGFP is shown in figure 4.22 a, while the processing bodies marked by DCP1-mCherry are displayed in figure 4.22 b. Figure 4.22 c exhibits an overlay image of both channels. The white line indicates the linear selection pattern on which the Γ-norm colocalization analysis was performed on. Due to the chain-like distribution of marked structures

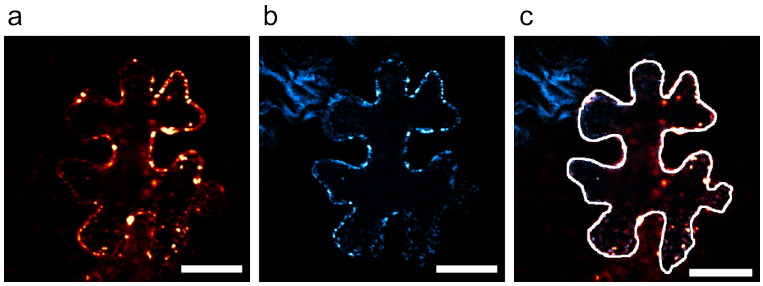

Figure 4.22: *At*GRP7- processing bodies colocalization analysis in plant cells.
(a) *At*GRP7 protein was fused to a fluorescent marker (eGFP) in a *Nicotiana benthamiana* epidermal leaf cell (scale bar = 70 µm). (b) The same cell also expresses another fluorescent reporter (DCP1-mCherry), highlighting processing bodies. (c) Colocalization of the RNA-binding protein and processing bodies was tested. Note that all images (a-c) were adjusted in contrast for display purposes, while the evaluation was performed on the original images.

within the cytoplasm, a linear selection was preferred over the usual regional selection approach (ROI). The resulting intensity profile plots can be analyzed with the novel Γ-norm algorithm. Γ_2 yielded a value of 1.52 which clearly reports a major fraction of colocalized pixels. A conventional PCC analysis returns a value of 0.67. The Γ-norm analysis additionally provides distance information of the colocalized structures. The average distance between the processing bodies along the cytoplasm was found to be (8.3 ±3.4) pixel (px) or equivalently (3.8 ±1.58) µm.

These findings suggest a contribution of *At*GRP7 to processing bodies under oxidative stress conditions. Furthermore, an average distance between processing bodies was easily extracted out of the data provided by the novel Γ-norm algorithm and may be of further interest to study the stress response pathway of plants.

4.6 Quantifying molecular colocalization in live cell fluorescence microscopy

In order to apply the correlation-matrix method [Yahiatène et al., 2012] to image data one has to first transform the image into a linear intensity trace. This linear plot could be assembled from an arbitrarily chosen path within the image, or it could just be a linear display of the confocal image scan, where each successive line is concatenated with the preceding line, resulting in a linear trace. This intensity profile is then divided into N sections (not necessarily of equal length). For each section a Hermitian correlation matrix is determined, and the Euclidian length Γ of a vector built from elements of the matrix is calculated. The size of the matrix and the length of the vector depend on the number of channels that are analyzed for correlations and they can be readily expanded beyond just 2 colors, making it possible to easily determine multi-channel correlations, or, in the case of images, colocalizations.

To demonstrate the performance and robustness of this method, first test images consisting of 3 different color channels with different degrees of colocalization (random, 50% and 100%) were analyzed (figure 4.23). The Γ-norm for each image for just two color channels, as well as for all three color channels, was calculated. Furthermore, the Γ-norm was determined for all pixels with an intensity value above a threshold of $T=\mu+3\sigma$ (mean pixel value plus three standard deviations).

For the image shown in figure 4.23 a, i.e. the image containing only randomly colocalized pixels, a value of $\Gamma_2 \approx 0.36$ was obtained. A Γ-norm well below 1 indicates a sample containing a large fraction of randomly colocalized intensity values. A colocalization analysis of all three color channels exhibited a norm of approximately 0.28 which is below the critical value of approximately 0.88 for three channels (see equation (3.7) on page 45). Figure 4.23 b shows an image where 50% of all pixels are colocalized, resulting in Γ-norm values of $\Gamma_2 \sim 1.37$ and $\Gamma_3 \sim 1.72$, which clearly signalizes the presence of a large number of colocalized pixels.

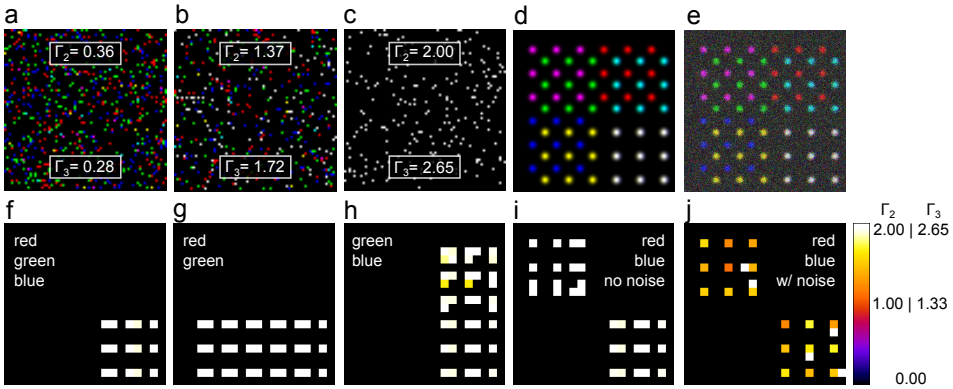

Figure 4.23: Determining the quality of the Γ-norm as a measure of colocalization with test images.
Top row: Three test images representing three different color channels (red (R), green (G), blue (B)) were created to assess the quality of the Γ-norm as a measure of their degree of colocalization. The RGB images are a result of the addition of the three separate channels and also contain the corresponding Γ-norms calculated for the entire image if only two channels (Γ_2: red and blue) or all three channels (Γ_3) are taken into account. (a) Image pixels in all three channels are randomly distributed, (b) 25% of all the pixels are colocalized, and (c) 100% of all the pixels are colocalized. Image (c) exhibits 100% colocalization and yields maximum values for Γ_3 and Γ_2. (d) A Manders test image was modified to feature 3 color channels (RGB) and serves as a test image for the retrieval of colocalized image features based on the Γ-norm. (e) Specified Gaussian noise (sd=43) was added to the test image shown in (d). Bottom row: Reconstructed images indicating colocalized regions of the test image in (d). Each pixel in these images is obtained by calculating the Γ-norm of a 20×20 pixel area in (d). (f) Colocalization of all image channels, (g-i) combinations of 2 channels, respectively. (j) Two-channel colocalization analysis of image (e) including noise. The calibration bar on the right hand side shows the color-coded Γ-norm values determined for each image, for both two-channel and three-channel colocalization analysis.

In figure 4.23 c all relevant pixels are colocalized in all three channels resulting in white pixels in the overlay and Γ-norms of $\Gamma_2 = 2$ and Γ_3 approximately 2.65. This set of simulated images (figure 4.23 a-c) shows the numerical range that the Γ-norm can adopt for 2-channel colocalizations (0 – 2), as well as for 3-channel colocalizations (0 – 2.65). The Γ-norm values given in figure 4.23 a-c can be considered independent of the image dimensions. Smaller (or larger) images will contain the same relative amount of random colocalizations. To better compare the Γ-norm analysis to PCC and MOC results, the well-known Manders test image (figure 4.23 d) was expanded to 3 color channels, and thus analyzed.

A feature of Γ-norm analysis is that a relatively small number of pixel is sufficient to reliably calculate the Γ-norm. Thus, the image was split into superpixels, which correspond to a 20×20 pixel array in the original Manders test image. Then the Γ-norm for each pixel array was calculated. Subsequently, the superpixels, which encode for the Γ-norm using a color scale to indicate areas of high or low colocalization in the original image, were reassembled to reconstruct the image. This methodology was applied to every channel combination of the three different color channels in the Manders test image (figure 4.23 f-i). To make this analysis useful for any size image, the number of superpixels in the x– and y–direction can be easily calculated by $SP_x = \sqrt{x}$ and analogously $SP_y = \sqrt{y}$ as a rough approximation, where x and y are the pixel dimensions of the original image.

Another test image was created, to further understand the influence of noise on the analysis. In the test image, Gaussian noise with a standard deviation (sd) of 43 was added to all three channels of the Manders test image (figure 4.23 e) and the Γ-norm topology was calculated for the red and blue channels (figure 4.23 j). For the reconstructed image 20×20 superpixels at 30 sections were calculated. As can be seen in figure 4.23 j no structural information was lost during the reconstruction process. The obtained mean Γ-norm of approximately 1.82, indicates excellent colocalization between the sample features.

4.6.1 Experiments with autofluorescent beads

Laser scanning fluorescence microscopy was performed on the custom confocal setup (see chapter 3.1.2.3) to image autofluorescent beads with a diameter of 2.8 µm adhered to a dry glass surface (figure 4.24 a). This provided a reference sample containing a major fraction of colocalizing pixels.

These particles exhibit intense and spectrally broad autofluorescence emission upon excitation at 405 nm with an excitation power of 30 µW. Images which serve as perfect experimental three-color colocalization samples, were obtained by detecting the autofluorescence signal simultaneously on three detectors using different bandpass filters.

With this perfect colocalization sample also the robustness against noise of Γ-norm colocalization analysis was determined by successively adding noise to these images (figure 4.24 a). Performing the Γ-norm analysis on the unchanged image, the Γ-norms was calculated to be Γ_2~1.98 and Γ_3 approximately 2.62, indicating a near to perfect colocalized sample. Varying the threshold level by ± 15%, and therefore including more or fewer background pixels, resulted in a minor change of approximately 2.8% of the Γ-norm values. This example shows that the Γ-norm holds well against changes in the absolute number of signals (e.g. fluorophore concentration) or threshold values, and thus, is able to detect even low fractions of colocalized pixels. The robustness of this technique also implies that the results will not be sensitive to inadequately chosen filter sets, which is considered the most common problem in fluorescence microscopy. These data show one of the major strengths of the Γ-norm analysis compared to conventional methods for evaluating colocalization. Here, the threshold value can simply be set to the mean intensity value, resulting in a simplification of the analysis.

By using the image processing environment Fiji, noise was added with successively increasing amplitude to one channel of the two-color bead measurement (figure 4.24 a and b). All data were analyzed with a threshold of δ=3 if not stated otherwise. Subsequently, the Γ_2-norm

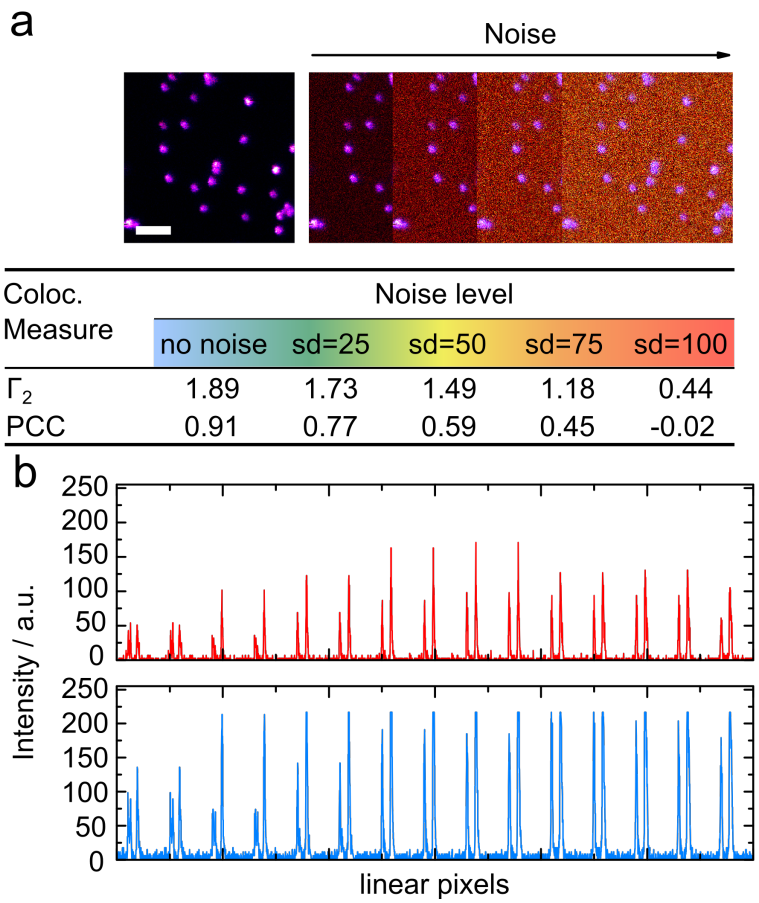

Figure 4.24: Robustness of the Γ-norm against the addition of noise demonstrated with a perfect colocalization sample.
(a) Autofluorescence images of M280 beads on a surface were obtained by confocal fluorescence microscopy using two spectrally different channels. The resulting images were overlaid (scale bar: 20 µm) and exhibit 100% colocalization due to their broad emission. (b) The image from (a) was converted into pixel intensity plots for the two color channels. These traces are then analyzed for colocalization by the Γ-norm-algorithm. Instead of the full image, just the 15 first rows of the image are presented for better visualization. To enable a direct comparison between the Pearson correlation coefficient (PCC) and the Γ-norm for the images, specified Gaussian noise was added to one channel of the bead image in increasing amounts and then analyzed for colocalization with the unchanged channel. The noise level is specified by the standard deviation of the Gaussian noise.

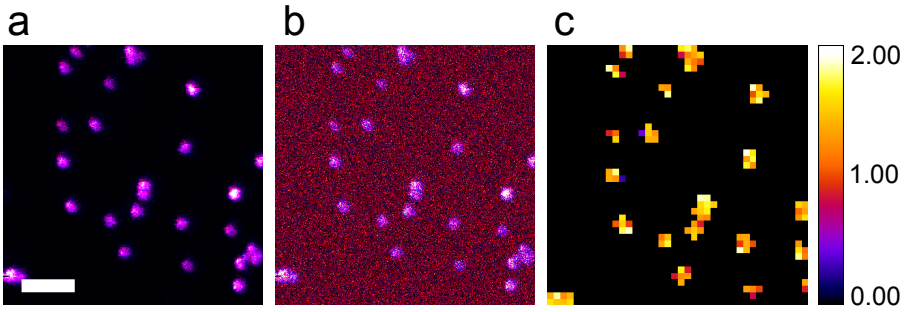

Figure 4.25: Robustness of the Γ-norm topology against noise demonstrated by a sample with 100% colocalization.
(a, b) Autofluorescence images of M280 beads on a surface detected on two spectrally separated channels. (Scale bar: 20 µm). (b) Noise with an sd=100 was added. (c) The corresponding Γ-norm topology image (resolution 20×20 spx) is still able to identify every single bead. Applying even higher noise levels results in a loss of the dimmest beads in the topology image. Up to a noise level of sd=100 the topology still features the majority of beads. The calibration bar on the right hand side shows the color code for the Γ-norm topology image.

was compared to the PCC by checking the red and blue channels for colocalization. At a noise level of sd=75 the PCC already results in a weak correlation between the two images (PCC=0.45) whereas the Γ_2-norm retains a value of approximately 1.2, i.e. well above 1, indicating a significant number of colocalized data points for two-channel data (cf. table in figure 4.24). One of the greatest drawbacks of the PCC (and other numerically very similar parameters) is the undefined interpretability at this point. The new Γ-norm, on the other hand, has a fixed relationship to the anti-fraction (AF), which makes the interpretation simple. At maximum noise the Γ-norm yields a value of 0.44 which corresponds to an anti-fraction of 0.78. Since the value of the Γ-norm is less than 1 in this case, it indicates no significant colocalization. At this point applying filters to remove the noise from the data is no longer possible. For the same data the PCC turns negative with a value of -0.02, which is not meaningful. There is no obvious statistical reason that would explain the anti-correlation between the two channels. This again demonstrates the

stability of the Γ-norm against background fluctuations in comparison to the established PCC. Additionally, the anti-fraction can be directly calculated from the Γ-norm (table 4.3).

To further prove that the Γ-norm enables the extraction of structural information hidden in noise a topology map was calculated, which provides a full reconstruction of the scanned particle image (figure 4.25). Here, noise with a standard deviation of 35 was added to both channels independently. The reconstructed image in figure 4.25 c exhibits Γ-norms still well above 1 for all particles. Images polluted with such a high noise level typically would be dumped immediately. This again demonstrates the robustness of the Γ-norm, yet mastering unreasonably corrupted data.

4.6.2 Live-cell analysis

Next, the Γ-norm analysis was performed on data obtained from live cell imaging experiments, which were carried out on the CLSM (see chapter 3.1.2). In figure 4.26 a, living Cos-7 cells labeled with 3 different fluorophores were imaged. Two of the fluorophores were attached to the very same antibody, and should thus provide physiological colocalization. Tubulin in the cytosceleton of the cell was stained using a primary and secondary antibody, where the secondary antibody was labeled with Alexa 647 and Alexa 488, respectively. The nucleus was labeled with DAPI. Since two fluorophores are targeted simultaneously to the same cellular compartment, the red (Alexa647) and the green (Alexa488) channels were expected to colocalize, while none of both should be colocalized with the nucleus (blue channel). The topology maps computed by calculating the Γ-norm for all possible combinations of 2 color channels at a time, are shown in figure 4.26 b-d. These data show that the red and the green channel (figure 4.26 b) exhibit the highest occurrence of colocalizing events. Combinations with the blue channel reveal some apparent colocalization in the perinuclear region, obviously due to some overexposure and out-of focus fluorescence (figure 4.26 c-d).

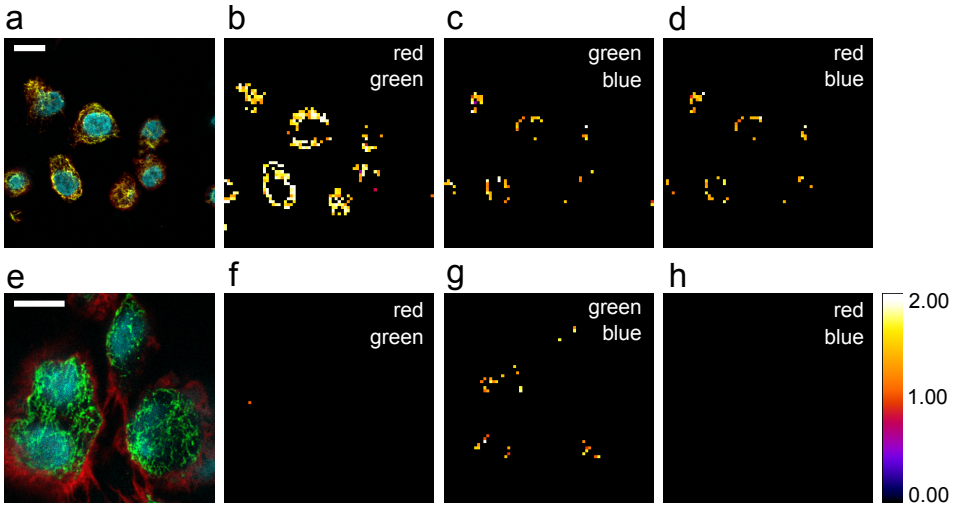

Figure 4.26: Assessing colocalization in multicolor live cell fluorescence images.
(a) Microtubuli in Cos-7 cells were immunostained using an antibody against β-tubulin and two equimolar secondary antibodies conjugated to Alexa 488 (green) and Alexa 647 (red), respectively. The nucleus was stained with DAPI (blue). (b-d) Γ-norm topology images with a superpixel resolution of 70×70 spx show regions of colocalization for each combination of the three color channels. The red and green channels colocalize to physiologically resemble the tubulin distribution, whereas the other combinations show only weak colocalization due to out of focus signals. (e) In a second experiment with Cos-7 cells, actin was labeled with rhodamine-phalloidin (red), while tubulin was labeled as before, but with a single secondary antibody conjugated to Alexa 488 (green). The nucleus was again stained with DAPI (blue). In this case, no physiological colocalization is expected. (f-h) The green and blue channels again exhibit some weak colocalization due to out of focus contributions. Scale bars: 15 µm. The calibration bar on the right hand side shows the color code for the Γ-norm topology images.

Figure 4.26 e shows an image of another set of Cos-7 cells that serve as an example for non-colocalization. Here, three different compartments were labeled with three different fluorophores accordingly, to minimize colocalization of all channels. The actin filaments of the Cos-7 cells were marked by rhodamin labeled phalloidin. Additionally, tubulin filaments were again labeled with Alexa 488, while the nuclei were stained with DAPI, as done before. Within the calculated topology maps, no significant fraction of colocalizing pixels was detectable (figure 4.26 f-h), except for some solitary superpixels representing overlap between microtubuli and the nucleus.

In a next step, cellular structures of again Cos-7 cells were reconstructed by Γ-norm analysis. These images are compared to overlaid and threshold-adjusted images, which claim to highlight regions of apparent colocalization (figure 4.27). Those pixel maps are commonly used by most evaluation software along with the Manders overlap coefficient and the PCC, where only colocalizing pixels above a certain threshold are highlighted (figure 4.27 b and e).

In figure 4.27 a, tubulin again was stained with two spectrally different dyes to provide a sample exhibiting significant colocalization. The corresponding topology map exactly reconstructs the split structure that is visible by eye in the original picture (figure 4.27 c), whereas the pixel map highlights almost every pixel (figure 4.27 b).

Figure 4.27 d shows Cos-7 cells with tubulin and actin stained by different fluorophores, as described previously. The pixel map obtained by analyzing for colocalization, reports nearly every pixel to colocalize. Since this image represents a non-colocalizing sample, no pixels should be highlighted. Notably, the Γ-norm topology returns a by far better result exhibiting very few apparent colocalizations, though.

Finally, the Γ-norm analysis was performed on the live cell imaging experiments in plants described in chapter 4.5. Here, the particular distribution of marked structures demanded to exchange the usual ROI approach for a linear selection scheme. While in principle a PCC analysis can be performed on a liner selection, it is not supported in most colocalization software (probably due to the discussed drawbacks

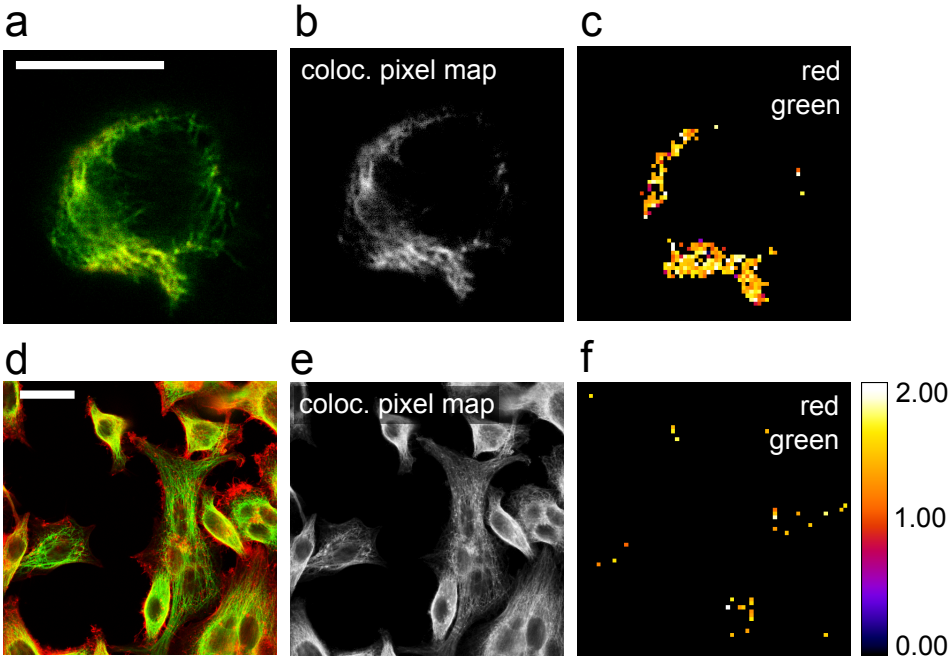

Figure 4.27: Γ-norm colocalization analysis performs better than multi-channel thresholding.
(a) Microtubuli in Cos-7 cells were immunostained using two secondary antibodies (red and green) as described in figure 4.26. (b) Thresholding and overlaying these image channels results in an apparent colocalization. (c) The corresponding Γ-norm topology image with a size of 70×70 spx highlights regions of true colocalization. Scale bar: 15 µm. (d) Actin and tubulin were labeled in Cos-7 cells as described before (red and green, respectively) resulting in no physiologically colocalized regions. (e) The corresponding pixel map based on thresholding and overlaying separate image channels indicates significant apparent colocalization. (f) The corresponding Γ-norm topology image shows that essentially no colocalization occurs in this sample. Scale bar: 30 µm. The calibration bar on the right hand side displays the color code for the Γ-norm topology images.

of the PCC). To demonstrate the scalability of the Γ-norm a zig-zag linear selection roughly covering a region of interest was applied in figure 4.28. Even this rough selection pattern yields reasonable Γ-norm values and again showcases the robustness of the Γ-norm algorithm.

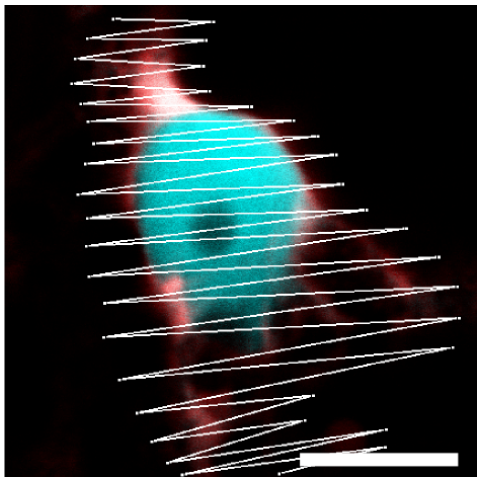

Figure 4.28: Linear selection pattern in Γ-norm colocalization analysis.
*At*GRP7-eGFP (blue) localizes to the nucleus of the cells (scale bar = 10 µm) as shown before (chapter 4.2). An ER-marker fused to mCherry (red) is located in the surroundings of the nucleus. For demonstration purposes a line selection instead of a ROI was chosen, as this already yields valuable colocalization information. An analysis of the extracted linear intensity profile yields a Γ_2 =0.84. As expected the Γ-norm analysis does not register a significant amount of colocalizations.

4.6.3 Analysis of simulated colocalization data

To determine how the Γ-norm behaves for 2 and 3 data channels, respectively, 30 artificially generated test images consisting of 3 color channels with 300×300 binary pixels, each, were computed. Thus the

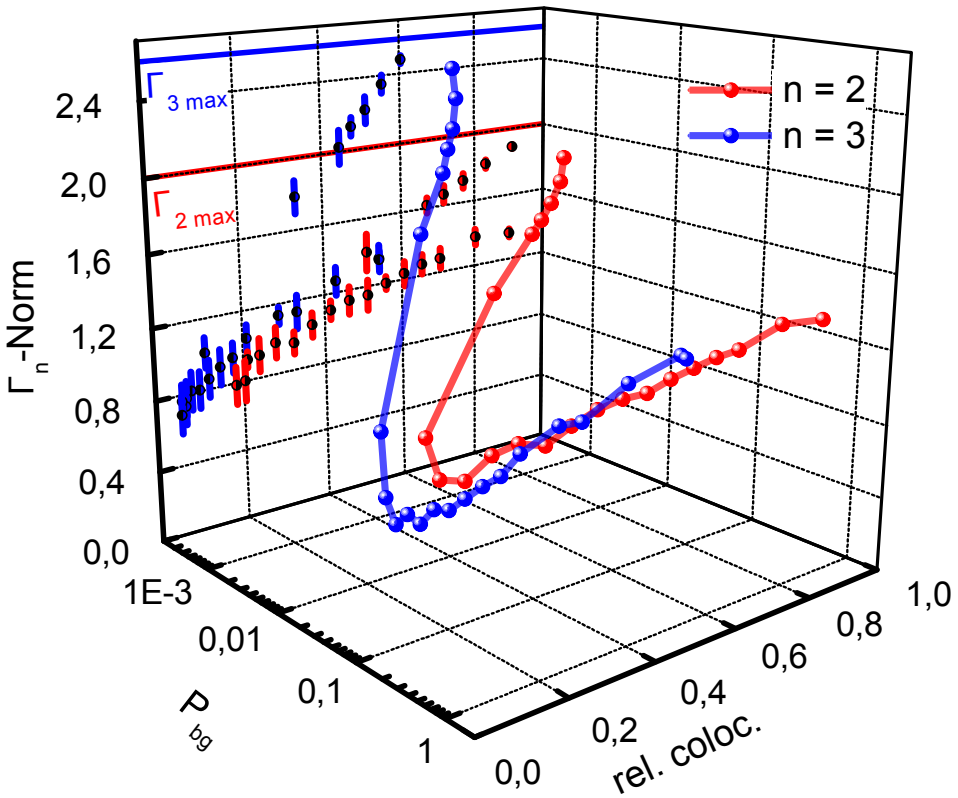

Figure 4.29: Simulations of the noise filtering capabilities of the Γ-norm.
A total of 30 test images, each consisting of 3 color channels with 300×300 pixels, respectively, were created and analyzed. The resulting data points are a measure of the reproducibility of the Γ-norm analysis. Each pixel value was randomly assigned a probability P_c describing the probability of colocalization between the color channels. P_{bg} is the probability for un-correlated signal. Depicted are Γ_3 and Γ_2 as functions of P_{bg} and the percentage of colocalizing pixels. P_c was set to 0.01. The maximum possible value of Γ_3 and Γ_2 is indicated by the straight red and blue lines in the yz-plane. The minimum values occur at a background probability of 0.1, which can be interpreted as a signal-to-noise ratio of 0.1. This minimum in the Γ_3 and Γ_2 values indicates the lowest signal-to-noise ratio for which the Γ-norm analysis can still be successfully conducted.

p The corresponding Γ-norm values were calculated as a function of the background probability P_{bg} and the relative number of colocalizing pixels.

The probability of detecting colocalized pixels was fixed at 1% (figure 4.29). In both cases, for 2 and 3 channel data, the Γ-norm decreases with increasing background contributions until it reaches a minimum value at a background probability of 0.1, corresponding to a signal-to-noise ratio of 0.1. Below this value, the Γ-norm increases again because of an increasing number of randomly colocalizing (false-positive) pixels. This result demonstrates that the Γ-norm analysis remains valid even for images that contain 10× higher pixel intensities for uncorrelated pixels compared to correlated pixels, thus exhibiting remarkable robustness against noise. In contrast, the PCC for the same data continues dropping steadily and returns negative values for a background probability of less than 0.1 (figure 4.30 d). Without comparison to the Γ-norm it would thus be impossible to draw any conclusion whether these images still colocalize or not.

In Figure 4.30 a, the Γ_3-norm is plotted as a function of the probability of colocalization on all three channels (P_c). The resulting proportional relationship proves the Γ-norm a valid parameter to quantify colocalization. Analyzed data should be divided into 10-100 subsections, to receive reasonable Γ-norm values. A Γ-norm computed with less than 10 sections is arguable due to a high statistical error. Whereas an undue computing time is necessary at 100 or more sections (figure 4.30 b). The impact of un-correlated background noise on the Γ-norm, is shown in figure 4.30 c. Here, the relative fraction of detected colocalization is plotted versus the probability of each channel to detect a noise pixel. Thus, with rising P_{bg}, the fraction of false-positive detected colocalization increases, while there is no real colocalization. Put into perspective, a noticeable false-positive detection only occurs at unreasonably high noise levels, i.e. 20% background noise.

The validity of the aforementioned anti-fraction (AF) can also be demonstrated by simulations, as can be seen in table 4.3. Comparing the AF values, which are directly calculated out of the received Γ-norm

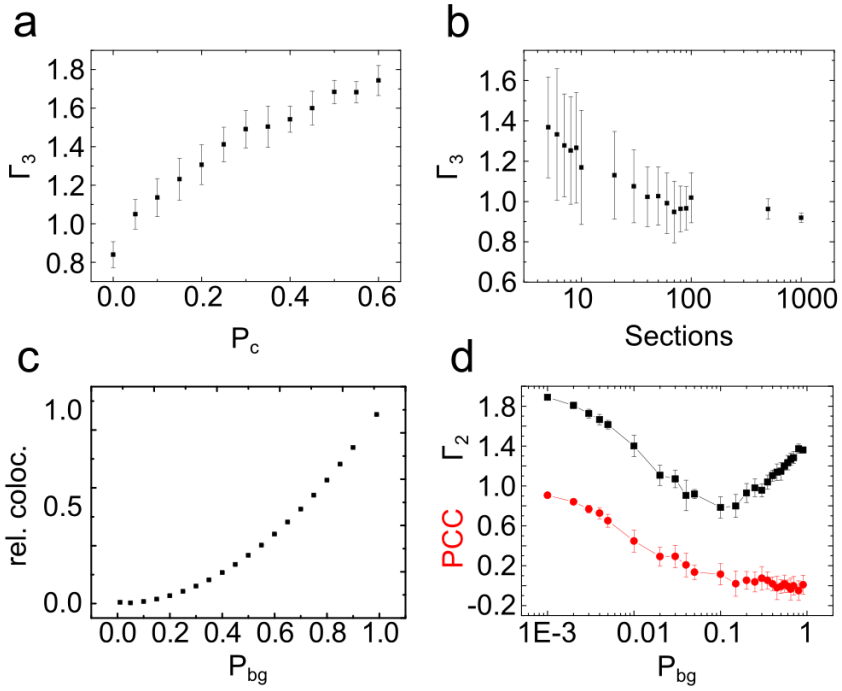

Figure 4.30: Computer simulations of 10^5 pixels of 30 experiments.
A total of 30 test images, each consisting of 3 color channels with 300×300 pixels, respectively, were created and analyzed. Here, each pixel value was randomly assigned with a probability P_c describing the probability of colocalization between the color channels. P_{bg} is the probability for un-correlated signal, and $P_{r,g,b}$ is the probability for a signal value in each corresponding color channel. (a) The Γ-norm as a function of P_c with a constant value of $P_{bg} = P_r = P_g = P_b = 0.4$. (b) The Γ-norm as a function of the number of sections. P_c is set to 0.05 and P_{bg} is set to 0.35. (c) The probability to detect random colocalization as a function of un-correlated background where $P_{bg} = P_r = P_g = P_b$. (d) A direct comparison of the Γ-norm for two colors with the PCC. For the Γ-norm a clear minimum of approximately 1 is visible with increasing background noise P_{bg}, whereas the PCC decreases monotonously and even becomes negative for large values of P_{bg}. The minimum value for Γ_2 indicates the lowest value of P_{bg} for which the colocalization analysis is still meaningful. For the PCC such value is not defined and if it weren't for the direct comparison with the Γ-norm analysis, then it would be impossible to determine the minimum P_{bg} after which the analysis fails.

Table 4.3: Γ-norm analysis results for simulated pixel-traces of samples with realistic fractions of colocalized signals. 10^5 pixels were simulated and the norms represent stable average values of 30 simulations. P_c denotes the probability to detect a colocalized event which ranges from 1 down to 0.6 with corresponding Γ-norms and anti-fractions AF. The background probability P_{bg} is calculated as the complement of P_c. Note how well the AF retrieved from the images corresponds to calculated P_{bg}.

P_C	$P_{bg}\ (1 - P_C)$	Γ_3	AF
1.00	0.00	2.646	0.000
0.99	0.01	2.628	0.008
0.90	0.10	2.435	0.081
0.80	0.20	2.166	0.183
0.70	0.30	2.026	0.235
0.60	0.40	1.775	0.330

values, to the not colocalizing fraction $1 - P_c$, the good consistence oft the two parameters becomes evident.

Taken together, the novel Γ-norm method is able to quantitatively evaluate colocalization in microscopy data. Furthermore, the extension of this method to the analysis of three- or multicolor images is straightforward, while PCC and PCC-like schemes are only able to crosswise check two channels for colocalization. Additionally the superior robustness of this method against the influence of varying background or random noise was showcased.

5 Summary and Outlook

The main findings provided by this work can be subdivided in two categories: First, new approaches to well established imaging techniques, with a wide field of applications, mostly within molecular cell biology, are introduced and evaluated with the help of examples from the field of fluorescence microscopy. Second, by applying these technical advances, a variety of molecular interactions of the RNA-binding protein *At*GRP7 are revealed, in live cell– as well as *in vitro* studies. In the course of the last years, the knowledge about *At*GRP7 was highly increased by this work within the framework of the collaborative research centre SFB 613, which successfully came to an end with the beginning of this year.

Advanced imaging techniques using the photoswitchable reporter Dronpa-s

Dronpa-s is shown to provide a versatile tool to fluorescence imaging as a reporter in plants, as well as in mammalian cells. In particular its ability to be switched between an on– and an off-state increases its overall aptitude. Here, Dronpa-s is presented as an enhanced alternative to standard fluorescent proteins like eGFP, pa-GFP and others, commonly used in fluorescence imaging. As an example, transport kinetics are often determined by applying imaging techniques like FRAP and FLIP, which in essence involve photobleaching of a sub-fraction of fluorescent proteins within the sample. This is achieved by exposing parts of the sample to intense laser radiation. Such treatment is phototoxic to an extent for most cell types. Thus the results of experiments inducing intense photobleaching are often argued to just reflect a disturbed

system and not being representative for physiologically healthy cell. As a result it was found, that Dronpa-s is efficiently switched-off at comparably low laser intensities. Thus, the benefit of using Dronpa-s and thereby avoiding phototoxic bleaching processes is described in chapter 4.1.

However, photobleaching and (in case of pa-GFP) photoactivation also afford conventionally irreversible processes. Obviously the reversibility of Dronpa-s's switching is a core advantage, rendering the fluorophore a multi-purpose tool. Chapter 4.3 describes the usage of Dronpa-s for repeated FRAP and photoactivation studies carried out in the same cell. This showcases the extendability of Dronpa-s to all imaging techniques demanding photoactivation or bleaching, in any possible way.

Additionally photoswitching of Dronpa-s, specifically within the nucleus, is demonstrated in chapter 4.3.2. This provides an extension to FRAP or photoactivation experiments, enabling a determination of transport into and out of cell compartments. The extended method is referred to as *Selective Photoswitching*.

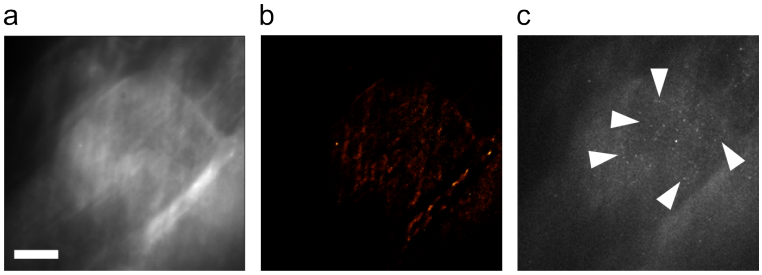

Figure 5.1: SOFI analysis of *At*GRP7 in a plant cell. *Arabidopsis* root cells expressing *At*GRP7-Dronpa-s were imaged with standard widefield microscopy. A movie of fluorescence images was collected by an EMCCD camera (Andor). (a) Epifluorescence image. Scale bar = 30 µm. (b) dSTORM reconstruction out of 10000 frames. (c) SOFI reconstruction out of 100 frames. Arrow heads denote reconstructed details. Dark areas surrounded by bright *At*GRP7-Dronpa-s aggregates become visible.

Although, Dronpa has been used for super-resolution imaging techniques in the past (i.e. by Andresen et al. [2008]), it is not a straightforward solution. More over, there are better alternatives amongst the fluorescent proteins for super-resolution purposes. I.e. mEOS2 has been reported to perform well in super-resolution imaging by Endesfelder et al. [2011]. However, a new approach recently emerging, termed *Super-resolution optical fluctuation imaging* (SOFI) , showcases a convenient method involving Dronpa as a blinking emitter to compute super-resolved images [Dedecker et al., 2012, Dertinger et al., 2010, 2012]. A first promising implementation of this method applied to *Arabidopsis* root cells expressing *At*GRP7-Dronpa-s is displayed in figure 5.1. Progress on this extends the versatility of Dronpa-s in terms of an all-purpose fluorescent protein for live cell imaging.

A novel approach to colocalization studies

One of the major achievements of this work is the novel approach to colocalization studies, which is based on the *Correlation matrix method* introduced by Yahiatène et al. [2012].

A new method to quantitatively evaluate colocalization in microscopy data is introduced in chapter 4.6. This method, termed Γ-norm analysis, yields several key benefits: For the very first time a method is capable to provide a single parameter, determining colocalization of three or even more channels. Commonly used methods like PCC, are only able to crosswise check two channels for colocalization at a time. The novel Γ-norm analysis exhibits superior robustness against high background or random noise levels. It is also demonstrated that the Γ-norm is only slightly affected by strong intensity fluctuations across different channels. Furthermore, a topology map of Γ-norm values is capable to reconstruct even noisy images. Applied to live-cell images, the Γ-norm method allows to extract structural information as well as a reliable anti-fraction by applying a linear selection, which is a novelty for its own.

For future work, the Γ-norm analysis can readily be applied to 3D and super-resolution microscopy data, as well as data obtained by other contrast methods, e.g. Raman scattering or second harmonic generation (SHG). Another goal would be to expand the method to visualize dynamic colocalization effects in live cell movies.

To enable an easy adoption to the Γ-norm analysis, a plugin for the widely used open-source image analysis software Fiji was assembled.

*At*GRP7 is actively imported in the nucleus

In chapter 4.2 the localization of *At*GRP7 throughout an *Arabidopsis* cell is mapped with the help of Dronpa-s as a fluorescent reporter. A high abundance of *At*GRP7 within the nucleus was determined. Further it was found that the protein localizes to the cytoplasm but is not existent at the cell wall.

Selective photoswitching analysis in chapter 4.3 show that *At*GRP7 overcomes the nuclear barrier by shuttling through the nuclear pore complexes due to active transport against the concentration gradient. It was found that the import speed is not constant, but varies during the course of a day, according to the changing *At*GRP7 concentration, which obeys a circadian rhythmicity.

Furthermore, the nuclear export of *At*GRP7 was revealed for the first time during a selective photoswitching experiment.

FCS studies reveal binding mechanisms of protein RNA interactions

The binding of *At*GRP7 to its own mRNA *AtGRP7* is considered a key element to the protein's physiological function. Upon binding, *At*GRP7 induces an alternative splicing of the transcript, and therefore,

triggers a self regulatory oscillation in form of a negative feedback-loop. Closer *in vitro* analysis of a putative binding site at the intron of the transcript, exhibits a rather weak but specific binding. A K_D value in the range of 400 nM (chapter 4.4.1) denotes a weak affinity of protein and transcript, but may explain the high abundance of *At*GRP7 within the nucleus, as the premature transcript locates exclusively to the nucleoplasm. The high protein concentration might compensate for the weak binding.

By determining the characteristic diffusion times of purified *At*GRP7, bound to several fragments of the putative binding site, a core binding sequence could be narrowed down via FCS analysis of single molecule time traces.

In chapter 4.4.2 the sequence specificity of the binding is determined by a mutational analysis. Here, point mutations were inserted into the core binding sequence. Furthermore, the affinity of *At*GRP7 to the mutated sequences was determined. Two particular point mutations yielded a dramatic loss in binding affinity. This showcases the sequence specificity of *At*GRP7 binding to its transcript.

Chapter 4.4.3 describes how the core binding sequence was converted to a secondary structure hairpin loop by insertion of two point mutations. FCS studies reveal that the transcript, upon binding *At*GRP7, is unfolded into a stretched form. This may be of importance for the introduction of the aforementioned alternative splicing.

*At*GRP7 contributes in processing bodies

In chapter 4.5 the novel Γ-norm analysis provides information about protein-protein interactions between *At*GRP7 and DCP1, which is a marker for processing bodies. Upon introduction of oxidative stress to *Nicotiana benthamiana* leaf cells, both proteins form aggregates within the cytoplasm. Γ-norm analysis reveals aggregations of both proteins to colocalize significantly. This suggests *At*GRP7 to contribute to processing bodies, as known from other RNPs. Its ability to bind RNA

might enable the aggregation, since processing bodies are sites of high mRNA abundance.

Bibliography

Jeremy Adler and Ingela Parmryd. Quantifying colocalization by correlation: the pearson correlation coefficient is superior to the mander's overlap coefficient. *Cytometry A*, 77(8):733–742, Aug 2010. doi: 10.1002/cyto.a.20896. URL `http://dx.doi.org/10.1002/cyto.a.20896`. 84

David Alabadí, Marcelo J. Yanovsky, Paloma Más, Stacey L. Harmer, and Steve A. Kay. Critical role for cca1 and lhy in maintaining circadian rhythmicity in arabidopsis. *Curr Biol*, 12(9):757–761, Apr 2002. 31

Gul Shad Ali and Annireddy S N Reddy. Atp, phosphorylation and transcription regulate the mobility of plant splicing factors. *J Cell Sci*, 119(Pt 17):3527–3538, Sep 2006. doi: 10.1242/jcs.03144. URL `http://dx.doi.org/10.1242/jcs.03144`. 64

R. Ando, H. Mizuno, and A. Miyawaki. Regulated fast nucleocytoplasmic shuttling observed by reversible protein highlighting. *Science*, 306(5700):1370–1373, Nov 2004. doi: 10.1126/science.1102506. URL `http://dx.doi.org/10.1126/science.1102506`. 2, 4, 14, 53, 54, 55, 56

Martin Andresen, Andre C Stiel, Simon Trowitzsch, Gert Weber, Christian Eggeling, Markus C Wahl, Stefan W Hell, and Stefan Jakobs. Structural basis for reversible photoswitching in dronpa. *Proc Natl Acad Sci U S A*, 104(32):13005–13009, Aug 2007. doi: 10.1073/pnas.0700629104. URL `http://dx.doi.org/10.1073/pnas.0700629104`. 14

Martin Andresen, Andre C Stiel, Jonas Fölling, Dirk Wenzel, Andreas Schönle, Alexander Egner, Christian Eggeling, Stefan W Hell, and

Stefan Jakobs. Photoswitchable fluorescent proteins enable monochromatic multilabel imaging and dual color fluorescence nanoscopy. *Nat Biotechnol*, 26(9):1035–1040, Sep 2008. doi: 10.1038/nbt.1493. URL `http://dx.doi.org/10.1038/nbt.1493`. 105

D. Axelrod, D. E. Koppel, J. Schlessinger, E. Elson, and W. W. Webb. Mobility measurement by analysis of fluorescence photobleaching recovery kinetics. *Biophys J*, 16(9):1055–1069, Sep 1976. 1, 63, 64

N. Bechtold and G. Pelletier. In planta agrobacterium-mediated transformation of adult arabidopsis thaliana plants by vacuum infiltration. *Methods Mol Biol*, 82:259–266, 1998. 50

H. P. Bogerd, R. E. Benson, R. Truant, A. Herold, M. Phingbodhipakkiya, and B. R. Cullen. Definition of a consensus transportin-specific nucleocytoplasmic transport signal. *J Biol Chem*, 274(14): 9771–9777, Apr 1999. 3, 63, 75

Kevin Braeckmans, Liesbeth Peeters, Niek N Sanders, Stefaan C De Smedt, and Joseph Demeester. Three-dimensional fluorescence recovery after photobleaching with the confocal scanning laser microscope. *Biophys J*, 85(4):2240–2252, Oct 2003. doi: 10.1016/S0006-3495(03)74649-9. URL `http://dx.doi.org/10.1016/S0006-3495(03)74649-9`. 64

Kevin Braeckmans, Katrien Remaut, Roosmarijn E Vandenbroucke, Bart Lucas, Stefaan C De Smedt, and Joseph Demeester. Line frap with the confocal laser scanning microscope for diffusion measurements in small regions of 3-d samples. *Biophys J*, 92(6): 2172–2183, Mar 2007. doi: 10.1529/biophysj.106.099838. URL `http://dx.doi.org/10.1529/biophysj.106.099838`. 64

José Braga, Joana M P Desterro, and Maria Carmo-Fonseca. Intracellular macromolecular mobility measured by fluorescence recovery after photobleaching with confocal laser scanning microscopes. *Mol Biol Cell*, 15(10):4749–4760, Oct 2004. doi: 10.1091/mbc.E04-06-0496. URL `http://dx.doi.org/10.1091/mbc.E04-06-0496`. 64

J Ross Buchan and Roy Parker. Eukaryotic stress granules: the ins and outs of translation. *Mol Cell*, 36(6):932–941, Dec 2009. doi:

10.1016/j.molcel.2009.11.020. URL http://dx.doi.org/10.1016/j.molcel.2009.11.020. 84

J Ross Buchan, Denise Muhlrad, and Roy Parker. P bodies promote stress granule assembly in saccharomyces cerevisiae. *J Cell Biol*, 183(3):441–455, Nov 2008. doi: 10.1083/jcb.200807043. URL http://dx.doi.org/10.1083/jcb.200807043. 84

J. C. Bulinski, D. J. Odde, B. J. Howell, T. D. Salmon, and C. M. Waterman-Storer. Rapid dynamics of the microtubule binding of ensconsin in vivo. *J Cell Sci*, 114(Pt 21):3885–3897, Nov 2001. 64

Gustavo Carrero, Darin McDonald, Ellen Crawford, Gerda de Vries, and Michael J Hendzel. Using frap and mathematical modeling to determine the in vivo kinetics of nuclear proteins. *Methods*, 29(1): 14–28, Jan 2003. 64

M. Chalfie, Y. Tu, G. Euskirchen, W. W. Ward, and D. C. Prasher. Green fluorescent protein as a marker for gene expression. *Science*, 263(5148):802–805, Feb 1994. 1, 13

Peter Dedecker, Gary C H. Mo, Thomas Dertinger, and Jin Zhang. Widely accessible method for superresolution fluorescence imaging of living systems. *Proc Natl Acad Sci U S A*, 109(27):10909–10914, Jul 2012. doi: 10.1073/pnas.1204917109. URL http://dx.doi.org/10.1073/pnas.1204917109. 105

W. L. DeLano. The pymol user's manual. DeLano Scientific, Palo Alto, CA, USA, 2002. 14, 27

Thomas Dertinger, Mike Heilemann, Robert Vogel, Markus Sauer, and Shimon Weiss. Superresolution optical fluctuation imaging with organic dyes. *Angew Chem Int Ed Engl*, 49(49):9441–9443, Dec 2010. doi: 10.1002/anie.201004138. URL http://dx.doi.org/10.1002/anie.201004138. 105

Thomas Dertinger, Ryan Colyer, Robert Vogel, Mike Heilemann, Markus Sauer, Jörg Enderlein, and Shimon Weiss. Superresolution optical fluctuation imaging (sofi). *Adv Exp Med Biol*, 733: 17–21, 2012. doi: 10.1007/978-94-007-2555-3_2. URL http://dx.doi.org/10.1007/978-94-007-2555-3_2. 105

Sören Doose, Hannes Neuweiler, and Markus Sauer. Fluorescence quenching by photoinduced electron transfer: a reporter for conformational dynamics of macromolecules. *Chemphyschem*, 10(9-10): 1389–1398, 2009. 81

J. Ellenberg, E. D. Siggia, J. E. Moreira, C. L. Smith, J. F. Presley, H. J. Worman, and J. Lippincott-Schwartz. Nuclear membrane dynamics and reassembly in living cells: targeting of an inner nuclear membrane protein in interphase and mitosis. *J Cell Biol*, 138(6): 1193–1206, Sep 1997. 64

Ulrike Endesfelder, Sebastian Malkusch, Benjamin Flottmann, Justine Mondry, Piotr Liguzinski, Peter J. Verveer, and Mike Heilemann. Chemically induced photoswitching of fluorescent probes–a general concept for super-resolution microscopy. *Molecules*, 16(4):3106–3118, 2011. doi: 10.3390/molecules16043106. URL `http://dx.doi.org/10.3390/molecules16043106`. 105

Eva M. Farré, Stacey L. Harmer, Frank G. Harmon, Marcelo J. Yanovsky, and Steve A. Kay. Overlapping and distinct roles of prr7 and prr9 in the arabidopsis circadian clock. *Curr Biol*, 15 (1):47–54, Jan 2005. doi: 10.1016/j.cub.2004.12.067. URL `http://dx.doi.org/10.1016/j.cub.2004.12.067`. 31

Natália Freitas and Celso Cunha. Mechanisms and signals for the nuclear import of proteins. *Curr Genomics*, 10(8):550–557, Dec 2009. doi: 10.2174/138920209789503941. URL `http://dx.doi.org/10.2174/138920209789503941`. 63

Sumire Fujiwara, Atsushi Oda, Riichiro Yoshida, Kanae Niinuma, Kana Miyata, Yusuke Tomozoe, Takeomi Tajima, Mayu Nakagawa, Kounosuke Hayashi, George Coupland, and Tsuyoshi Mizoguchi. Circadian clock proteins lhy and cca1 regulate svp protein accumulation to control flowering in arabidopsis. *Plant Cell*, 20(11):2960–2971, Nov 2008. doi: 10.1105/tpc.108.061531. URL `http://dx.doi.org/10.1105/tpc.108.061531`. 31

Yu I Glazachev and V. V. Khramtsov. Fluorescence recovery under decaying photobleaching irradiation: concept and experiment. *J*

Fluoresc, 16(6):773–781, Nov 2006. doi: 10.1007/s10895-006-0130-8. URL http://dx.doi.org/10.1007/s10895-006-0130-8. 64

J. Shawn Goodwin and Anne K Kenworthy. Photobleaching approaches to investigate diffusional mobility and trafficking of ras in living cells. *Methods*, 37(2):154–164, Oct 2005. doi: 10.1016/j.ymeth.2005.05.013. URL http://dx.doi.org/10.1016/j.ymeth.2005.05.013. 64

D. Görlich and U. Kutay. Transport between the cell nucleus and the cytoplasm. *Annu Rev Cell Dev Biol*, 15:607–660, 1999. doi: 10.1146/annurev.cellbio.15.1.607. URL http://dx.doi.org/10.1146/annurev.cellbio.15.1.607. 63

Guy M Hagen, Wouter Caarls, Keith A Lidke, Anthony H B De Vries, Cornelia Fritsch, B. George Barisas, Donna J Arndt-Jovin, and Thomas M Jovin. Fluorescence recovery after photobleaching and photoconversion in multiple arbitrary regions of interest using a programmable array microscope. *Microsc Res Tech*, 72(6):431–440, Jun 2009. doi: 10.1002/jemt.20686. URL http://dx.doi.org/10.1002/jemt.20686. 64

Mark A Hallen and Anita T Layton. Expanding the scope of quantitative frap analysis. *J Theor Biol*, 262(2):295–305, Jan 2010. doi: 10.1016/j.jtbi.2009.10.020. URL http://dx.doi.org/10.1016/j.jtbi.2009.10.020. 64

S. L. Harmer, S. Panda, and S. A. Kay. Molecular bases of circadian rhythms. *Annu Rev Cell Dev Biol*, 17:215–253, 2001. doi: 10.1146/annurev.cellbio.17.1.215. URL http://dx.doi.org/10.1146/annurev.cellbio.17.1.215. 31, 33

R. Heim, A. B. Cubitt, and R. Y. Tsien. Improved green fluorescence. *Nature*, 373(6516):663–664, Feb 1995. doi: 10.1038/373663b0. URL http://dx.doi.org/10.1038/373663b0. 13

C. Heintzen, M. Nater, K. Apel, and D. Staiger. Atgrp7, a nuclear rna-binding protein as a component of a circadian-regulated negative feedback loop in arabidopsis thaliana. *Proc Natl Acad Sci U S A*, 94 (16):8515–8520, Aug 1997. 33, 54

Frank Herrmann, Jaeho Lee, Mark T Bedford, and Frank O Fackelmayer. Dynamics of human protein arginine methyltransferase 1(prmt1) in vivo. *J Biol Chem*, 280(45):38005–38010, Nov 2005. doi: 10.1074/jbc.M502458200. URL `http://dx.doi.org/10.1074/jbc.M502458200`. 64

H. Kautsky. Quenching of luminescence by oxygen. *Transactions of the Faraday Society*, 35:216–219, 1939. 15

Nancy Kedersha, Georg Stoecklin, Maranatha Ayodele, Patrick Yacono, Jens Lykke-Andersen, Marvin J. Fritzler, Donalyn Scheuner, Randal J. Kaufman, David E. Golan, and Paul Anderson. Stress granules and processing bodies are dynamically linked sites of mrnp remodeling. *J Cell Biol*, 169(6):871–884, Jun 2005. doi: 10.1083/jcb.200502088. URL `http://dx.doi.org/10.1083/jcb.200502088`. 84

Yeon-Ok Kim, SangO. Pan, Che-Hun Jung, and Hunseung Kang. A zinc finger-containing glycine-rich rna-binding protein, atrz-1a, has a negative impact on seed germination and seedling growth of arabidopsis thaliana under salt or drought stress conditions. *Plant Cell Physiol*, 48(8):1170–1181, Aug 2007. doi: 10.1093/pcp/pcm087. URL `http://dx.doi.org/10.1093/pcp/pcm087`. 31

M. J. Kruhlak, M. A. Lever, W. Fischle, E. Verdin, D. P. Bazett-Jones, and M. J. Hendzel. Reduced mobility of the alternate splicing factor (asf) through the nucleoplasm and steady state speckle compartments. *J Cell Biol*, 150(1):41–51, Jul 2000. 64

Mario Köster, Thomas Frahm, and Hansjörg Hauser. Nucleocytoplasmic shuttling revealed by frap and flip technologies. *Curr Opin Biotechnol*, 16(1):28–34, Feb 2005. doi: 10.1016/j.copbio.2004.11.002. URL `http://dx.doi.org/10.1016/j.copbio.2004.11.002`. 64

J. Lippincott-Schwartz, E. Snapp, and A. Kenworthy. Studying protein dynamics in living cells. *Nat Rev Mol Cell Biol*, 2(6):444–456, Jun 2001. doi: 10.1038/35073068. URL `http://dx.doi.org/10.1038/35073068`. 1, 64

Jennifer Lippincott-Schwartz, Nihal Altan-Bonnet, and George H Patterson. Photobleaching and photoactivation: following protein dynamics in living cells. *Nat Cell Biol*, Suppl:S7–14, Sep 2003. 64

James C W. Locke, Megan M. Southern, László Kozma-Bognár, Victoria Hibberd, Paul E. Brown, Matthew S. Turner, and Andrew J. Millar. Extension of a genetic network model by iterative experimentation and mathematical analysis. *Mol Syst Biol*, 1:2005.0013, 2005. doi: 10.1038/msb4100018. URL `http://dx.doi.org/10.1038/msb4100018`. 31

Ariel Lubelski and Joseph Klafter. Fluorescence recovery after photobleaching: the case of anomalous diffusion. *Biophys J*, 94(12): 4646–4653, Jun 2008. doi: 10.1529/biophysj.107.119081. URL `http://dx.doi.org/10.1529/biophysj.107.119081`. 64

Martina Lummer, Fabian Humpert, Christian Steuwe, Katharina Caesar, Mark Schüttpelz, Markus Sauer, and Dorothee Staiger. Reversible photoswitchable dronpa-s monitors nucleocytoplasmic transport of an rna-binding protein in transgenic plants. *Traffic*, 12(6): 693–702, Jun 2011. doi: 10.1111/j.1600-0854.2011.01180.x. URL `http://dx.doi.org/10.1111/j.1600-0854.2011.01180.x`. 53, 67

D. Magde, E. L. Elson, and W. W. Webb. Fluorescence correlation spectroscopy. ii. an experimental realization. *Biopolymers*, 13(1): 29–61, Jan 1974. doi: 10.1002/bip.1974.360130103. URL `http://dx.doi.org/10.1002/bip.1974.360130103`. 17

E. M. Manders, J. Stap, G. J. Brakenhoff, R. van Driel, and J. A. Aten. Dynamics of three-dimensional replication patterns during the s-phase, analysed by double labelling of dna and confocal microscopy. *J Cell Sci*, 103 (Pt 3):857–862, Nov 1992. 84

E. M. M. Manders, F. J. Verbeek, and J. A. Aten. Measurement of co-localization of objects in dual-colour confocal images. *Journal of Microscopy*, 169(3):375–382, 1993. ISSN 1365-2818. doi: 10.1111/j.1365-2818.1993.tb03313.x. URL `http://dx.doi.org/10.1111/j.1365-2818.1993.tb03313.x`. 5

R.A. Marcus and Norman Sutin. Electron transfers in chemistry and biology. *Biochimica et Biophysica Acta (BBA) - Reviews on Bioenergetics*, 811(3):265 – 322, 1985. ISSN 0304-4173. doi: 10.1016/0304-4173(85)90014-X. URL `http://www.sciencedirect.com/science/article/pii/030441738590014X`. 16

Davide Mazza, Francesca Cella, Giuseppe Vicidomini, Silke Krol, and Alberto Diaspro. Role of three-dimensional bleach distribution in confocal and two-photon fluorescence recovery after photobleaching experiments. *Appl Opt*, 46(30):7401–7411, Oct 2007. 64

Davide Mazza, Kevin Braeckmans, Francesca Cella, Ilaria Testa, Dries Vercauteren, Jo Demeester, Stefaan S De Smedt, and Alberto Diaspro. A new frap/frapa method for three-dimensional diffusion measurements based on multiphoton excitation microscopy. *Biophys J*, 95(7):3457–3469, Oct 2008. doi: 10.1529/biophysj.108.133637. URL `http://dx.doi.org/10.1529/biophysj.108.133637`. 64

Dagmar Mohr, Steffen Frey, Torsten Fischer, Thomas Güttler, and Dirk Görlich. Characterisation of the passive permeability barrier of nuclear pore complexes. *EMBO J*, 28(17):2541–2553, Sep 2009. doi: 10.1038/emboj.2009.200. URL `http://dx.doi.org/10.1038/emboj.2009.200`. 63

Florian Mueller, Paul Wach, and James G McNally. Evidence for a common mode of transcription factor interaction with chromatin as revealed by improved quantitative fluorescence recovery after photobleaching. *Biophys J*, 94(8):3323–3339, Apr 2008. doi: 10.1529/biophysj.107.123182. URL `http://dx.doi.org/10.1529/biophysj.107.123182`. 64

Morten Nielsen, Claus Lundegaard, Ole Lund, and Thomas Nordahl Petersen. Cphmodels-3.0–remote homology modeling using structure-guided sequence profiles. *Nucleic Acids Res*, 38(Web Server issue): W576–W581, Jul 2010. doi: 10.1093/nar/gkq535. URL `http://dx.doi.org/10.1093/nar/gkq535`. 32

Alessia Para, Eva M. Farré, Takato Imaizumi, José L. Pruneda-Paz, Franklin G. Harmon, and Steve A. Kay. Prr3 is a vascular regulator of toc1 stability in the arabidopsis circadian clock. *Plant Cell*,

19(11):3462–3473, Nov 2007. doi: 10.1105/tpc.107.054775. URL http://dx.doi.org/10.1105/tpc.107.054775. 31

Marc Parisien and François Major. The mc-fold and mc-sym pipeline infers rna structure from sequence data. *Nature*, 452(7183):51–55, Mar 2008. doi: 10.1038/nature06684. URL http://dx.doi.org/10.1038/nature06684. 27

George H. Patterson and Jennifer Lippincott-Schwartz. A photoactivatable gfp for selective photolabeling of proteins and cells. *Science*, 297(5588):1873–1877, Sep 2002. doi: 10.1126/science.1074952. URL http://dx.doi.org/10.1126/science.1074952. 2

N. Peyret. Prediction of nucleic acid hybridization: parameters and algorithms, 2000. 48

D. C. Prasher, V. K. Eckenrode, W. W. Ward, F. G. Prendergast, and M. J. Cormier. Primary structure of the aequorea victoria green-fluorescent protein. *Gene*, 111(2):229–233, Feb 1992. 13

E. A. Reits and J. J. Neefjes. From fixed to frap: measuring protein mobility and activity in living cells. *Nat Cell Biol*, 3(6):E145–E147, Jun 2001. doi: 10.1038/35078615. URL http://dx.doi.org/10.1038/35078615. 64

J. SantaLucia. A unified view of polymer, dumbbell, and oligonucleotide dna nearest-neighbor thermodynamics. *Proceedings of the National Academy of Sciences of the United States of America*, 95(4):1460–1465, 1998. 48

Fabian Schmidt, Aline Marnef, Man-Kim Cheung, Ian Wilson, John Hancock, Dorothee Staiger, and Michael Ladomery. A proteomic analysis of oligo(dt)-bound mrnp containing oxidative stress-induced arabidopsis thaliana rna-binding proteins atgrp7 and atgrp8. *Mol Biol Rep*, 37(2):839–845, Feb 2010. doi: 10.1007/s11033-009-9636-x. URL http://dx.doi.org/10.1007/s11033-009-9636-x. 32

Jan C Schöning and Dorothee Staiger. At the pulse of time: protein interactions determine the pace of circadian clocks. *FEBS Lett*, 579 (15):3246–3252, Jun 2005. doi: 10.1016/j.febslet.2005.03.028. URL http://dx.doi.org/10.1016/j.febslet.2005.03.028. 54

Jan C Schöning and Dorothee Staiger. Rna-protein interaction mediating post-transcriptional regulation in the circadian system. *Methods Mol Biol*, 479:337–351, 2009. doi: 10.1007/978-1-59745-289-2_21. URL `http://dx.doi.org/10.1007/978-1-59745-289-2_21`. 54

Jan C Schöning, Corinna Streitner, Damian R Page, Sven Hennig, Kenko Uchida, Eva Wolf, Masaki Furuya, and Dorothee Staiger. Auto-regulation of the circadian slave oscillator component atgrp7 and regulation of its targets is impaired by a single rna recognition motif point mutation. *Plant J*, 52(6):1119–1130, Dec 2007. doi: 10.1111/j.1365-313X.2007.03302.x. URL `http://dx.doi.org/10.1111/j.1365-313X.2007.03302.x`. 34, 54, 76

Jan C Schöning, Corinna Streitner, Irmtraud M Meyer, Yahong Gao, and Dorothee Staiger. Reciprocal regulation of glycine-rich rna-binding proteins via an interlocked feedback loop coupling alternative splicing to nonsense-mediated decay in arabidopsis. *Nucleic Acids Res*, 36(22):6977–6987, Dec 2008. doi: 10.1093/nar/gkn847. URL `http://dx.doi.org/10.1093/nar/gkn847`. 33, 49, 54

Mark Schüttpelz, Jan C Schöning, Sören Doose, Hannes Neuweiler, Elisabeth Peters, Dorothee Staiger, and Markus Sauer. Changes in conformational dynamics of mrna upon atgrp7 binding studied by fluorescence correlation spectroscopy. *J Am Chem Soc*, 130 (29):9507–9513, Jul 2008. doi: 10.1021/ja801994z. URL `http://dx.doi.org/10.1021/ja801994z`. 34, 54, 76, 77, 83

O. Shimomura, F. H. Johnson, and Y. Saiga. Extraction, purification and properties of aequorin, a bioluminescent protein from the luminous hydromedusan, aequorea. *J Cell Comp Physiol*, 59:223–239, Jun 1962. 1, 13

H. Siomi and G. Dreyfuss. A nuclear localization domain in the hnrnp a1 protein. *J Cell Biol*, 129(3):551–560, May 1995. 63

Brian L Sprague and James G McNally. Frap analysis of binding: proper and fitting. *Trends Cell Biol*, 15(2):84–91, Feb 2005. doi: 10.1016/j.tcb.2004.12.001. URL `http://dx.doi.org/10.1016/j.tcb.2004.12.001`. 64

D. Staiger. Rna-binding proteins and circadian rhythms in arabidopsis thaliana. *Philos Trans R Soc Lond B Biol Sci*, 356(1415):1755–1759, Nov 2001. doi: 10.1098/rstb.2001.0964. URL `http://dx.doi.org/10.1098/rstb.2001.0964`. 54

D. Staiger. Circadian rhythms in arabidopsis: time for nuclear proteins. *Planta*, 214(3):334–344, Jan 2002. 54

D. Staiger and K. Apel. Circadian clock-regulated expression of an rna-binding protein in arabidopsis: characterisation of a minimal promoter element. *Mol Gen Genet*, 261(4-5):811–819, Jun 1999. 33, 49, 54

D. Staiger and C. Heintzen. The circadian system of arabidopsis thaliana: forward and reverse genetic approaches. *Chronobiol Int*, 16(1):1–16, Jan 1999. 54

D. Staiger, K. Apel, and G. Trepp. The atger3 promoter confers circadian clock-regulated transcription with peak expression at the beginning of the night. *Plant Mol Biol*, 40(5):873–882, Jul 1999. 54

D. Staiger, L. Zecca, D. A. Wieczorek Kirk, K. Apel, and L. Eckstein. The circadian clock regulated rna-binding protein atgrp7 autoregulates its expression by influencing alternative splicing of its own pre-mrna. *Plant J*, 33(2):361–371, Jan 2003. 33, 34, 54, 76

Corinna Streitner, Selahattin Danisman, Franziska Wehrle, Jan C Schöning, James R Alfano, and Dorothee Staiger. The small glycine-rich rna binding protein atgrp7 promotes floral transition in arabidopsis thaliana. *Plant J*, 56:239–250, Aug 2008. doi: 10.1111/j.1365-313X.2008.03591.x. URL `http://dx.doi.org/10.1111/j.1365-313X.2008.03591.x`. 53, 54

R. Töpfer, V. Matzeit, B. Gronenborn, J. Schell, and H. H. Steinbiss. A set of plant expression vectors for transcriptional and translational fusions. *Nucleic Acids Res*, 15(14):5890, Jul 1987. 50

R. Y. Tsien. The green fluorescent protein. *Annu Rev Biochem*, 67:509–544, 1998. doi: 10.1146/annurev.biochem.67.1.509. URL `http://dx.doi.org/10.1146/annurev.biochem.67.1.509`. 1

J. D. Watson and F. H. Crick. Molecular structure of nucleic acids; a structure for deoxyribose nucleic acid. *Nature*, 171(4356):737–738, Apr 1953. 26

Idir Yahiatène, Sören Doose, Thomas Huser, and Markus Sauer. Correlation-matrix analysis of two-color coincidence events in single-molecule fluorescence experiments. *Anal Chem*, 84(6):2729–2736, Mar 2012. doi: 10.1021/ac2030283. URL `http://dx.doi.org/10.1021/ac2030283`. 46, 85, 87, 105

Alicja Ziemienowicz, Dorothea Haasen, Dorothee Staiger, and Thomas Merkle. Arabidopsis transportin1 is the nuclear import receptor for the circadian clock-regulated rna-binding protein atgrp7. *Plant Mol Biol*, 53(1-2):201–212, Sep 2003. doi: 10.1023/B:PLAN.0000009288.46713.1f. URL `http://dx.doi.org/10.1023/B:PLAN.0000009288.46713.1f`. 34

M. Zuker. Mfold web server for nucleic acid folding and hybridization prediction. *Nucleic Acids Research*, 31(13):3406–3415, 2003. ISSN 0305-1048. 48

Publications

This thesis is based on the following publications:

Lummer, M.; **Humpert, F.**; Steuwe, C.; Caesar, K.; Schüttpelz, M.; Sauer, M. ,& Staiger, D.; *Reversible photoswitchable DRONPA-s monitors nucleocytoplasmic transport of an RNA-binding protein in transgenic plants.*, Traffic, 2011, 12, 693-702

Wolf, A., Akrap, N., Marg, B., Galliardt, H., Heiligentag, M., , **Humpert, F.**, Sauer, M., Kaltschmidt, B., Kaltschmidt, C., Seidel, T.; *Elements of transcriptional machinery are compatible among plants and mammals.*, PLOS One, 2012, accepted manuscript

Martina Lummer, **Fabian Humpert**, Matthias Wiedenlübbert, Markus Sauer, Mark Schüttpelz, Dorothee Staiger;
A new set of reversibly photoswitchable fluorescent proteins for use in transgenic plants, Molecular Plant, 2012, manuscript provisionally accepted

Fabian Humpert , Idir Yahiatene , Martina Lummer , Markus Sauer, Thomas Huser; *Quantifying molecular colocalization in live cell fluorescence microscopy*, Nature Methods, 2013, manuscript under consideration

Conference contributions

Oral Contributions

XXIV. International Conference on Photochemistry, 2009, Toledo, Spain
Reading the Circadian Clock by means of Photoswitchable Proteins

SFB 613 Workshop, 2009, Bad Salzdetfurth, Germany
Tracking Protein Dynamics with Live Cell Imaging Techniques

SFB 613 Workshop, 2011, Loccum, Germany
Nucleocytoplasmic Transport of the RNA-binding Protein AtGRP7

Poster Presentations

15$^{\text{th}}$ International Workshop on 'Single Molecule Spectroscopy and Ultrasensitive Analysis in Life Sciences', PicoQuant, 2009, Berlin, Germany
Reading the Circadian Clock with Photoswitchable Proteins

SFB 613 International Workshop, 2010, Bielefeld, Germany
Investigation of a circadian slave-oscillator on the molecular level by single molecule spectroscopy and –imaging

UC Davis —Center for Biophotonics Science & Technology— Annual Retreat, 2012, Olympic Valley, California
Nucleocytoplasmic transport of the RNA-binding protein AtGRP7

Abbreviations

K_D 74
Dissociation constant.

Ar^+ 37
Argon Ionen.

CAI 47
codon adaptation index.

CLSM 21
Confocal Laser Scanning Microscopy.

ER 59, 60
Endoplasmic reticulum.

FWHM 53
Full width half maximum.

GFP 13
Green Fluorescent Protein.

HeNe 37
Helium Neon.

IDE 45
integrated development environment.

LSM 37
Laser Scanning Microscope.

MOC 5
Manders Overlap Coefficient.

NLS 61
Nuclear Localization Signal.

NPC 61
Nuclear Pore Complex.

PBS 50
Phosphate-buffered saline.

PCC 5
Pearson Correlation Coefficient.

PET 16
Photoninduced Electron Transfer.

PMT 37
Photomultiplier Tube.

PSF 20
point spread function.

ROI 45
region of interest.

SNR 19
signal to noise ratio.

SOFI 102
Super-Resolution Optical Fluctuation Imaging.

TIRF 21
Total Internal Reflection Fluorescence.

UTR 27
untranslated region.

zt 70
Zeitgeber time.

Acknowledgements

I am very grateful for all the support I received during the last years. Therefore I want to thank everyone who helped me in realizing this work.

First of all I want to thank Markus Sauer for giving me the opportunity to join his workgroup *Applied Laser Physics & Laser Spectroscopy* and to write my thesis here at Bielefeld University.

When Markus shifted his group to Würzburg, Thomas Huser jumped in and built up the new workgroup *Biomolecular Photonics*. Both, Markus and Thomas, gave me the chance to finish my thesis while staying in Bielefeld. I still appreciate this opportunity very much. I am very grateful to Thomas for offering me support during the last period of my work. It was a really fruitful time.

A special thanks goes to Gerd Wiebusch, who always helped me with technical questions regarding experimental setups. Thank you very much, no one can hold a candle to you in terms of technical expertise.

Also I would like to thank all of my present and former colleagues for all the fruitful discussions, motivations and cooperation. Especially Sigrun Henkenjohann, Sebastian van de Linde, Anindita Mukherjee, Andre Lampe, Marc Löllmann, Ralf Brune, Viola Mönkemöller and Wolfgang Hübner should be mentioned. Thank you for all the conversations on the matter.

For a splendid collaboration I'd like to thank Idir Yahiatene – Hopefully you will have an amazing time at the CBST. I am looking forward to tackling our next projects.

Furthermore I want to thank Tobias Klamp, Simon Hennig and Idir Yahiatene for always sharing the office and their good temper with me. I am grateful for every minute of the amazing office– and out-of-office time we spent together. Thanks a lot guys – we had a great time.

This Work partly emerged out of the collaborative research centre SFB 613, which was funded by the *German Research Foundation*. In the framework of the SFB 613, I closely collaborated with the members of Dorothee Staiger's *Molecular Cellphysiology* group. Therefore I'd like to express my gratitude to Dorothee Staiger, Martina Lummer and Kathrin Tegeler, for a pleasant and fruitful collaboration.

For proofreading of this manuscript I want to thank Sigrun Henkenjohann, Simon Hennig, Martina Lummer and Idir Yahiatene.

Thanks to Rudolf Böttner and Mark Schüttpelz, if it had not been for them, I wouldn't have found my way to D3.

Last but not least, I am very grateful to my whole family who always supported me by all means. Thank you, Sigrun, for all your endless support and understanding.

Erklärung

Hiermit versichere ich, dass ich die vorliegende Arbeit selbstständig und ohne unerlaubte Hilfsmittel verfasst habe.

Bielefeld, im Januar 2013

Fabian Humpert